Electrochemical Energy Reviews (2024) 7:12
https://doi.org/10.1007/s41918-024-00212-1

REVIEW ARTICLE

Li–Solid Electrolyte Interfaces/Interphases in All-Solid-State Li Batteries

Linan Jia[1] · Jinhui Zhu[2] · Xi Zhang[1] · Bangjun Guo[1] · Yibo Du[1] · Xiaodong Zhuang[2]

Received: 9 January 2023 / Revised: 21 April 2023 / Accepted: 9 January 2024
© The Author(s) 2024

Abstract

The emergence of all-solid-state Li batteries (ASSLBs) represents a promising avenue to address critical concerns like safety and energy density limitations inherent in current Li-ion batteries. Solid electrolytes (SEs) show significant potential in curtailing Li dendrite intrusion, acting as natural barriers against short circuits. However, the substantial challenges at the SEs−electrode interface, particularly concerning the anode, pose significant impediments to the practical implementation of ASSLBs. This review aims to delineate the most viable strategies for overcoming anode interfacial hurdles across four distinct categories of SEs: sulfide SEs, oxide SEs, polymer SEs, and halide SEs. Initially, pivotal issues such as anode interfacial side reactions, inadequate physical contact, and Li dendrite formation are comprehensively outlined. Furthermore, effective methodologies aimed at enhancing anode interfacial stability are expounded, encompassing approaches like solid electrolyte interface (SEI) interlayer insertion, SE optimization, and the adoption of Li alloy in lieu of Li metal, each tailored to specific SE categories. Moreover, this review presents novel insights into fostering interfaces between diverse SE types and Li anodes, while also advocating perspectives and recommendations for the future advancement of ASSLBs.

Keywords All-solid-state Li batteries · Solid electrolytes · Li metal anode · Li dendrites · Interface

1 Introduction

Since its inception in 1958, Li metal, renowned for its high energy density, has been a pivotal component in battery technology. The milestone moment arrived in 1976 when Whittingham introduced the first rechargeable Li-ion batteries (LIBs) featuring Li|Li_2S, boasting an exceptional specific energy nearing 500 Wh kg^{-1} [1]. These groundbreaking LIBs, comprising the $LiCoO_2$ cathode (crafted by Goodenough) and carbonaceous anode (engineered by Yoshino), emerged as the cornerstone of modern LIBs [2, 3]. Sony's development of the 18650-type LIB in 1991, which is post-acquisition of the aforementioned patent, marked a turning point, propelling the subsequent evolution and commercialization of LIBs through innovative electrode materials and electrolyte advancements [4]. The advent of LIBs heralded a new era, revolutionizing energy storage applications in automotive and portable electronics. However, inherent safety concerns, notably thermal runaway due to Li dendrites and the risk of short circuits, pose significant threats to LIB integrity. Furthermore, the limitation of current LIBs' energy density (capped at 300 Wh kg^{-1}) contributes to the prevalent "range anxiety" in electric vehicles, compounding the paramount concerns.

Addressing these challenges necessitates a paradigm shift—replacing conventional flammable liquid electrolytes (LEs) with robust and secure solid electrolytes (SEs) to realize all-solid-state Li batteries (ASSLBs). ASSLBs offer a definitive solution to mitigate safety issues. While the cathode materials in ASSLBs remain akin to those in LIBs, the former possess the potential for a 50% or greater increase in energy density through stacking, obviating the need for individual cell packing, metal shell fixation, and allocated space for coolants—A distinctive advantage in practical applications [5]. Consequently, owing to their exceptional

Co first author: Linan Jia and Jinhui Zhu

✉ Xi Zhang
braver1980@sjtu.edu.cn

1 School of Mechanical Engineering, Shanghai Jiao Tong University, Shanghai 200240, China

2 The Meso-Entropy Matter Lab, State Key Laboratory of Metal Matrix Composites, School of Chemistry and Chemical Engineering, Frontiers Science Center for Transformative Molecules, Shanghai Jiao Tong University, Shanghai 200240, China

Published online: 18 March 2024

safety profile and heightened energy density, ASSLBs stand as the frontrunner in the quest for a new generation of energy storage devices.

Typically, SEs need to satisfy several key criteria: (i) displaying appropriate ionic conductivity (> 0.1 mS cm^{-1}); (ii) possessing a broad electrochemical stability window (ESW); (iii) showcasing robust mechanical properties to hinder Li dendrite infiltration; (iv) maintaining cost-effectiveness; and (v) offering ease of processing [6]. To date, four primary categories of SEs have emerged: sulfide SEs, oxide SEs, polymer SEs, and halide SEs. These distinct categories of SEs, when integrated into ASSLBs, present diverse advantages and challenges owing to the distinctive electrochemical and physical characteristics they exhibit. This differentiation is summarized in Fig. 1, while Table 1 delineates the ionic conductivities of typical SEs.

The ionic conductivities of sulfide SEs rival those of traditional LEs and stand as one of the most promising directions in SE research. Notably, sulfide SEs showcase impressive mechanical properties, such as plastic deformation, and readily form densely packed interfaces [7]. A myriad of sulfide SE types have undergone exploration, including Li–P–S-based glasses, Li_6PS_5X (X = Cl, Br, or I), and $Li_{10}GeP_2S_{12}$ (LGPS) varieties. Glassy sulfide SEs possess advantageous plastic properties, circumventing high-resistance grain boundaries and facilitating efficient ionic flux due to their composition. An exemplary instance lies in the binary $xLi_2S\cdot(100-x)\ P_2S_5$ system, where x, ranging from 40 to 80 molar percentages, generates single-phase composition like $60Li_2S\cdot40P_2S_5$, $75Li_2S\cdot25P_2S_5$, among others [8]. The ionic conductivities of these glassy sulfide SEs typically fall within a moderate range of 10^{-2}–10^{-1} mS cm^{-1} at room temperature (RT). Strategies enhancing charge carrier concentration and mobility in glasses, involving compounds like Li_3PO_4, Li_4SiO_4, $LiBH_4$, and other Li salts, effectively bolster the ionic conductivity of glassy systems [9, 10]. Transitioning from glass to glassy ceramics via heat treatment influences their ionic conductivities, as observed in $Li_7P_3S_{11}$ derived from $70Li_2S\cdot30P_2S_5$ glass, exhibiting a high ionic conductivity of 1 mS cm^{-1} after heating within the range of 531–633 K. The substantial presence of interstitial sites and expansive open volumes between $P_2S_7^{4-}$ di-tetrahedra and PS_4^{3-} tetrahedra facilitates rapid Li^+ transport. Notably, Li_3PS_4 demonstrates three crystal types—α, β, and γ phases—with β-phase PS_4^{3-} tetrahedra presenting disorderly zig-zag structures and an ionic conductivity of approximately 3.2 mS cm^{-1} [11, 12]. Within the Li_6PS_5X argyrodite family, the anionic disorder plays a pivotal role in dictating differing ionic conductivities. Argyrodites like Li_6PS_5Cl (LPSC) and Li_6PS_5Br (LPSB) exhibit S^{2-}/X^- anion disorder due to partial exchange between normal X^- and S^{2-} sites, contributing to ionic conductivities of 1.9 and 0.68 mS cm^{-1} at RT, respectively. In contrast, Li_6PS_5I (LPSI) maintains an ordered anionic framework due to the larger non-interchangeable I^-, resulting in a lower ionic conductivity of 4.6×10^{-4} mS cm^{-1} [13, 14]. Substituting elements in argyrodites not only stabilizes the structure but also enhances the ionic conductivity of sulfide SEs, occurring at halide sites, PS_4^{3-} units, and free sulfur sites. Notably, $Li_{5.3}PS_{4.3}Cl_{1.7}$ stands as a representative, boasting an ionic conductivity of up to 17 mS cm^{-1} [15, 16]. The LGPS family, described as $Li1_{1-x}M_{2-x}P_{1+x}S_{12}$ ($0<x<2$) with M representing Si, Sn, or Ge, showcases remarkable potential. The groundbreaking LGPS superionic conductor reported in 2011 by Kanno's

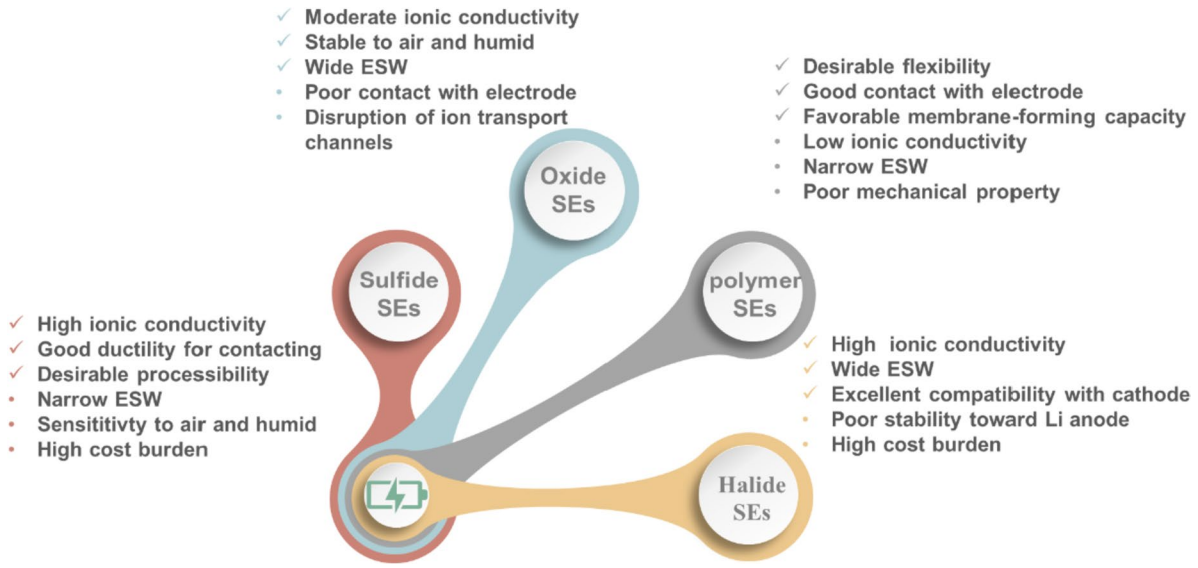

Fig. 1 Holistic aspects of four main categories of SEs performance

Table 1 Ionic conductivities of different categories of SEs for ASSLBs

	Materials	Ionic conductivity @ RT/(mS cm^{-1})
Sulfide SEs	β-$Li_7P_3S_{11}$[11]	3.2
	γ-Li_3PS_4[275]	1×10^{-4}
	β-Li_3PS_4[276]	0.16
	LGPS[17]	12
	LGPS (single crystal)[19]	27
	$Li_{10}SnP_2S_{12}$[277]	4
	$Li_{6.25}PS_4O_{1.25}Cl_{0.75}$[103]	2.8
	Li_6PS_5Cl[14]	1.9
	$Li_{5.5}PS_{4.5}Cl_{1.5}$[278]	9.4
	$Li_{5.4}PS_{4.4}Cl_{1.6}$[119]	17
	$Li_{5.3}PS_{4.3}Cl_{1.7}$[16]	8.4
	$Li_{9.54}Si_{1.74}P_{1.44}S_{11.7}Cl_{0.3}$[18]	25
	Li_6PS_5Br[14]	0.68
	Li_6PS_5I[14]	4.6×10^{-4}
Oxide SEs	LATP[279]	0.1 – 1
	LAGP[280]	$>10^{-1}$
	$Li_{1.5}Al_{0.5}Ge_{1.5}(PO_4)_3$[34]	5
	$Li_7La_3Zr_2O_{12}$[26]	0.3
	$Li_{6.75}La_3(Zr_{1.75}Nb_{0.25})O_{12}$[281]	0.8
	LLTO[282]	1
	LiPON[163]	2×10^{-6}
Polymer SEs	PEO[283]	1×10^{-3}
	PEO–LiTFSI	2.44×10^{-3}@30 °C
	Li–Cu–CNF[262]	1.5@30 °C
	PEC–LiMNT[240]	0.35
	Al_2O_3–PEO[248]	0.698@30 °C
	SIPE–PAN–NFs[259]	0.809
	PEO–GF[95]	0.12
	TTE–LP[260]	0.3
	PI–PEO–LiTFSI[54]	0.23@30 °C
	PEO–LiTFSI–nickel phosphate[255]	4.83×10^{-2}@30 °C
	LAGP–GPE[204]	0.611@30 °C
	PVDF–Palygorskite[249]	0.12
Halide SEs	Li_3YBr_6[274]	2.1
	$Li_3YBr_{5.7}F_{0.3}$[274]	1.8
	Li_3InCl_6[265]	1.49
	Li_2ZrCl_6[272]	1.0@30 °C
	Li_2HfCl_6[272]	0.5@30 °C
	Li_3YCl_6[58]	0.51
	Li_3ScCl_6[264]	3.02
	Li_3YbCl_6[263]	0.2
	$Li_{2.556}Yb_{0.492}Zr_{0.492}Cl_{5.966}$[263]	1.58
	Li_3ErCl_6[85]	0.407
	Li_3HoCl_6[270]	1.05
	$Li_3Y(Br_3Cl_3)$[60]	7.2
	Li_2ZrCl_6[266]	0.4
	$Li_{2.25}Zr_{1-x}Fe_xCl_6$[266]	1

Data are extracted from different references, and thus are with different significant digits

group demonstrated an exceptional ionic conductivity of 12 mS cm^{-1}, inspiring Japanese automakers like Toyota and Nissan to embrace sulfide SE systems [17]. Subsequent advancements led to the development of LGPS-type SEs, such as $Li_{9.54}Si_{1.74}P_{1.44}S_{11.7}Cl_{0.3}$ (LSPS) in 2016, boasting an impressive ionic conductivity of 25 mS cm^{-1}. The synthesis of LGPS with a single crystal structure reached the pinnacle, showcasing the highest ionic conductivity to date at 27 mS cm^{-1} [18, 19]. Despite LGPS achieving or surpassing LE-level ionic conductivities, researchers face lingering challenges, including interfacial properties between sulfide SEs and electrodes, a narrow ESW, Li dendrite formation, and the high cost associated with Ge. These hurdles warrant continued investigation and resolution in the pursuit of sulfide SEs' full potential in solid-state battery technology.

Oxide SEs have garnered significant attention from battery energy manufacturers like QuantumScape, WELION, Qingtao Development, and Prologium due to their superior safety compared to sulfide SEs and LEs. Typical oxide SEs, including garnets, NASICONs, and perovskites, offer advantages such as cost-effective processing and reduced sensitivity to air exposure. Among promising oxide SE candidates, garnet-type electrolytes stand out for their broad ESW, robust chemical stability at the Li – garnet interface, and high mechanical stiffness and hardness [20, 21]. Garnets are categorized based on their Li content into Li_3, Li_5, and Li_7 types, corresponding to $Li_3Ln_3Te_2O_{12}$, $Li_5La_3M_2O_{12}$, and $Li_7La_3M'_2O_{12}$, respectively, where Ln includes Y, Pr, Nd, Sm–Lu, and M includes Nb, Ta, Sb, and M' includes Zr, Sn, Hf [22–30]. The concentration of Li^+ in garnet structures significantly influences the Li^+ conduction pathway. $Li_7La_3Zr_2O_{12}$ (LLZO) garnet electrolyte has been identified as a potential catalyst for the commercialization of ASSLBs due to its moderate ionic conductivity (0.1–1 mS cm^{-1}), robust mechanical strength, chemical stability, and wide ESW [31, 32]. To stabilize the cubic phase in LLZO, substituting Zr with metals like Ta or Nb or doping with elements like Ga or Al has proven effective [33]. For example, LLZTO garnets doped with Ta exhibit satisfactory stability with Li anodes [34]. NASICONs, originating from sodium super ion conductors, have intrigued researchers since their discovery in 1976, evolving into compounds like $LiM_2(PO)_4$, where M represents Ge, Ti, Hf. $LiTi_2(PO)_4$ displays superior ionic conductivity compared to others [35–38]. Additionally, $Li_{1+x}Al_xTi_{2-x}(PO_4)_3$ (LATP) and $Li_{1+x}Al_xGe_{2-x}(PO_4)_3$ (LAGP) achieve ionic conductivities exceeding 10^{-1} mS cm^{-1} at 25 °C by partially replacing trivalent ions [39]. However, LATP's compatibility with anode materials possessing low potential properties like In and C_6Li is unsatisfactory due to Ti^{4+} reduction at 2.5 V vs. Li/Li^+ [34, 40]. Perovskite-type $Li_xM_{1/3}Nb_{1-x}Ti_xO_3$ (M = La, Nd) and $Li_{0.5}La_{0.5}TiO_3$ were first reported in 1984, and the $Li_{3x}La_{(2/3)-(1/3)-2x}TiO_3$ phase (LLTO) subsequently, where represents a

structural vacancy and relative compounds, with $0 < x < 0.16$ [41–43]. Comparing the heat generation rates of prevalent oxide SEs, the order of thermal stability toward Li anodes is LAGP < LATP < LLTO < LLZO [34]. These comparative insights into thermal stability and compatibility with anode materials highlight the nuanced strengths and limitations of different oxide SEs, informing ongoing research aimed at harnessing their full potential in advancing solid-state battery technology.

Polymer SEs possess remarkable flexibility, strong adhesion, and the capacity to form favorable membranes. These SEs typically comprise solid-state polymer hosts (PHs) with high dielectric properties and dissolved Li salts featuring low lattice energy. Among the PHs, those with functional groups play a pivotal role in dissociating and facilitating Li^+ transport. Notably, poly(ethylene oxide) (PEO) stands out as one of the most promising PHs. Li salts like Li bis(trifluoromethanesulfonyl)imide (LiTFSI), $LiBF_4$, and $LiClO_4$ significantly contribute to maintaining high ionic conductivities in polymer SEs. The pioneering work in 1973 marked the inception of the typical PEO-based SE framework [44]. In PEO-based SEs, Li^+ transport primarily occurs through ion migration and the strong complexation and dissociation effects of ether oxygen groups along the PEO chain segments within the polymer matrix [45]. Notably, due to its exceptional salt-solvating ability, low glass transition temperature (T_g), and compatibility with electrodes, PEO-based SEs have been the sole choice for large-scale EVs in the ASSLBs developed by Bolloré [6]. Further advancements have led to the development of other polymer hosts like polyvinylidene fluoride (PVDF), polyurethane (PU), polyimide (PI), and polyacrylonitrile (PAN). These hosts exhibit high ionic conductivities, good Li salt solubility, and continuous polar groups (such as $–NH_2$, –O–, –P–, and –S–) within their molecular chain segments [46–55]. However, most polymer SEs available to date fail to meet practical requirements, primarily due to their low ionic conductivity (ranging from 10^{-5} to 10^{-3} mS cm^{-1}) at RT and low Li^+ transference number (ranging from 0.2 to 0.3). To enhance the Li^+ conductivity of polymer SEs, researchers have explored various approaches, including incorporating inorganic fillers. However, due to space limitations, this review cannot delve deeper into additional relevant methods and findings in this field [56].

As a burgeoning family of SEs, halide SEs present compelling features akin to sulfide SEs, offering excellent machinability, a wide ESW spanning between 0.36 V and 6.71 V vs. Li/Li^+, desirable ionic conductivity exceeding 1.0 mS cm^{-1}, and robust chemical and electrochemical stability against oxide cathodes, as well as air/humidity tolerance [57]. Ternary compounds expressed as Li_aMX_b (where X = F, Cl, Br, I and M represents metal or non-metal elements) are the prevailing representatives of halide SEs. Significant breakthroughs in 2018 introduced halide SEs like Li_3YCl_6 and Li_3YBr_6, boasting ionic conductivities ranging from 0.51 to 1.70 mS cm^{-1} at RT [58]. Subsequent advancements led to the development of halide SEs like Li_3InCl_6, Li_3InBr_6, $Li_3Y_{1-x}In_xCl_6$, Li_xScCl_{3+x}, $Li_2Sc_{2/3}Cl_4$, showcasing ideal ionic conductivities exceeding 1.0 mS cm^{-1} at RT [59]. Notably, the ionic conductivity of $Li_3Y(Br_3Cl_3)$ has surged to an impressive 7.2 mS cm^{-1} at RT, signifying a substantial stride in this domain [60]. These impressive ionic conductivities in halide SEs hold promise for the design and advancement of next-generation ASSLBs. The choice of metal elements in halide SEs significantly influences their compatibility with Li anodes in ASSLB applications. Halide SEs featuring non-metal elements tend to demonstrate a narrower ESW, exemplified by Li_3OCl (up to 2.55 V vs. Li/Li^+). In contrast, those incorporating metal elements exhibit a broader ESW, such as Li_3YCl_6 (up to 4.21 V vs. Li/Li^+) [61, 62]. Due to their advantageous properties—prominently, exceptional ionic conduction and wide ESWs—halide SEs with metal elements have garnered escalating interest. These halide SEs can be categorized based on the type of metal element involved: (i) $Li_aM_iX_b$ featuring group 3 elements like Sc, Y, La–Lu; (ii) $Li_aM_{ii}X_b$ involving group 13 elements such as Al, Ga, and In; and (iii) $Li_aM_{iii}X_b$ encompassing divalent metal elements like Mg, Ti, Cu, Fe [59]. However, it's important to note that the reduction potential of halide SEs still surpasses 0.6 V (vs. Li/Li^+), indicating that direct coupling with Li metal anodes remains a challenge.

While the performance of SEs remains a crucial factor for achieving efficient Li^+ transport and high electrochemical performance in assembled ASSLBs, it's no longer the sole determinant. The establishment of a preferred interface, ensuring robust stability between SEs and electrodes, has emerged as a decisive element in meeting the commercial demands for ASSLBs. Most SEs encounter challenges in maintaining complete stability when faced with highly reductive Li anodes, creating bottlenecks for the practical application of ASSLBs. Recent papers have extensively covered protection methods specifically for the Li anode side [63–66], leaving a substantial gap in addressing interfacial issues across all SE categories. This discussion aims to delve into both the Li anode side and SEs side, highlighting the intricate interface stability challenges and proposing corresponding solutions. Our objective is to present the most promising outcomes in research. The exploration begins by uncovering the failure mechanisms within the interface between Li anodes and SEs, encompassing chemical side reactions, poor physical contact, and the formation of Li dendrites. Additionally, we emphasize design strategies aimed at stabilizing the interface between Li anodes and the four main types of SEs—sulfide, oxide, polymer, and halide SEs—pertaining to ASSLBs within the

past decade. Lastly, we offer ideas and suggestions for interfacing different SE types with Li anodes and propose views and recommendations for the future development of ASSLBs. This comprehensive approach aims to address and bridge critical gaps in understanding and overcoming interface challenges, ultimately propelling advancements in ASSLB technology.

2 Issues of Li–Solid Electrolyte Interfaces/Interphases

In the realm of batteries, interfaces and interphases represent distinct yet crucial concepts. The interface serves as the primary site for electron/ion exchange in ASSLBs, where the anode/cathode meets the SEs, creating a sudden phase discontinuity experienced by both the bulk anode/cathode and bulk SEs. Conversely, the interphase emerges as a result of irreversible reactions between SEs and the anode/cathode, aiming for superior ionic conduction and electronic insulation [67]. The allure of Li metal, with its exceptionally high specific capacity of ~ 3 860 mAh g^{-1}, has long been perceived as the holy grail in the landscape of commercial LIBs. Additionally, Li metal boasts a notably low potential of − 3.04 V vs. the standard hydrogen electrode (SHE) and a low density of 0.534 g cm^{-3}, significantly contributing to the achievement of ultrahigh energy density in ASSLBs [68]. While incorporating Li anodes in ASSLBs is pivotal for enhancing energy density, the inherent low electrochemical potential of Li anodes leads to their reactivity with most SEs. This reactivity often triggers the nucleation and growth of Li dendrites, ultimately leading to cell short circuits. Unlike LEs, SEs lack the ability to infiltrate voids and gaps, resulting in undesirable physical contact between SEs and electrodes. Consequently, the primary challenge in ASSLBs lies in ensuring the stability of the interface between Li anodes and SEs. This challenge is directly linked to issues of side reactions, contact area, and the formation of Li dendrites, posing significant hurdles in advancing the performance and safety of these batteries.

Securing an ideal interphase that encompasses robust mechanical, chemical, and electrochemical properties holds immense significance. Such interphases are pivotal in establishing a stable interface that mitigates severe side reactions, maintains low interfacial impedance, and enables a high critical current density (CCD). These attributes play a crucial role in restraining side reactions, facilitating the swift transport of Li^+, and suppressing the formation of Li dendrites at the interface. Addressing several challenges inherent in Li–SE interfaces/interphases is imperative before their practical implementation can be realized.

2.1 Side Reactions

The ESW of SEs delineates their capacity to resist oxidation or reduction by extracting or inserting ions and electrons. Meeting the escalating energy density demands of ASSLBs necessitates a high operating voltage, underscoring the need for SEs to retain stability across the widest possible ESW. Assessing the chemical stabilities of both LEs and SEs is often predicted by using an energy diagram, where the ESW is gauged by the relative energy of "E_g" [69]. Oxidation events occur when the top of the valence band (VB) surpasses the chemical potential of the cathode (μ_C), while reduction reactions are triggered when the bottom of the conduction band (CB) falls below the chemical potential of the anode (μ_A). The ESW, positioned between the bottom of CB and the top of VB in SEs, is determined by their oxidation and reduction (such as S and P redox for thiophosphate-based SEs, and O and Zr redox for garnet) [70]. A wide ESW is pivotal for achieving high-performance cells, often achieved by lowering the highest occupied molecular orbital (HOMO) and raising the lowest unoccupied molecular orbitals (LUMO) to counteract sluggish decomposition kinetics [71]. Regarding SEs and the cathode/anode interface, during the Li^+ stripping/plating process, a cathode electrolyte interphase (CEI) interlayer and an anode solid electrolyte interphase (SEI) interlayer are formed. The stability issues at these interfaces significantly impact the state and energy density of ASSLBs, though beyond the review's scope. The formation of SEIs inevitably involves SE consumption and impedance increase, directly related to the reduction products of SEs. The ESW of commonly used SEs, along with their application prospects, is summarized in Fig. 2, providing a foundation for interpreting interface stability between Li and SEs. Notably, Li binary compounds merit a separate classification for summarization (Fig. 2, blue–green bars at the bottom). Extensive computational and experimental research into the ESW not only delineates the operating voltage range for various SE types but also elucidates oxidation and reduction processes. For example, the ESW of LGPS spans from 1.71 to 2.14 V vs. Li/Li^+, with LGPS lithiated and reduced to Li_4GeS_4, P, and Li_2S at 1.7 V, and oxidized to Li_3PS_3 and GeS_2 at 2.14 V [32].

According to Wenzel et al., the Li–SEs interface can be classified into three distinct categories: the thermodynamically stable interphase, the mixed ionic and electronic conducting (MIEC) interphase, and the metastable solid–electrolyte interphase (M–SEI), as illustrated in Fig. 3 [72].

(1) Thermodynamically stable interphase. Figure 3a depicts a scenario where the Li anode and SEs exhibit stability with each other, forming a flat and clear 2D interface devoid of any side reactions. Li binary com-

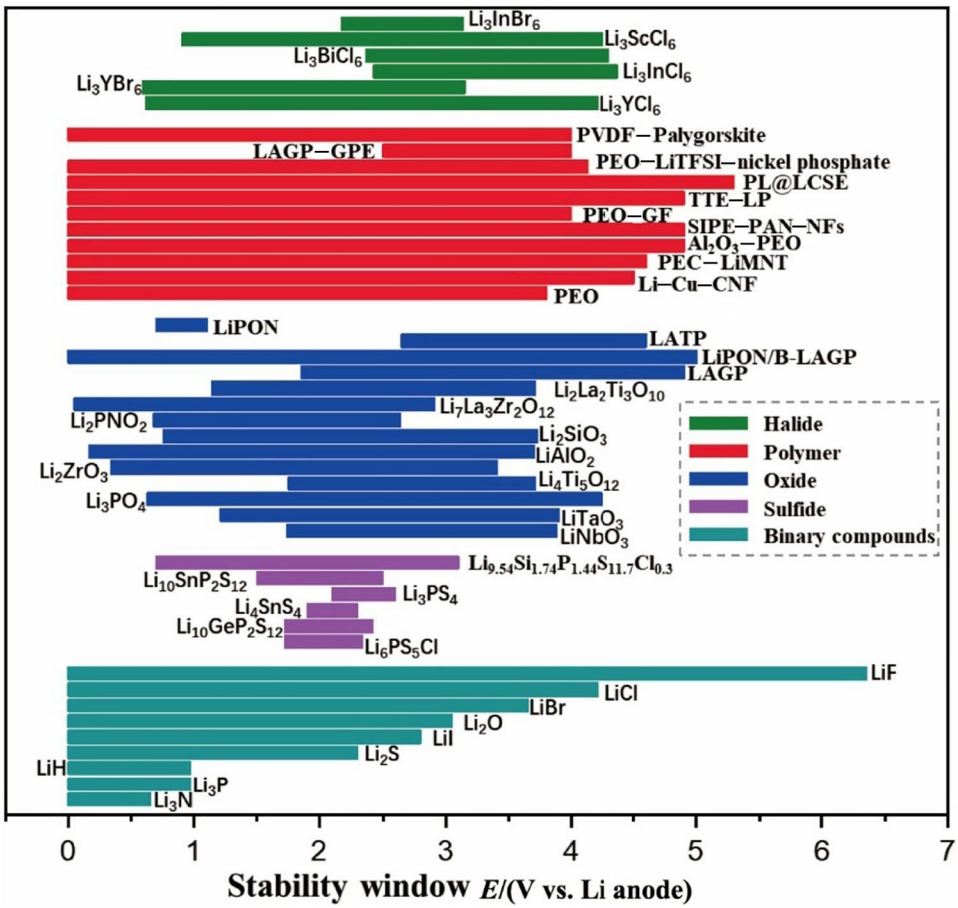

Fig. 2 Electrochemical stability window of examples from various SEs (binary compounds, sulfide, oxide, polymer and halide)

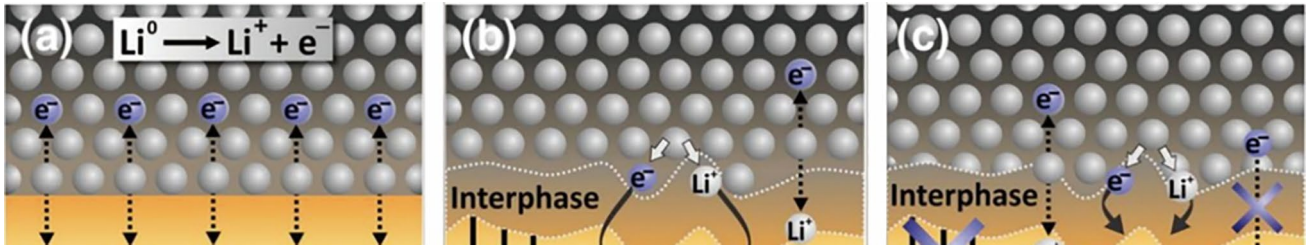

Fig. 3 Interfaces between the Li anode and SEs can be categorized into three key types: **a** thermodynamically stable interface; **b** mixed ionic and electronic conducting (MIEC) interphase; **c** metastable solid–electrolyte interphase (M–SEI). Reprinted with permission from Ref. [72]. Copyright © 2015, Elsevier

pounds stable with the Li anode undergo decomposition at 0 V vs. Li/Li$^+$ (Fig. 2a, cyan bars), signaling a stable interphase [73]. Common binary SEs such as Li_3N, Li_2O, Li_3P, and LiX (where X represents halide elements) are stable with the Li anode, although they typically exhibit low ionic conductivity, rendering them unsuitable as standalone SEs for ASSLBs [74].

(2) MIEC interphase. Figure 3b illustrates the occurrence of chemical reactions between the Li anode and SEs, resulting in a thermodynamically unstable interface. This scenario often leads to the formation of an electronic conductive interphase, fostering an electronic pathway for reduction at the anode–SEs interface. This phenomenon contributes to gradual Li dendrite formation, ultimately leading to short circuits in ASSLBs, a significant impediment to practical use. However, in the case of PEO-based SEs, Wan et al. discovered that an in situ formed MIEC interphase, comprising the high ionic conductivity of Li_3N and the electronic conductor Mg between PEO and Mg_3N_2 intermediary, effectively alleviated concentration gradients and enhanced uni-

form Li deposition [75]. In contrast, without the MIEC interlayer, anions tend to accumulate on the Li anode.

(3) M–SEI. Figure 3c showcases chemical reaction products exhibiting low electronic conductivity or insulative properties, limiting the continuous growth of the M–SEI. This metastable interphase bears similarity to the SEI observed in LEs-based cells.

In terms of sulfide SEs, Li_3PS_4-based glasses, glass ceramics, and Li argyrodites demonstrate greater stability than highly conducting sulfide SEs like LGPS and LSPS when exposed to the Li anode in ASSLBs. When Li metal interacts with Li_3PS_4-based glasses, glass ceramics, and argyrodites, the decomposition products are Li_2S and Li_3P. The former compound is insulative, while the latter is ionic conductive, indicating the formation of an M–SEI. On the other hand, LGPS shows a favorable decomposition energy (− 1.2 eV atom^{-1}), resulting in decomposed products of insulative Li_2S, ionic conductive Li_3P, and electronic conductive Li–Ge alloy after contact with the Li anode, indicating an MIEC interphase [74, 76]. The accumulation of these products increases interfacial impedance and encourages continuous Li dendrite growth, leading to eventual cell failure. This behavior is similar in sulfide SEs containing Si, Sn, and Sb. Li_3PS_4-based glasses, glass ceramics, and argyrodites can serve as protective layers between the Li anode and highly conducting sulfide SEs like LGPS and LSPS. LLZO, known as an ionic conductor, shows a decomposition close to 0 V, suggesting greater stability with Li metal compared to sulfide SEs. However, slight reduction of Zr^{4+} in LLZO by Li can elevate electronic conductivity in the interphase, leading to the formation of an MIEC interphase [77]. LPON reduced by Li metal produces Li_3P, Li_2O, and Li_3N, indicating an M–SEI favorable for Li^+ transport without blocking electron conduction, described as a metastable interphase, enabling a long cycle life of around ≈10 000 cycles [78, 79]. NASICON-type oxide SEs containing Ti, Ge, and Al, such as Ti^{4+} in LLTO, Ti^{4+} and Al^{3+} in LATP, Ti^{4+}, Ge^{4+}, and Al^{3+} in LAGP, are prone to forming MIEC interphases with Li metal via reduction reactions, making them unsuitable for use with the Li anode [80]. Most polymer SEs are stable with the Li anode, except for poly(*N*-methyl-malonic amide) (PMA) and polyacrylonitrile (PAN) [81, 82]. Halide SEs, due to high valence metal elements, exhibit high reactivity with the Li anode [83, 84]. For instance, $Li_aM_iX_b$ exhibits a reduction onset of 0.41–0.92 V, while $Li_aM_{ii}X_b$ demonstrates a higher value of 1.06–0.92 V [62]. When Li_3YCl_6 contacts Li metal, it decomposes into Li_3Y (an electronic conductor) and LiCl (an ionic conductor), indicating an MIEC interphase [85]. The metal component is crucial in determining the reduction onset of halide SEs.

2.2 Poor Physical Contact

Compared to the effective contact between sufficient LEs and electrodes, establishing a solid connection between SEs and electrodes is notably more intricate. Inadequate contact between the Li anode and SEs results in interfacial issues like the formation of Li dendrites, elevated charge transfer impedance, and uneven current distribution. Even with sulfide SEs known for their pliability, which aids in compacting the Li anode and SEs, they still struggle to entirely fill gaps, leading to subpar physical contact. Applying moderate stack pressure during cycling becomes essential to enable cycling in ASSLBs by preventing void formation [86]. Most electrochemical tests in ASSLBs employ external pressure to counteract the adverse effects of insufficient solid–solid contact and high interfacial impedance. However, the specific parameters of applied external pressure vary based on the properties of sulfide SEs and electrodes and lack uniformity.

Evaluating the contact performance between solid-state electrodes and SEs involves assessing wettability and cyclic stress. Inadequate physical contact between the Li anode and SEs often arises from poor wettability, which can be gauged by the contact angle between molten Li and SEs. Contact angles below 90° signify good wettability, representing a lithiophilic interface, while angles larger than 90° denote poor wettability, indicating a lithiophobic interface [87]. Oxide SEs, typically brittle when assembled, exhibit weak interfacial compatibility. Within the garnet family, while they demonstrate remarkable electrochemical stability with the Li anode, the metallic Li anode showcases poor wettability against garnets, hindering further applications in ASSLBs [88]. LLZO, boasting an ionic conductivity of 6.46×10^{-1} mS cm^{-1}, tends to develop impurities (like LiOH and Li_2CO_3) in air, leading to a significant reduction in conductivity to 3.62×10^{-1} mS cm^{-1}, adversely affecting wettability. Surface impurity removal as a pretreatment is necessary to enhance LLZO's wettability with Li metal [74].

Furthermore, during the repeated plating and stripping processes of the Li anode or Li alloy anode (e.g., Li–Si or Li–Sn), cyclic stress occurs due to volume expansion and compression, resulting in void formation and contact loss. This insufficient contact can create uneven Li^+ flux distribution, facilitating Li dendrite formation. These dendrites may penetrate SEs through microdefects like pores or grain boundaries, leading to short circuits, especially at relatively low current densities [89]. Therefore, high-quality SEs should be capable of reversible deformation to accommodate anode volume changes, maintaining close contact for sustaining capacity and cycling performance in ASSLBs [90].

The mechanical properties of SEs significantly influence the physical contact between electrodes and SEs. For instance, sulfide SEs lacking metal additives, like LPSC, exhibit better physical contact with Li compared to LGPS

due to increased hardness from metal additives. Polymer electrolytes outperform other SE categories, establishing an intimate interface with enhanced flexibility [91].

2.3 Li Dendrites

Li dendrites pose a significant challenge in addressing anode interfacial issues within secondary batteries, capable of causing severe short circuits. ASSLBs were initially devised to couple high-energy Li metal with SEs, aiming to leverage a robust mechanical barrier to prevent the infiltration of problematic Li dendrites through the SEs. However, despite this design, Li dendrite growth remains a critical factor in short circuits within ASSLBs, sometimes occurring even more rapidly than in cells using LEs. The exact mechanisms driving Li dendrite formation are multifaceted and not yet fully understood, as they can either grow from the Li anode toward the SEs or originate directly within the SEs. Previous studies suggest that the primary causes of Li dendrites in ASSLBs encompass interface defects, the inherent mechanical properties of SEs, and the critical current for stripping (CCS).

Anode interfacial defects, such as voids and grain boundaries, typically arise due to inadequate physical contact, volume fluctuations, and low compacting density. When the applied current density exceeds a moderate range, deposited Li tends to nucleate and propagate primarily within the voids and grain boundaries within the SEs. This infiltration can extend throughout the entire SE, culminating in cell failure. The formation and growth of Li dendrites are not confined solely to grain boundaries and cracks but can also occur within amorphous SEs lacking distinct grain boundaries [92, 93].

The well-known Monroe–Newman model outlines that inhibiting Li dendrites becomes feasible when the shear modulus of SEs surpasses twice that of Li metal, which is around 4.8 GPa at RT [94]. As a result, SEs generally need to have a shear modulus higher than 9.6 GPa at RT. However, even inorganic SEs like LLZO (100 GPa) and β-Li_3PS_4 (12 GPa) possess shear moduli exceeding 9.6 GPa at RT, yet Li dendrite growth remains prevalent [90]. For garnets, an excessively high shear modulus can lead to mechanical flaws and fractures due to strain experienced during cycling [68]. It's important to note that the Monroe–Newman model is only applicable to interfaces devoid of defects or irregularities in SEs [66]. Consequently, Li dendrite growth is notably pronounced in the inherently softer nature of polymer SEs compared to other inorganic SEs, despite the positive traits such as flexibility and excellent processability they offer. Despite extensive efforts to enhance the elastic modulus, it still remains considerably lower than that of the Li anode for all PEO-based SEs, presenting a major challenge for the utilization of polymer SEs [95].

The CCD, which denotes the maximum permissible current density without leading to a short circuit, can be further categorized into CCD for plating (CCP) and CCS. Among these, CCS holds greater significance as it is a pivotal factor in causing ASSLBs failure due to the emergence of Li dendrites, superseding the importance of CCP [96]. Exceeding the CCS threshold results in uneven Li stripping, leading to various drawbacks including void formation on the Li anode surface, diminished solid–solid contact area, escalated local current density at contact points, and ultimately, the short circuit of ASSLBs. External pressure tests reveal that moderate external pressure enhances the CCD. At the Li–SEs interface, it's not diffusion but rather creep that acts as the actual mechanism for Li^+ migration. Li metal possesses a yield strength of ≈0.8 MPa, which surpasses the threshold at which Li starts to creep within SEs' pores, eventually fostering Li dendrite formation and culminating in a short circuit [86]. The U.S. Department of Energy aims for an ASSBs power density exceeding 33 kWh L^{-1}, necessitating a CCD of more than 10 mA cm^{-2} to attain this benchmark [97]. However, currently employed ASSLBs typically operate within a limited CCD range of 1–2 mA cm^{-2}, presenting a challenging path to achieving the desired high power density and expanded CCD. Addressing anode–SEs interfacial issues, curbing Li dendrite formation, boosting CCD, and reducing interfacial resistance require urgent attention through numerous dedicated studies.

On the whole, Li dendrite formation and growth, SEI properties, and volume changes within the Li anode pose the primary bottlenecks at the Li anode–SEs interface, as depicted in Fig. 4. Consequently, key strategies revolve around interlayer insertion to segregate the Li anode and SEs, modifications to the Li anode, and SEs optimization to prevent side reactions and Li dendrite growth while preserving SEs' ionic conduction. Here's a summary of recent strategies aimed at fostering efficient and secure ASSLBs based on the preliminary analysis of these challenges.

3 Interfacial Engineering Toward Li and Sulfide SEs

Based on recent studies and earlier discussions, sulfide SEs showcase exceptional ionic conductivity, yet their high reactivity and limited ESW pose significant challenges for sulfide-based ASSLBs at the anode interface. These encompass parasitic reactions, subpar contact, low CCD, and the growth of Li dendrites. A variety of successful strategies have emerged to combat these persistent interfacial concerns between Li and sulfide SEs. These strategies involve incorporating stable interlayers, fine-tuning SE properties, and alloying the Li anode, all aimed at resolving the intricate interface issues between Li and sulfide SEs.

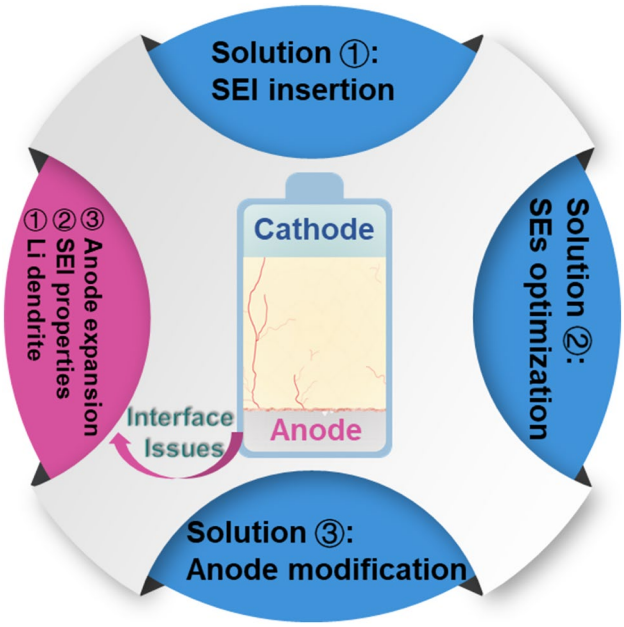

Fig. 4 Illustrative representation of key interfacial challenges between the Li anode and SEs, along with effective solutions

3.1 Insertion of Interlayer

Certainly, one prevalent approach involves incorporating an artificial interlayer to mitigate parasitic reactions and prevent direct contact between the Li anode and sulfide SEs, all while minimizing any significant increase in cell impedance. To effectively serve this purpose, these interlayers must fulfill specific criteria: (i) exhibiting thermodynamic stability with the Li anode; (ii) demonstrating ionic conductivity while being electronically insulative (or exhibiting low electronic conductivity); and (iii) possessing good mechanical ductility. Based on their preparation methods, these artificial interlayers can be categorized into two types: the in situ SEI interlayer and the ex situ buffer interlayer.

3.1.1 In Situ SEI Interlayer

The incorporation of an in situ SEI interlayer serves to prevent parasitic reactions and the formation of mixed ionic and electronic conducting interphases while preserving the ionic conductivity of sulfide SEs. Addressing the challenges associated with the narrow ESW and contact stability with both ambient environment and Li metal is crucial for highly active sulfide SEs in practical applications. Researchers have dedicated significant efforts toward achieving stability at the anode interface, aiming to establish a uniform and robust in situ layer. For instance, Sun et al. demonstrated an in situ generated, air-stable, and highly ionic conductive Li_xSiS_y interphase layer on Li metal, enhancing the stability of Li metal against both air exposure and sulfide SEs. This Li_xSiS_y interphase comprises Li_2SiS_3/Li_4SiS_4 and Li_2S; the former facilitates rapid Li^+ migration through the protective layer, while the latter ensures direct contact with Li metal without triggering parasitic reactions (Fig. 5A) [98].

The chemical composition of the interphase formed at the anode–SE interface profoundly influences both the CCD value and the long-term cycling performance. Binary SEI interlayers like Li_2S, Li_3P, Li_3N, LiF, LiCl, LiBr, and LiI demonstrate high interfacial energy, negative decomposition energy, and acceptable electronic conduction, making them favorable for establishing a thermodynamically stable interphase. For instance, when the Li anode is coated with Li bis(fluorosulfonyl)imide (LiFSI) and brought into contact with Li_3PS_4, an in situ formation of a LiF-rich SEI layer effectively inhibits Li dendrites, resulting in an increased CCD exceeding > 2 mA cm^{-2} at RT, as showcased in Fig. 5B(a) and Fig. 5B(b) [99]. Another method employs the in situ liquid phase infiltration of methoxyperfluorobutane (HFE) into sulfide SEs, generating a stable interphase comprising LiF at the Li anode–sulfide SE interface, effectively suppressing Li dendrites, as depicted in Fig. 5B(c) and Fig. 5B(d) [100]. Sun et al. synthesized $LiPSCl_{0.3}F_{0.7}$ as an SE via fluorination, yielding a stable LiF interphase toward Li metal, enabling ultra-stable Li^+ transport even under high current densities [101]. Moreover, in Fig. 5C, a Li_3PO_4–Li_3N hybrid interphase, exhibiting desirable ionic conduction and sufficiently low electronic conduction, was constructed on the Li surface through a chemical reaction involving $LiNO_3$/H_3PO_4 (NPO). The resulting cell displayed commendable cycling performance at 1 mA cm^{-2} [102]. Density function theory (DFT) calculations revealed that Li_3PO_4 possesses the highest interfacial energy against Li metal, while Li_3N exhibits the highest adhesion energy. Wang et al. introduced trace amounts of propylene carbonate (PC) to form a stable and robust SEI with LiCl-rich LPSC, not only enhancing the Li–SE interface for Li^+ transport but also impeding undesirable parasitic reactions and Li dendrite growth [103]. The assembled ASSLBs with $LiCoO_2$|$Li_{6.25}PS_4O_{1.25}Cl_{0.75}$|Li showcased a specific capacity of 116 mAh g^{-1} under a 1 C rate for 200 cycles.

As a remarkable milestone in ASSLB research, LGPS boasts ultrahigh ionic conduction comparable, and sometimes superior, to LEs at RT [17]. Yet, the reduction of Ge^{4+} in LGPS against the Li anode can accelerate LGPS decomposition. However, recent research has employed an in situ SEI interlayer to address this concern, yielding promising outcomes. Several effective strategies have emerged to foster a stable and high Li^+ transport SEI between LGPS and Li metal. One of these approaches involves leveraging in situ gelation, electrochemical deposition of LEs on the Li anode, and chemical modification of the Li anode. In the Li–LGPS interface realm, substantial efforts have been dedicated to crafting an in situ gel polymer interlayer (GPI) using in situ

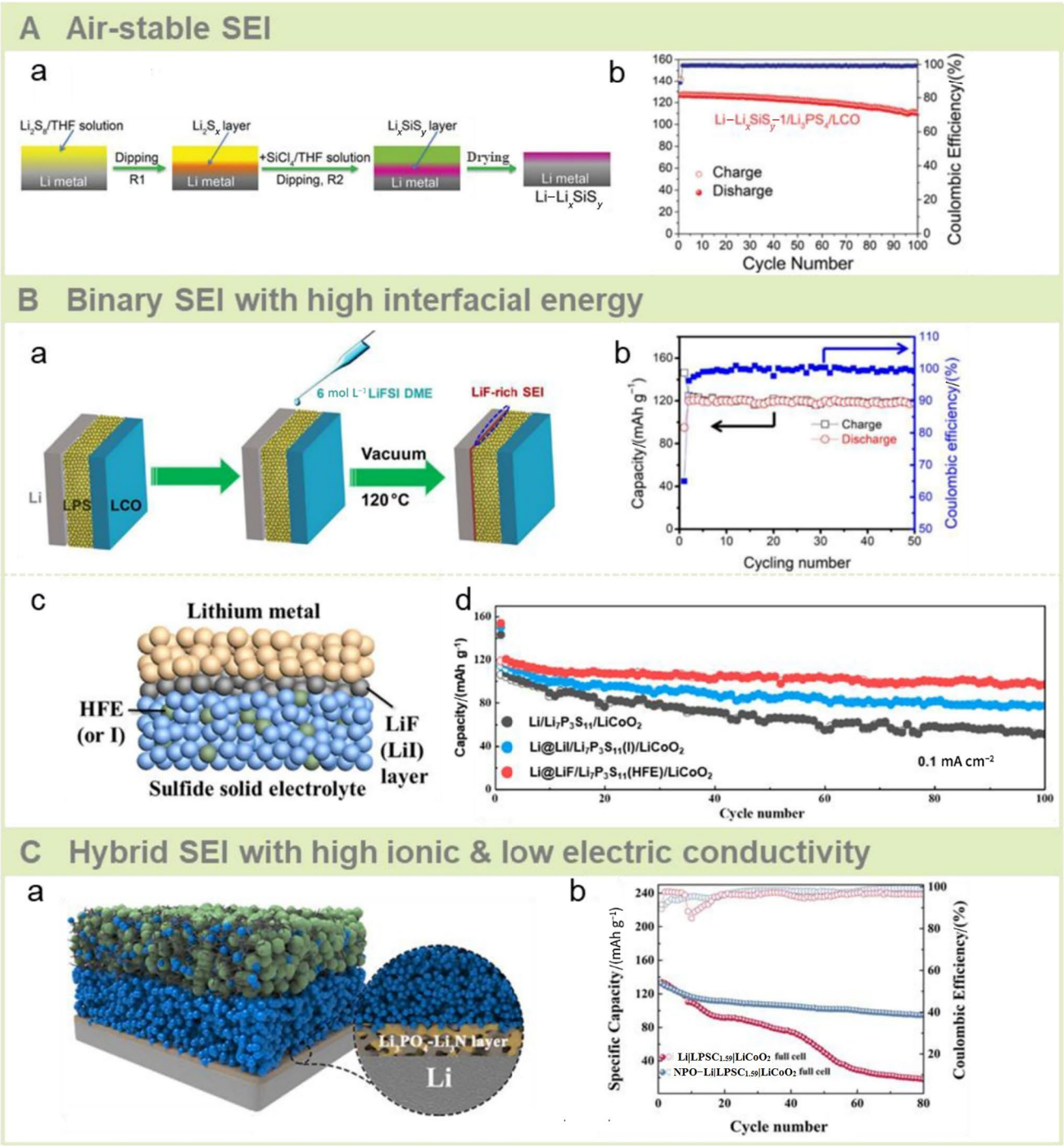

Fig. 5 Insertion of stable in situ SEIs between Li and sulfide SEs. **A** An air stable SEI formed at the anode interface. **a** Schematic illustration of formation processes for the in situ Li_xSiS_y interlayer. **b** Cycling performance of Li–Li_xSiS_y|Li_3PS_4|$LiCoO_2$ cells. Reprinted with permission from Ref. [98]. Copyright © 2019, John Wiley and Sons. **B** A stable in situ SEI composed of binary materials formed at the anode interface. **a** Schematic illustration of LiF-rich in situ interlayer's formation process between Li_3PS_4 SEs and the Li anode. **b** Cycling performance of Li|LiFSI@Li_3PS_4|$LiCoO_2$ at 0.3 mA cm^{-2} at RT. Reprinted with permission from Ref. [99]. Copyright © 2018, Chunsheng Wang. **c** Schematic illustration of a stable SEI LiF interlayer formation process. **d** Cycling performance of assembled ASSLBs including Li|$Li_7P_3S_{11}$|$LiCoO_2$, Li|$Li_7P_3S_{11}$(I)|$LiCoO_2$ and Li/$Li_7P_3S_{11}$(HFE)|$LiCoO_2$ at 0.1 mA cm^{-2}. Reprinted with permission from Ref. [100]. Copyright © 2018, Elsevier. **C** In situ SEI interlayer formed at the Li anode interface. **a** Schematic diagram of the modified interface with a Li_3PO_4–Li_3N composite SEI. **b** Cycling performance of NPO–Li|$LPSC_{1.59}$|$LiCoO_2$ batteries and Li|$LPSC_{1.59}$|$LiCoO_2$ batteries. Reprinted with permission from Ref. [102]. Copyright © 2022, Elsevier

polymerization technology. This elastic GPI exhibits desirable ionic conduction, enhancing physical contact, promoting uniform Li^+ transport, and curbing parasitic reactions and Li dendrite formation [104]. Similarly, in Fig. 6A, a dual-layered structure (GI-P) was created via ring-opening polymerization on the Li metal surface. This structure consists of an inorganic species (the bottom layer) and a polymer (the upper layer), effectively restraining Li dendrites and fostering a deformable SEI [105]. Electrochemically reducing LEs at the Li–sulfide SE interface can generate a nanocomposite interlayer, as depicted in Fig. 6B. Gao et al. demonstrated an in situ preparation of a nano-level SEI composed of organic and inorganic Li salts on Li metal, effectively curbing LGPS reduction reactions during extensive cycling [106]. The stable composite interlayer enabled electrodeposition of the Li anode for over 3 000 h. Another ingenious strategy involves employing an interlayer with high ionic conductivity on the Li anode through chemical modification. Zhou et al. employed a smart chemical iodine vapor deposition method to create an in situ densely interweaving structural LiI interphase. This LiI SEI serves as a bridge between Li and LGPS, exhibiting negligible electronic conductivity yet high ionic conductivity and mechanical strength. This approach showcased effective Li dendrite suppression and outstanding cycling performance even under challenging conditions [107]. Further exploration led to the investigation of a manipulated LiH_2PO_4 interphase via the chemical reaction of H_3PO_4 in tetrahydrofuran solvents with Li metal. The resulting LiH_2PO_4 interlayer on the Li surface demonstrated enhanced protection and intimate physical contact, indicating improved stability between the Li anode and LGPS, as illustrated in Fig. 6C [108].

3.1.2 Ex Situ Buffer Interlayer

In terms of ex situ buffer interlayers, the integration of a protective layer has emerged as a common approach to stabilize both Li metal and sulfide SEs. However, considering the discussed mechanism of Li^+ transport primarily via creep, substantial pressure is required [96, 109]. Nonetheless, extremely high stack pressure can promote Li dendrite formation and lead to short circuits in ASSLBs.

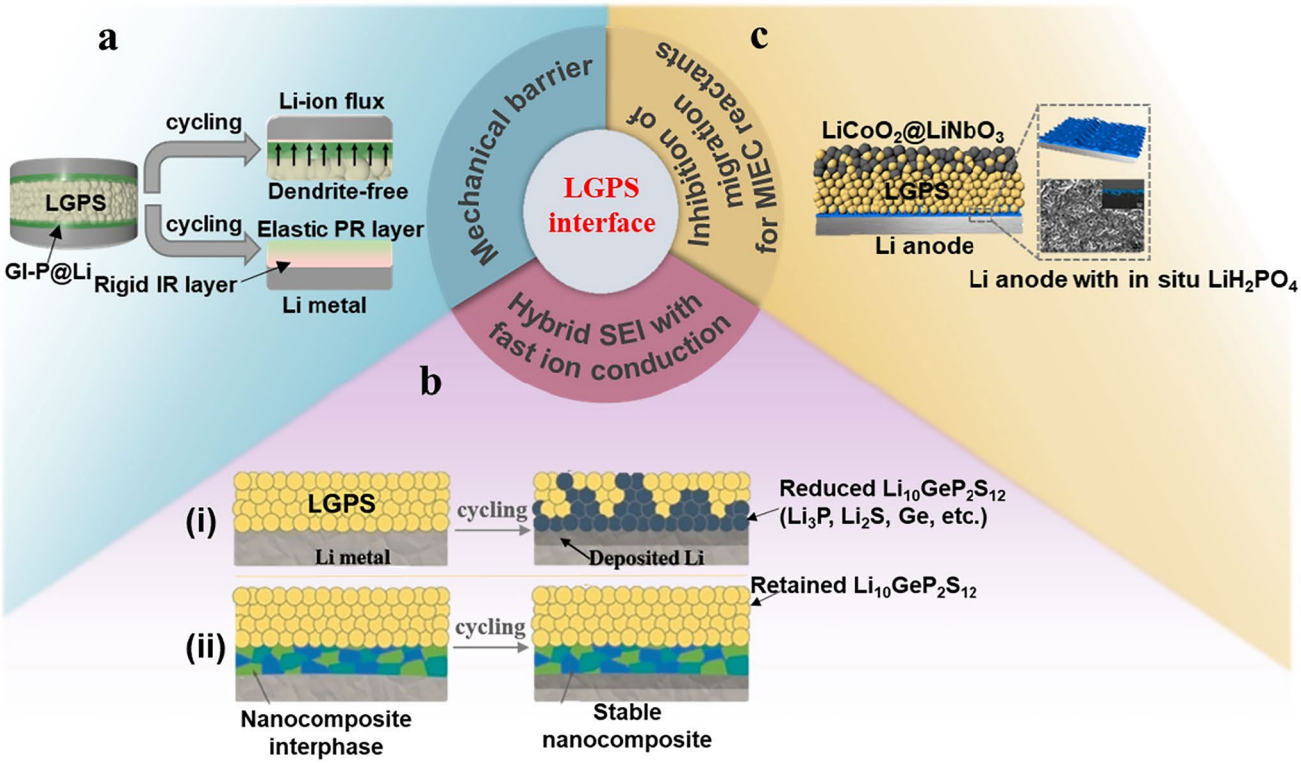

Fig. 6 Insertion of a stable in situ SEI between Li and LGPS. **a** Schematic illustration of the Li–sulfide SE interface with GI-P@Li and with bare Li, where PR and IR represent polymer-rich and inorganic-rich, respectively. Reprinted with permission from Ref. [105]. Copyright © 2022, Elsevier. **b** Schematic diagram of composite Li salts as an in situ interphase for improving the anode interface: (i) undesirable interface between Li and LGPS without a composite interlayer; (ii) desirable interface between Li and LGPS with composite Li salts as a protective interlayer. Reprinted with permission from Ref. [106]. Copyright © 2018, John Wiley and Sons. **c** $LiCoO_2$|LGPS|Li cells with the LiH_2PO_4 interlayer between the anode and SE. Reprinted with permission from Ref. [108]. Copyright © 2018, ACS publications

To address this challenge, the mechanical constriction mechanism has introduced a graphite-protected Li metal (Li/G) setup (Fig. 7A) that accommodates high external stack pressures [110–112]. The Li/G composite anode has demonstrated exceptional performance across different sulfide SE systems, showcasing an 82% capacity retention for an SE system composed of LPSC–LSPS–LPSC after 10 000 cycles at a high rate of 20 C. Additionally, a multi-LPSC composite system exhibited an ultra-high capacity retention of 95% over 700 cycles at 55 °C. Moreover, solid-state plastic crystal electrolytes, known for their high ionic conductivity at RT, have been identified as promising interlayers to address interfacial challenges [113, 114]. For instance, the succinonitrile (SN)-based plastic crystal electrolyte (PCE) interlayer (Fig. 7B) offers good thermal stability, nonflammability, and chemical compatibility with the Li anode [115]. Assembled Li-S batteries with a PCE interlayer showcased outstanding high initial capacity and extremely high capacity retention after 100 cycles. Introducing Al_2O_3 as an interlayer via atomic layer deposition (ALD) has been another successful strategy to prevent parasitic reactions by forming a thermodynamically stable Li_2O–Al_2O_3 phase for various SE types [116–118]. Yao et al. suppressed short circuits in Li–Al_2O_3|$Li_{5.4}PS_{4.4}Cl_{1.6}$|Al_2O_3–Li symmetric cells by sputtering a 400 nm-thick Al_2O_3 interlayer at the interface between the Li anode and the $Li_{5.4}PS_{4.4}Cl_{1.6}$ thin membrane electrolyte [119]. Molecular layer deposition (MLD) has also proven effective; for instance, an alucone layer was created via MLD on the anode interface to block electron transfer, suppressing side reactions and Li dendrites at the anode interface (Fig. 7C) [120]. Additionally, binary composite compounds with acceptable ionic conduction and high interfacial energy have served as effective layers to ensure stable interphases for Li^+ transport and Li dendrite suppression during cycling. A Li_3N–LiF composite designed for a dendrite-free Li–Li_3PS_4 interface exhibited exceptional performance with an ultra-high value of CCD, even at an outstanding area capacity (6.0 mAh cm^{-2}) (Fig. 7D) [121]. Furthermore, the insertion of an Au thin film by Masahiro Tatsumisago proved advantageous in inhibiting side reactions within the Li anode and Li_3PS_4, exhibiting excellent rate performance at elevated temperatures [122]. Other types of SEs have also been explored as interlayers. For instance, a LiPON thin amorphous interlayer introduced via radio frequency sputtering by Grovenor et al. improved the wettability between molten Li and LPSC and reduced interfacial resistance, increasing CCD for Li/LiPON|LPSC|LiPON/Li symmetric cells to 4.1 mA cm^{-2}, a promising value for practical applications of ASSLBs [123].

3.2 Optimization of Sulfide SEs

Optimizing sulfide SEs involves modifications and structural designs aimed at reducing residual electronic conductivity and broadening the ESW. This process holds significant importance in restraining the formation of lithium dendrites.

3.2.1 Doping of Exotic Elements

Strengthening the weak P–S bonds is crucial to enhancing the stability of sulfide SEs. Modifying the composition of these SEs offers a straightforward method to boost their thermodynamic stability and widen the ESW while preserving their ionic conduction properties. The β-Li_3PS_4, a low-symmetry crystalline material, boasts high ionic conductivity but faces instability at RT, limiting its practicality. An effective approach involves anion doping to establish a stable interface between sulfide SEs and Li anodes [31, 124]. The substitution of sulfur with oxygen in β-Li_3PS_4, suggested by Chen's group based on bond valence and DFT, strengthens the P–O bonds, offering increased stability without compromising ionic conductivity. This strategy not only stabilizes the medium-temperature crystal phase but also facilitates smoother ion transport pathways, transitioning from a 2D to 3D transport behavior. This advancement preserves the wide ESW of β-Li_3PS_4. This substitution technique extends to argyrodites as well [125, 126]. Shao et al. [103] explored $Li_{6.25}PS_4O_{1.25}Cl_{0.75}$, demonstrating exceptional cycling performance when paired with Li anodes and $LiCoO_2$, retaining the pristine argyrodite's exceptional ionic conduction. This modification led to the in situ formation of a Li_3PO_4 interphase, serving as an SEI interlayer at the anode interface, as illustrated in Fig. 8A. This O-doped argyrodite showcased superior capabilities in suppressing Li dendrites and exhibiting resilience against air and humidity. Beyond single atom doping or substitution, various oxides like ZnO[127, 128], Li_2O[129, 130], Sb_2O_5[131], P_2O_5[132] and Nb_2O_5[133] have been employed to reinforce the stability of sulfide SEs against both air and Li anodes, as depicted in Fig. 8B. Notably, incorporating ZnO atoms onto the sulfur site not only enhances the SEs' stability but also leads to the formation of a highly conductive LiZn alloy, effectively curbing the nucleation and growth of Li dendrites without sacrificing ionic conductivity.

LiX, encompassing various halide elements, stands out as an ideal dopant for enhancing sulfide SEs. This group of dopants contributes significantly to widening the ESW, refining compatibility with the Li anode, and augmenting ionic conductivity. Among these halides, the ionic conductivity follows the order: LiI > LiBr > LiCl > LiF [134]. Liang et al. introduced LiI into Li_3PS_4, resulting in the creation of

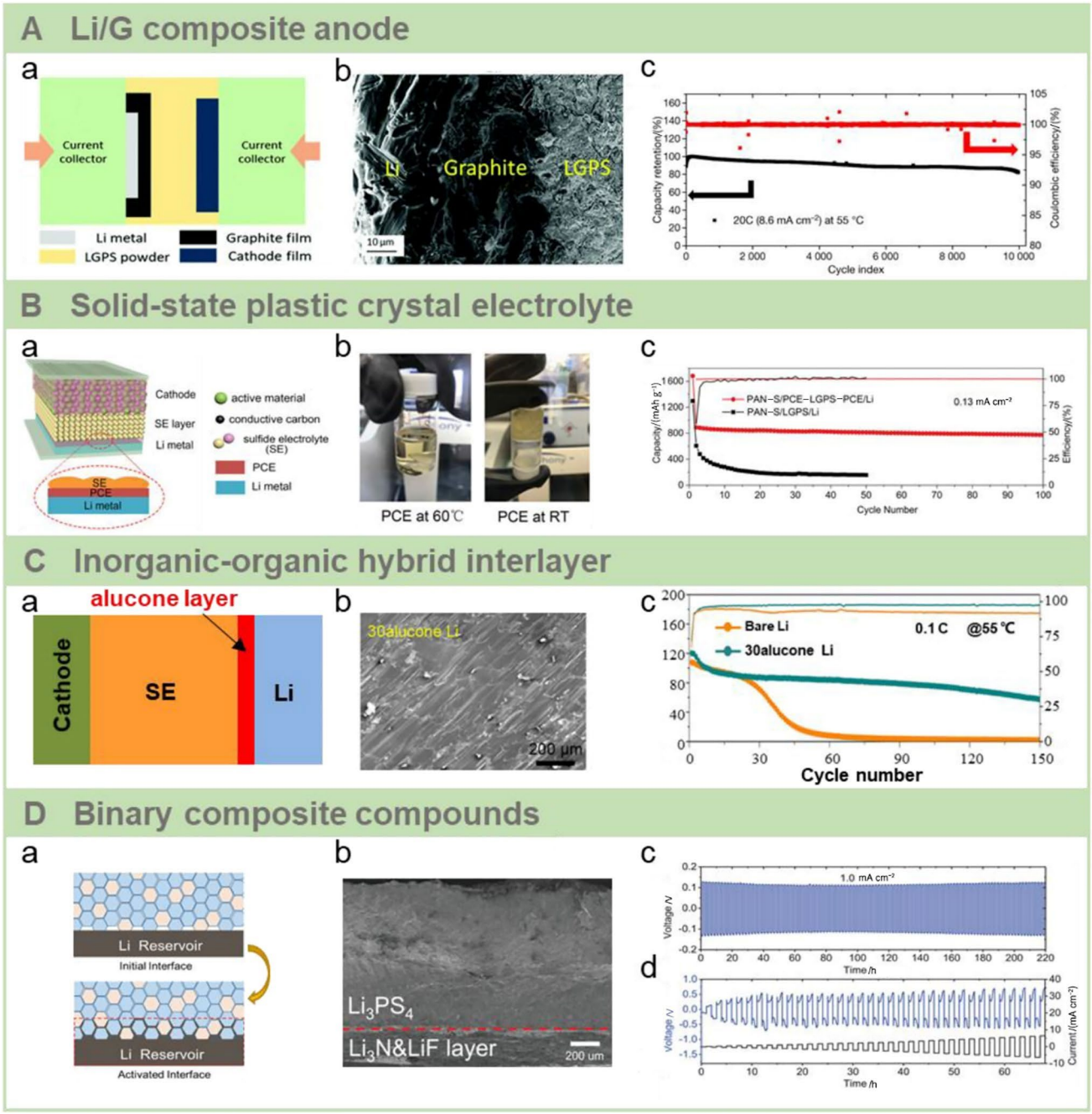

Fig. 7 Insertion of a stable ex situ buffer interlayer between Li and SEs. **A a** The illustration of Li/G structure design. **b** Scanning electron microscopy of the cross-section for Li/G electrodes. Reprinted with permission from Ref. [110]. Copyright © 2020, Royal Society of Chemistry. **c** Electrochemical performance of ASSLBs for 10 000 cycles with Li/G electrodes at a high rate of 20 C. Reprinted with permission from Ref. [111]. Copyright © 2021, Springer Nature. B: **a** Schematic illustration of ASSLBs with the PCE interlayer. **b** Photographs of the PCE at different temperature. **c** Cycling performance of ASSLBs with and without the PCE interlayer at 0.13 mA cm^{-2} for 100 cycles. Reprinted with permission from Ref. [115]. Copyright © 2019, John Wiley and Sons. **C a** Schematic illustration of the alucone layer on the Li surface through MLD. **b** Scanning electron microscopy of the Li surface after MLD treatment. **c** Cycling performance of ASSLBs with and without the alucone layer at 55 °C. Reprinted with permission from Ref. [120]. Copyright © 2018, Elsevier. **D a** Schematic illustration of the interfacial activation process. **b** Scanning electron microscopy of structure of the Li_3N–LiF interlayer and Li_3PS_4 SEs. **c** Voltage profile for the symmetric cell at 1.0 mA cm^{-2} for 220 h. **d** Voltage profile of the symmetric cell at high current density of 6.0 mA cm^{-2}. Reprinted with permission from Ref. [121]. Copyright © 2020, John Wiley and Sons

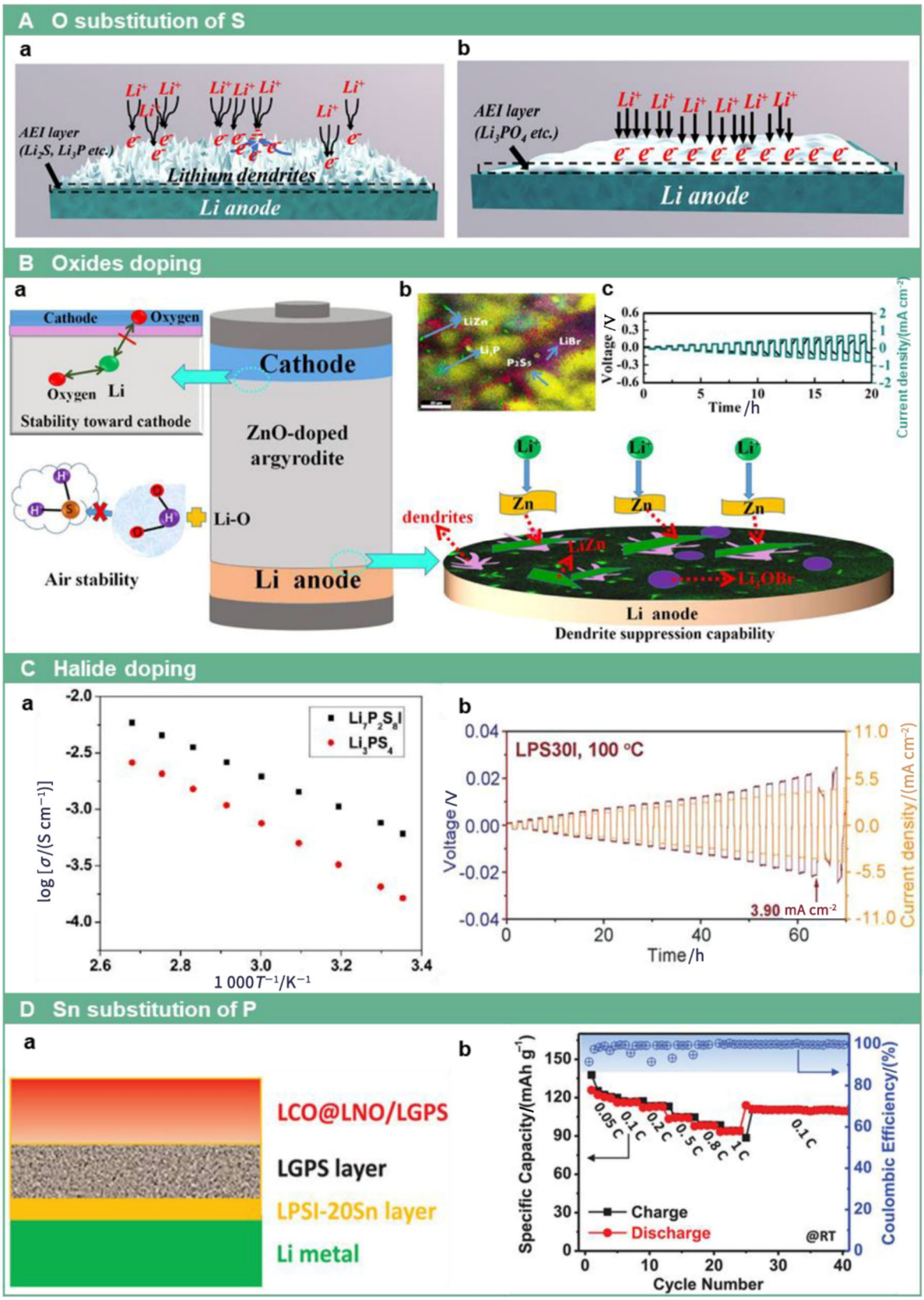
A O substitution of S
a
AEI layer
(Li2S, Li3P etc.)
Lithium dendrites
Li anode
b
AEI layer
(Li3PO4 etc.)
Li anode
B Oxides doping
a
Cathode
Oxygen
Oxygen Li
Stability toward cathode
Cathode
ZnO-doped
argyrodite
Li-O
Air stability
Li anode
b
LiZn
Li3P
P2S5
LiBr
c
Voltage /V
Time /h
Current density/(mA cm-2)
dendrites
Zn
LiZn
Li3OBr
Li anode
Dendrite suppression capability
C Halide doping
a
Li7P2S8I
Li3PS4
log [σ/(S cm−1)]
1 000T−1/K−1
b
LPS30I, 100 °C
Voltage /V
Time /h
3.90 mA cm-2
Current density/(mA cm-2)
D Sn substitution of P
a
LCO@LNO/LGPS
LGPS layer
LPSI-20Sn layer
Li metal
b
Specific Capacity/(mAh g-1)
Coulombic Efficiency/(%)
0.05 C
0.1 C
0.2 C
0.5 C
0.8 C
1 C
0.1 C
Charge
Discharge
@RT
Cycle Number

◂**Fig. 8** Substitution or doping for sulfide SEs. **A** O substitution of S for sulfide SEs. **a** Process diagram of dendrites growth without O doping for the Li–LPSC interface. **b** Schematic illustration of inhibition for Li dendrite with a stable interface. Reprinted with permission from Ref. [103]. Copyright © 2022, John Wiley and Sons. **B** ZnO co-doping in argyrodite. **a** Schematic illustration of advantages of ZnO-doped argyrodite sulfide SEs. **b** Elemental mapping on the Li–$Li_{5.7}Zn_{0.15}PS_{5.85}O_{0.15}Br$ interface. **c** Galvanostatic intermittent cycling of Li|$Li_{5.7}Zn_{0.15}PS_{5.85}O_{0.15}Br$|Li symmetric cells at RT for 20 h. Reprinted with permission from Ref. [127]. Copyright © 2019, ACS Publications. **C** Halide doping in sulfide SEs. **a** Arrhenius plot of these two sulfide SEs of Li_3PS_4 and $Li_7P_2S_8I$. Reprinted with permission from Ref. [135]. Copyright © 2015, ACS Publications. **b** Cycling performance of Li|LPS30I|Li cells at 100 °C [136] Copyright © 2018, John Wiley and Sons. **D** Sn substitution of P in argyrodite sulfide LPSI SEs. **a** Schematic illustration of Li|LPSI–20Sn/LGPS|LCO@LNO/LGPS ASSLBs. **b** Rate performance of Li|LPSI–20Sn/LGPS|LCO@LNO/LGPS ASSLBs at RT. Reprinted with permission from Ref. [137]. Copyright © 2020, John Wiley and Sons

a Li_7PS_8I interphase, exhibiting remarkable electrochemical stability reaching up to 10 V vs. Li/Li^+ [135]. This innovative interphase not only demonstrates significantly higher Li^+ conductivity (6.3×10^{-1} mS cm^{-1}) compared to β-Li_3PS_4 and LiI but also bolsters stability against Li metal while reducing charge transfer resistance. Wang et al. showcased the effectiveness of LiI incorporation into Li_2S–P_2S_5 glass electrolytes in suppressing Li dendrite formation, facilitating favorable Li deposition at the anode interface, and enabling a CCD of up to 3.9 mA cm^{-2} at 100 °C, as illustrated in Fig. 8C [136]. An alternative strategy involves substituting Sn for P in sulfide SEs, yielding stable SEs not only against Li anodes but also in moist air, thanks to the robust Sn–S bonding and high ionic conductivity of Sn-doped SEs [137, 138]. As depicted in Fig. 8D, the LPSI–20Sn electrolyte displayed exceptional plating/stripping behavior over 200 h in symmetric cells, serving as a stabilizing interlayer for Li anodes and exhibiting excellent performance and rate capability [137].

3.2.2 Design of Electrolyte structures

Vertical multilayered sulfide SEs represent a promising strategy, leveraging the best of single SE layers to enhance compatibility and stability at the SE–electrode interface. Li's group introduced a novel sandwiched electrolyte structure (Fig. 9A) to achieve exceptional rate capability and cycling performance [111]. This design concept, likened to an expansion screw effect, employs the newly formed Li dendrites as screws, the inner sulfide SEs like LGPS as anchors, and the surrounding SEs such as LPSC as drywalls. Similarly, a similar structural design involving Cl substitution in argyrodite SEs not only widens the ESW but also suppresses Li dendrite nucleation [112]. Addressing the challenge of poor interfacial stability between superionic conductor LGPS and Li anodes, bi-layer structural designs like LGPS/75%Li_2S–24%P_2S_5–1%P_2O_5 and LGPS/Li_3PS_4 have been developed [139, 140]. Additionally, for improved anode stability, Sb_2O_5 is incorporated into Li_3PS_4 to create a bi-layer structure of LGPS/$Li_3P_{0.98}Sb_{0.02}S_{3.95}O_{0.05}$. This combination of LGPS with high ionic conductivity and $Li_3P_{0.98}Sb_{0.02}S_{3.95}O_{0.05}$ boasting exceptional stability enhances Li^+ flux even at − 10 °C while improving anode interfacial compatibility [131]. However, solely protecting the Li anode doesn't entirely prevent side reactions and Li dendrites. Ci's group devised a robust layer coating on SEs, such as graphene oxide (GO) and Li_2S, to mitigate interfacial reactions between Li and $Li_7P_3S_{11}$ particles, as well as to guide or induce homogeneous Li deposition (Fig. 9B) [141, 142]. In the Li_2S@$Li_7P_3S_{11}$ system, the resulting ASSLB exhibited exceptional cycling performance over 150 cycles, serving as an effective means to inhibit Li dendrite formation.

In the realm of sulfide SEs-based ASSLBs systems, the strategies mentioned earlier—SEI fabrication and SEs modification—have shown significant promise in improving anode interfacial stability and restraining Li dendrite growth to varying degrees. However, the fundamental issue persists. Completely eliminating the possibility of Li dendrite formation demands a design that facilitates the uniform deposition and growth of Li. In an innovative approach illustrated in Fig. 9C, Wang et al. explored a strategy involving a wood template LPSC to manipulate a consistent Li^+ flux. Electrolyte cells assembled with such modified systems exhibited exceptional stability for 1 000 h at 0.2 mA cm^{-2} (in symmetric cells) and maintained excellent battery performance over 100 cycles ($Li_4Ti_5O_{12}$|LPSC@wood|Li cells) [143]. Another intriguing approach was introduced by Liang et al., who engineered an adhesive sulfide SEs by employing hot melting adhesive porous membranes made of ethyl vinyl acetate porous (EVAP) on LGPS. The adhesive force played a pivotal role in enhancing the contact area at the anode interface and improving interfacial stability, offering a fresh perspective on interfacial engineering in ASSLB applications [144].

3.3 Alloying of Li Anode

Li alloys present an enticing alternative to pure Li anodes in ASSLBs, offering enhanced solid–solid contact wettability, promoting uniform Li deposition, and curbing Li dendrite formation during plating/stripping. Several high-capacity Li alloys—like Li–In, Li–Si, Li–Al, and Li–Sn alloys—serve as effective Li dendrite inhibitors, elevating charge–discharge reversibility and long-term cyclability for ASSLBs [145]. Moreover, these alloys offer superior mechanical properties compared to pure Li metal [145]. The newly formed alloyed interphase during cycling also holds promise for enabling high capacity and stable long-term performance

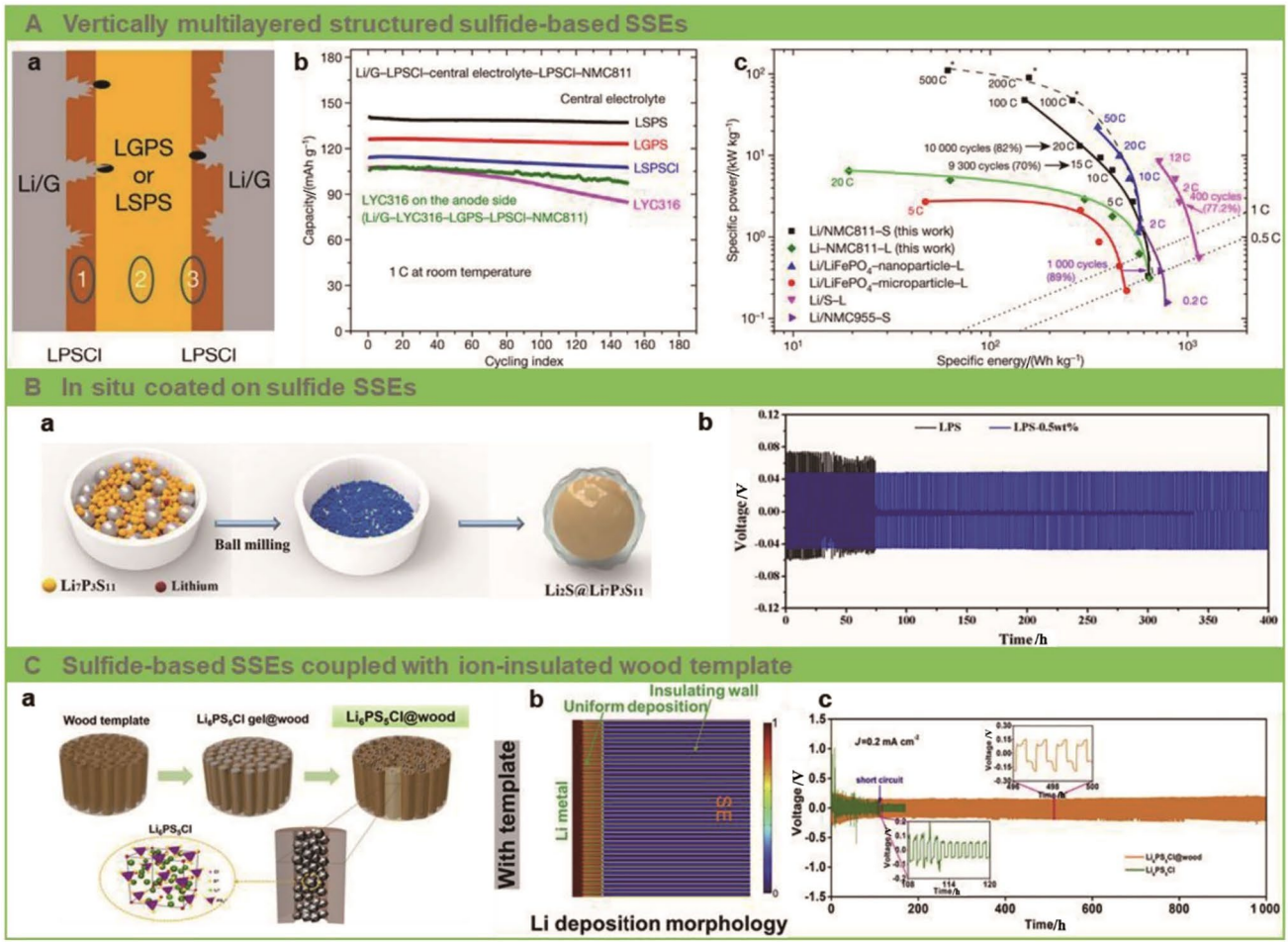

Fig. 9 Structural design for sulfide SEs. **A** Vertically multilayered structured sulfide SEs. **a** Schematic illustration of Li/G|LPSC–LGPS–LPSC|G/Li. **b** Cycling performance of sandwiched structural sulfide SEs at a rate of 1 C with different central electrolytes at RT coupled with Li/G anodes and NCM811. **c** The Ragone plot for typical ASSLBs' performance. Reprinted with permission from Ref. [111]. Copyright © 2021, Springer Nature. **B** In situ coated on sulfide SEs. **a** Schematic illustration of synthesis procedures of $Li_2S@Li_7P_3S_{11}$ composite sulfide SEs. **b** The voltage profiles of Li/Li symmetric batteries with and without Li_2S coating for $Li_7P_3S_{11}$ SEs at 0.1 mA cm^{-2}. The expression "wt%" means "% by weight". **c** Bulk transition energy barrier for Li_2S and $Li_7P_3S_{11}$. Reprinted with permission from Ref. [142]. Copyright © 2022, Elsevier. **C** Ion-insulation wood template coupled with LPSC structural design. **a** Schematic illustration of synthesis procedures of LPSC@wood SEs. **b** Li deposition morphology and distribution within LPSC@wood SEs. **c** Electrochemical performance of symmetric cells for LPSC (green) and LPSC@wood (orange) SEs at 0.2 mA cm^{-2}. Reprinted with permission from Ref. [143]. Copyright © 2020, Elsevier

in ASSLBs. Among these alloys, Li–In alloys (with a capacity of 220 mAh g^{-1} for LiIn) are frequently used in lab-scale experiments due to their thermodynamic and kinetic stability [146–148]. The Li–In alloy exhibits higher Li^+ diffusivity compared to Li metal owing to lower energy barriers for bulk Li diffusion. However, the high voltage difference of ≈ 0.6 V between In and Li leads to a significantly reduced discharging platform, resulting in decreased energy density in ASSLBs. Despite this, most ASSLBs using Li–In anodes only cycle at low current density, insufficient to effectively demonstrate Li–In alloy's ability to suppress dendrite formation. Zhang et al. reported the short-circuiting of a Li–In|LPSC|NCM622 full cell due to Li–In dendrite generation after long-term cycling at high current density and cathode loading (Fig. 10A) [149]. Analysis via scanning electron microscope (SEM), X-ray photoelectron spectroscopy (XPS), and Ab initio molecular dynamics (AIMD) indicated that metallic In lacks absolute thermodynamic and kinetic stability with sulfide SEs, causing volume expansion and interfacial reactions, leading to Li–In dendrite formation and penetration under high current density until cell failure. Unlike vertically grown Li dendrites, the laterally striped morphology of Li–In dendrites exhibits reduced growth rates, minimizing electrolyte structure damage—an important guideline for alloy anode research and development [150]. Li–In alloys can also be obtained from Li-free In

foil anodes during Li plating, showcasing improved interfacial contact due to volume expansion without dendrites and exhibiting excellent cycling stability for over 160 cycles. Beyond mechanical and physical mixing methods, Li–In alloy incorporation on sulfide SEs stabilizes the anode surface. Lee et al. devised a unique In–I–Li–P–S layer inserted between the Li anode and the Li_3PS_4 electrolyte. Composed of Li_2S, P_2S_5, and InI_3, this layer forms a Li–In alloy and a stable LiI interphase with chemical stability toward the Li anode [151]. This In–I–Li–P–S protector effectively separates the Li anode and the Li_3PS_4 electrolyte without causing side reactions, exhibiting outstanding electrochemical performance (cycling over 500 h) in assembled ASSLBs.

Li–Si alloys, offering a voltage plateau of < 0.3 V vs. Li/Li^+, boast high theoretical specific capacities of 3 572 mAh g^{-1} ($Li_{15}Si_4$). Earlier studies using $Li_{4.4}Si$ and $Li_{4.4}Ge_xSi_{1-x}$ as anodes for sulfide-based cells yielded unsatisfactory results [152, 153]. However, recent research utilizing pure Si anodes in sulfide-based cells has shown exceptional performance. Stefan Kaskel et al. investigated a columnar Si anode employing a 1D breathing mechanism via a scalable physical vapor deposition (PVD) process [154]. This 1D Si anode design maintains the interface, reduces the active contact area, and minimizes side reactions during cycling. The assembled Si|LPSC|NCM full cell demonstrated an outstanding area capacity of 3.5 mAh cm^{-2} and stable cycling performance with an excellent Coulombic efficiency (CE) of 99.7% – 99.9% over 100 cycles. In cyclic voltammetry (CV) measurements of cathodic scans for Si|SE|Li half cells, Si exhibited three phase transformations: a-Si to PI phases (Li–50% by atom number (hereinafter the expression "% by atom number" is referred to as "at%") Si; LiSi), the PI phase to the PII phase (Li–30 at% Si; Li_7Si_3) at 0.21 V vs. Li/Li^+, and the PII phase to the PIII phase (Li–24 at% Si; $Li_{3.16}Si$) at 0.05 V vs. Li/Li^+. The discharge voltage is influenced by the Si anode's voltage plateau, which extends to 1.0 V instead of providing a constant voltage plateau (as seen in Li or In anodes). Consequently, the cut-off voltage for Si anode-based ASSLBs is reduced to 2.0 V for complete anode utilization. Meng et al. reported a 99.9% by weight (hereinafter the expression "% by weight" is referred to as "wt%") μSi anode used in μSi|LPSC|NCM811 full cells, achieving remarkable interfacial stability and cycling performance (Fig. 10B) [155]. This μSi anode, devoid of carbon additives, prevents sulfide SE decomposition while forming a Li–Si interphase between Si and sulfide SEs, facilitating both electronic and ionic transport. Operating at wide temperatures ranging from – 20 to 80 °C, the critical current density (CCD) reaches 5 mA cm^{-2}, and for the first time, the area capacity reaches up to 11 mAh cm^{-2}, retaining an outstanding capacity of 80% over long-term cycling. This provides compelling evidence for the viability of Si anodes in ASSLBs. Zhu et al. investigated ASSLBs using nano-Si anodes, achieving an excellent capacity of 145 mAh g^{-1} over 1 000 cycles [156]. Unlike Meng's research [155], carbon additives in nano-Si did not result in sulfide SE decomposition, possibly due to the lower electronic conductivity of nano-Si, three orders of magnitude lower than μSi, attributed to its larger surface area and SiO coating. Furthermore, in the same system, Zhu's group designed bipolar stacking ASSLBs with a high voltage of 8.2 V and an energy density of 204 Wh kg^{-1} [157]The ionic conductivities o The advancements in Si anode research are poised to drive large-scale commercialization and progression in ASSLBs.

Kim et al. introduced the Ag–Li anode to establish a stable interface between the anode and LPSC by forming an in situ intermetallic layer composed of Ag–Li [158]. Their assembled Ag–Li|LPSC|NCM full cell exhibited superior cycling performance even under a high rate of 12 C. Utilizing a thin Ag–C nanocomposite layer as the anode effectively regulated Li deposition and improved stable cycling performance [159]. The solubility of Ag in Li forms a stable Li–Ag alloy that maintains an interface, while carbon acts as a separator, preventing SEs from direct contact with the Li anode. This assembled pouch cell demonstrated an outstanding energy density of > 900 Wh L^{-1} and a CE of > 99.8% over 1 000 cycles. Building on the insights gained from the Ag–C layer [159], Yang et al. employed a clever design by incorporating a Li-based Li–B alloy within a 3D skeleton and an Ag@C layer. The Li–B alloy countered the volume changes in the anode during cycling, while the Ag@C layer maintained a stable interphase [160]. Choi chose an Ag–C composite anode with an elastic spandex binder, resulting in the formation of Ag–Li alloys at the anode interface [161]. Zhou et al. designed a reliable anode using a $Li_{0.8}Al$ alloy without carbon and binder additives for ASSLBs, as depicted in Fig. 10C [162]. The $Li_{0.8}Al$ alloy exhibited excellent performance toward LGPS, retaining an outstanding capacity of 93.29% for 200 cycles and an energy density of 541 Wh kg^{-1}. These various strategies employing Li alloying provide promising options for anodes and significantly expedite the practical implementation of ASSLBs.

4 Interfacial Engineering Toward Li and Oxide SEs

Numerous oxide SEs, such as Li phosphorus oxynitride (LiPON), despite being relatively inexpensive, exhibit undesirable ionic conduction of 2×10^{-3} mS cm^{-1}, making them unsuitable for practical applications—an aspect extensively covered in previous reviews and thus won't be discussed here [163]. Instead, the focus lies on the most promising oxide SEs, particularly garnets and NASICONs. In the case of garnets, while the interface stability between oxide SEs and the Li anode is commendable, garnets possess

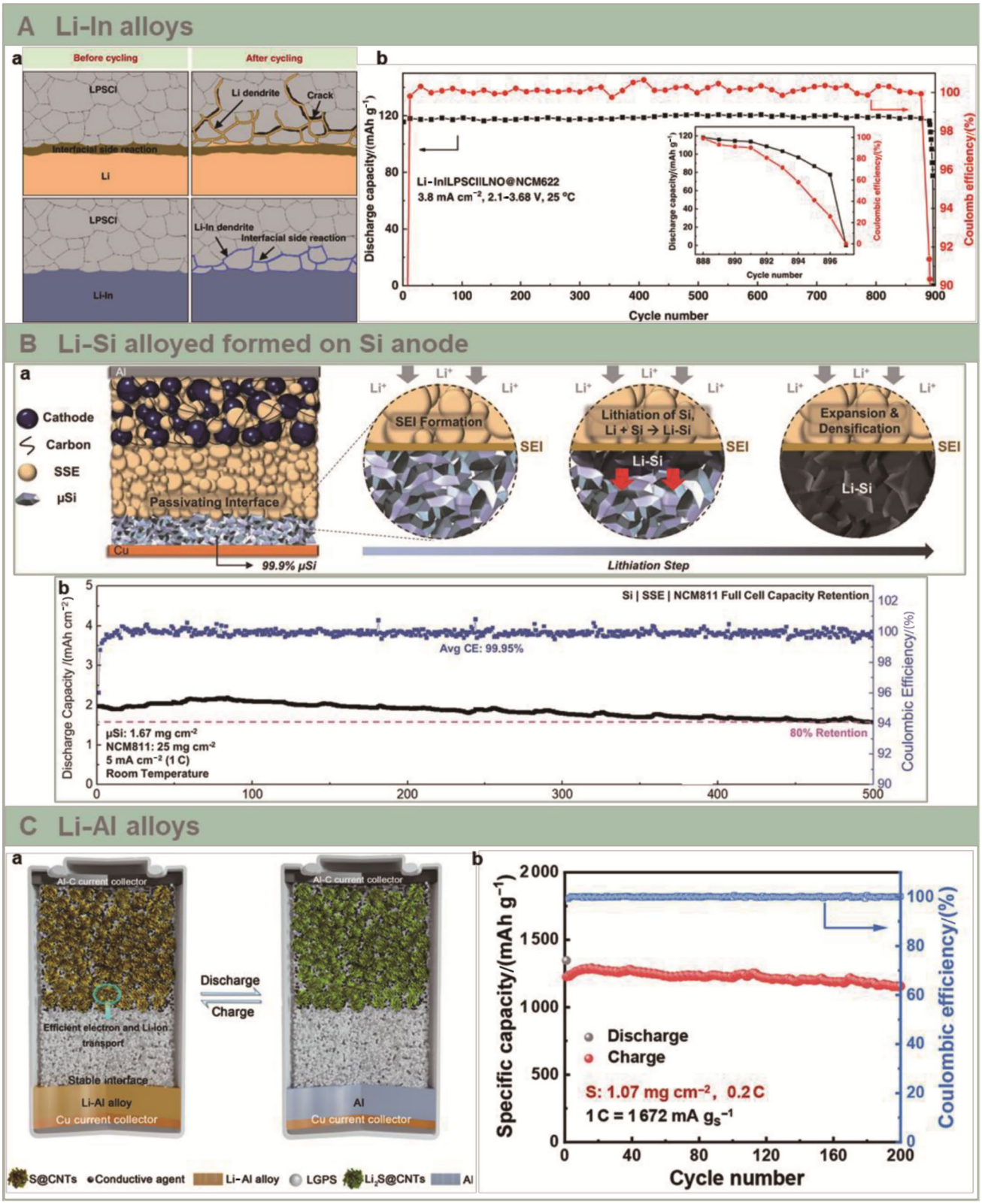
A Li-In alloys
a
Before cycling
After cycling
LPSCl
Interfacial side reaction
Li
Li dendrite
Crack
LPSCl
Li-In
Li-In dendrite
Interfacial side reaction
b
Li-In|LPSCl|LNO@NCM622
3.8 mA cm⁻², 2.1–3.68 V, 25 °C
Discharge capacity/(mAh g⁻¹)
Coulomb efficiency/(%)
Cycle number
B Li-Si alloyed formed on Si anode
a
Cathode
Carbon
SSE
μSi
Al
Passivating Interface
Cu
99.9% μSi
SEI Formation
Lithiation of Si, Li + Si → Li-Si
Expansion & Densification
SEI
Li-Si
Lithiation Step
b
Si | SSE | NCM811 Full Cell Capacity Retention
Avg CE: 99.95%
80% Retention
μSi: 1.67 mg cm⁻²
NCM811: 25 mg cm⁻²
5 mA cm⁻² (1 C)
Room Temperature
Discharge Capacity /(mAh cm⁻²)
Coulombic Efficiency/(%)
C Li-Al alloys
a
Al-C current collector
Efficient electron and Li-ion transport
Stable interface
Li-Al alloy
Cu current collector
Discharge
Charge
Al
S@CNTs
Conductive agent
Li-Al alloy
LGPS
Li₂S@CNTs
Al
b
Discharge
Charge
S: 1.07 mg cm⁻², 0.2 C
1 C = 1 672 mA gs⁻¹
Specific capacity/(mAh g⁻¹)
Coulombic efficiency/(%)
Cycle number

◂**Fig. 10** Alloyed for Li anodes to improve interfacial properties with sulfide SEs. **A** Li–In alloy anode used in LPSC. **a** Schematic diagram of anode interface evolution with the Li anode and the Li–In anode for LPSC before and after cycling. **b** Long-term cycling performance of Li–In|LPSC |LNO@NCM622 at 3.8 mA cm^{-2}. Reprinted with permission from Ref. [149]. Copyright © 2021, Springer Nature. B: Pure silicon anode enabled by sulfide SEs. **a** Schematic illustration of interfacial change during lithiation processes between the Si anode and LPSC. **b** Si|LPSC|NCM811 cycling performance at RT. Reprinted with permission from Ref. [155]. Copyright © 2021, Science. **C** Carbon-free and binder-free Li–Al alloys used in LGPS. **a** Schematic illustration of charging and discharging of Li–Al alloy in ASSLBs. **b** Cycling stability of ASSLBs using $Li_{0.8}Al$ alloy anodes for 200 cycles at 0.2 C. Reprinted with permission from Ref. [162]. Copyright © 2022, Science family of journals/AAAS

a lithiophobic nature that hampers their contact with the Li anode, leading to undesirable interfacial resistance reaching several or even hundreds of kΩ cm^2. Additionally, this lithiophobic characteristic restricts effective wettability at the anode interface, resulting in uneven current distribution and the formation of Li dendrites, which significantly hinders the practical application of garnets. On the other hand, NASICONs demonstrate high Li^+ conductivity and exceptional air stability. However, their development faces hurdles due to interfacial challenges, including high interfacial impedance and severe side reactions with Li metal, impeding their progress in practical applications. Researchers have explored various approaches to address these issues in oxide SEs, encompassing electrolyte modification, the creation of artificial solid-state electrolyte interfaces, and composite Li anodes. In the subsequent sections, we will consolidate the recent strides made in advancing strategies to enhance the interfaces of oxide SEs-based ASSLBs.

4.1 Insertion of Interlayer

Introducing an ideal SEI stands as a potent strategy to resolve the interfacial challenges encountered between the Li anode and oxide SEs. This approach not only enhances the wettability of Li on oxide SEs but also reduces interfacial impedance significantly. This section will focus on summarizing the SEI interlayer insertion strategy for two primary types of oxide SEs—garnets and NASICONs.

4.1.1 Interlayer for Li–Garnets

The interfacial resistance between garnets and the Li anode is heavily influenced by the presence of impurities like Li_2CO_3 and LiOH. Addressing these issues involves introducing an artificial SEI to reduce interfacial impedance, enhance wettability, and improve the lithiophilic affinity between the Li anode and garnets. Additionally, the insertion of an SEI interlayer proves beneficial in curbing cracks and defects within oxide SEs. To meet the necessary criteria for an effective artificial SEI, several key requirements must be fulfilled: (1) stability with garnets; (2) high Li^+ diffusivity; (3) minimal volume change during cycling; (4) minimal thickness to not compromise the energy density of ASSLBs. Various types of SEI interlayers exist, including liquid metals, metal oxides, conductive binary compounds, Li alloys, electrically conductive materials, covalent organic frameworks (COFs), polymers, and others. Liquid metals can infiltrate garnet grain boundaries to create additional ionic transport paths. Li's group proposed using liquid Ga as a lithiophilic layer on garnets, avoiding the need to remove Li_2CO_3. This method significantly reduces Li–garnet interfacial resistance, ensuring high battery reversibility [164]. Oxide interlayers enhance the wettability of oxide SEs for Li metal. For instance, an ultrathin Al_2O_3 film deposited on $Li_7La_{2.75}Ca_{0.25}Zr_{1.75}Nb_{0.25}O_{12}$ using the ALD method has shown promising results. This lithiated Al_2O_3 interface drastically reduces interfacial impedance and improves wettability, albeit with some complexity and cost limitations in the ALD method (Fig. 11A) [88]. Another approach involves coating a Ta_2O_5 nanofilm on LLZTO, significantly decreasing interfacial impedance and resulting in high-performance full cells with impressive endurance [165].

The right interlayer can establish an alloy interphase, stabilizing the Li–garnet interface, reducing interfacial impedance, and enhancing garnet surface wettability. Zhang et al. introduced $In_{2(1-x)}Sn_{2x}O_3$ (ITO) as an interlayer, forming a Li_xIn/Li_xSn interphase that effectively bonds the Li anode onto the LLZTO surface through conversion and alloying reactions [166]. Guo et al. addressed LLZTO–Li anode interfacial issues by modifying LLZTO with a Sn film, reducing interfacial resistance by approximately 20 times through Li–Sn alloy formation (Fig. 11B) [167]. Liu et al. applied a SnS_2 film on LLZTO, significantly lowering interfacial impedance to ~ 17 Ω cm^2, enhancing wettability, and improving CCD for ASSLBs [168]. Hu et al. in situ coated a Si film on garnets, creating a super lithiophilic SE that displayed low impedance and excellent cycling stability [169]. Alloy formations like Li–Ag [170, 171], Li–Zn [172, 173] and Li–Al [174] alloys have also proven effective in adjusting garnet wettability. However, there's a continual need for more appropriate alloy interphases to meet evolving requirements.

Interphases consisting of conductive binary materials like Li_3N, Li_3P, Li_2O, and LiF offer strong capabilities in impeding Li penetration in garnets [175–177]. Guo et al. introduced a practical SEI insertion strategy involving inorganic and organic compounds (Fig. 11C) [177]. This SEI interlayer, fostering high Li^+ and electronic conductivities between LLZTO and the Li anode, enhances wettability without impeding charge transfer. Sun et al. implemented an MIEC interlayer with Li_3N/Cu nanoparticles at the anode–garnet interface via magnetic sputtering technology

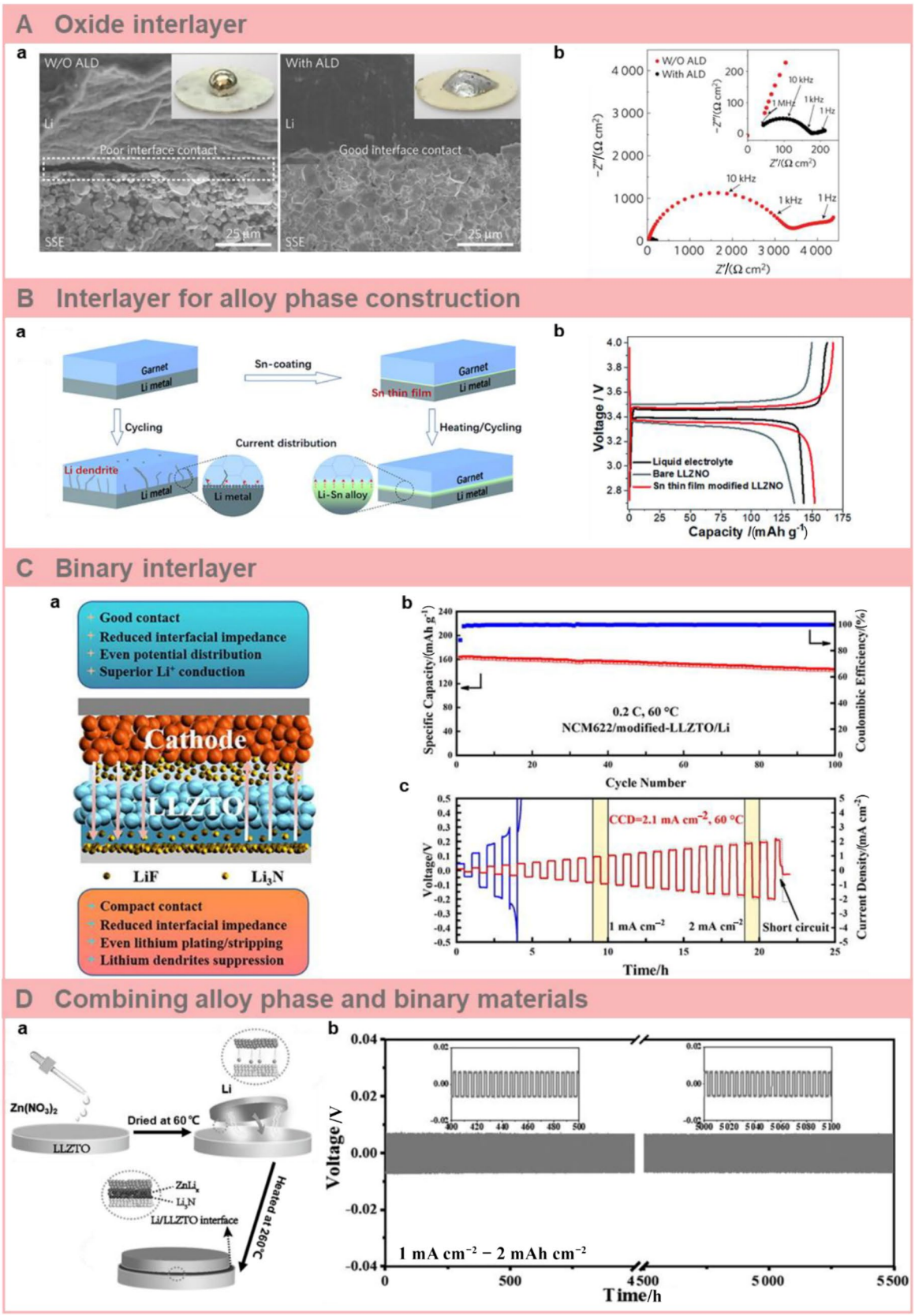
A Oxide interlayer
a
W/O ALD
With ALD
Li
Poor interface contact
Good interface contact
SSE
25 μm
b
W/O ALD
With ALD
10 kHz
1 kHz
1 Hz
1 MHz
Z'/(Ω cm²)
−Z''/(Ω cm²)
B Interlayer for alloy phase construction
a
Garnet
Li metal
Sn-coating
Sn thin film
Cycling
Heating/Cycling
Current distribution
Li dendrite
Li-Sn alloy
b
Voltage / V
Capacity /(mAh g⁻¹)
Liquid electrolyte
Bare LLZNO
Sn thin film modified LLZNO
C Binary interlayer
a
Good contact
Reduced interfacial impedance
Even potential distribution
Superior Li⁺ conduction
Cathode
LLZTO
LiF
Li₃N
Compact contact
Reduced interfacial impedance
Even lithium plating/stripping
Lithium dendrites suppression
b
Specific Capacity/(mAh g⁻¹)
Coulombic Efficiency/(%)
0.2 C, 60 °C
NCM622/modified-LLZTO/Li
Cycle Number
c
Voltage/V
Current Density/(mA cm⁻²)
CCD=2.1 mA cm⁻², 60 °C
1 mA cm⁻²
2 mA cm⁻²
Short circuit
Time/h
D Combining alloy phase and binary materials
a
Zn(NO₃)₂
LLZTO
Dried at 60 °C
Li
ZnLiₓ
Li₃N
Li/LLZTO interface
Heated at 260 °C
b
Voltage /V
1 mA cm⁻² − 2 mA cm⁻²
Time/h

◂**Fig. 11** For optimizing the interface between Li anodes and garnet SEs, a stable SEI interlayer insertion strategy is applied. **A** Al_2O_3 interlayer for improving interface between Li and $Li_7La_{2.75}Ca_{0.25}Zr_{1.75}Nb_{0.25}O_{12}$. **a** Scanning electron microscopy of the Li–garnet interface without and with Al_2O_3 interlayers. **b** Corresponding EIS's comparison results. Reprinted with permission from Ref. [88]. Copyright © 2017, Springer Nature. **B** Schematic illustration of the desired Li–garnet interface. **a** Schematic illustration of the Li–garnet interface with and without surface modification. **b** The first charge–discharge curve of Li|Sn–LLZNO|$LiFePO_4$ ASSLBs. Reprinted with permission from Ref. [167]. Copyright © 2018, The Royal Society of Chemistry. **C** Binary materials interlayer for improving the interface between garnet–type oxide SEs and electrodes. **a** Schematic diagram and advantages of the interfacial stability strategies of garnet–type oxide SE's ASSLBs toward electrodes. **b** Capacity and CE at 0.2 C under 60 °C for NCM622|modified–LLZTO|Li cells. **c** CCD test results of symmetric cells with and without garnet surface modification. Reprinted with permission from Ref. [177]. Copyright © 2021, Elsevier. **D** Combing alloy phases and binary materials as the interlayer for garnet–type oxide SEs. **a** Diagram of preparation processes of the Li–LLZTO interface through chemical reaction between $Zn(NO_3)_2$ and Li. **b** Long-term cycling tests results with improved interfaces at 1 − 2 mA cm^{-2} for Li symmetric cells. Reprinted with permission from Ref. [183]. Copyright © 2020, John Wiley and Sons

[89]. This interlayer aids Li^+ transport, regulates electric field distribution, suppresses Li dendrite generation, and optimizes anode interface contact. A chemical reaction between Li and SnF_2 forms an in-situ mosaic structural Li_7Sn_3/LiF interphase at the Li–garnet interface [178]. Li_7Sn_3 acts as an ionic conductor, relieving mechanical stress during cycling, while LiF expedites Li^+ transport through Li_7Sn_3.

Combining alloy phase construction with conductive binary materials, a mixed conductive layer showcasing robust electronic and ionic conductivity effectively diminishes interfacial impedance, improves Li–garnet anode physical contact, and suppresses Li dendrite formation. An introduced Si_3N_4 layer on garnets forms a stable interphase of Li–Si alloy and Li_3N through a reduction reaction with Li metal, ensuring tight Li anode contact, homogeneous electric field distribution, and a significant drop in interfacial resistance [179, 180]. A garnet-based ASSLB incorporating a Li_2S/Li_xSn interphase exhibited an interfacial impedance of 47 Ω cm^2 and sustained a long-term cycling life over 1 000 h [181]. A homogenous lithiophilic interphase comprising $InLi_x$ and LiCl was crafted between the Li anode and LLZTO by using a straightforward, cost-effective wet chemistry method [182]. This approach showcased a reduction in interface impedance from 189 to 1 Ω, an increase in CCD from 0.2 to 0.7 mA cm^{-2}, and exceptional electrochemical performance over 475 cycles. Wang et al. proposed an in situ method to generate a $ZnLi_x$ and Li_3N interlayer between Li and LLZTO via an energetic chemical reaction between $Zn(NO_3)_2$ and Li [183]. This approach demonstrated a CE of > 99.5% without Li dendrite generation over thousands of hours of cycling, as depicted in Fig. 11D.

The cycling-induced localized stress often triggers the formation of Li dendrites. Carbon materials, known for their high ionic and electronic conductivity, serve as excellent soft buffer layers, ensuring electro-chemo-mechanical stability. Li et al. devised a lithiophilic candle soot (CS) shield atop LLZTO using flame vapor deposition, which displayed a polycrystalline structure with graphitic domains (Fig. 12a, b) that mitigated the carbonate layer [184]. The Li|CS-LLZTO|FeF_3 cell exhibited an exceptional capacity of 500 mAh g^{-1} over 1 500 cycles, showcasing remarkable long-term cyclability. Similarly, a graphite-based soft interface was created as a buffer layer via pencil drawing, demonstrating outstanding ionic and electronic conductivities (Fig. 12c, e). This straightforward method ensures uniform Li^+ distribution, resulting in ASSLBs with superior rate capacity and long-term cyclability [185]. Hu et al. utilized amorphous carbon between Li and garnets to uphold electronic conductivity and regulate Li^+ flux, addressing electro-chemo-mechanical stability concerns (Fig. 12f, g) [186]. Li et al. introduced a novel strategy involving the one-step fabrication of LLZTO with a lithiophilic graphite (iGr@LLZTO) interface. This approach reduced resistance from 4 351.6 to 26.2 Ω cm^2, decreased overpotential from 500 to 30 mV, and improved contact between iGr@LLZTO and the Li anode while ensuring compatibility and efficient Li^+ transport [187].

To maintain electro-chemo-mechanical stability, a stress-adaptive interlayer proves effective. Luo et al. demonstrated a soft hyperelastic polydimethylsiloxane (PDMS) substrate (Fig. 13A) that effectively suppressed Li dendrite formation and cracks in garnets during cycling [188]. In garnet-based ASSLBs, the rigid contact between oxide SEs and Li demands a softer polymer interlayer to reduce anode interfacial impedance and enhance contact with the Li anode. An in situ solidified gel polymer electrolyte (GPE) buffered the interface between the electrode and garnets, fortifying the garnet blocks and enabling flexible solid batteries [189]. Additionally, Fan et al. devised a polymer SE and 3D Li metal structure specifically for suppressing Li dendrites using 3D frameworks [190]. COFs, with their regular open channels, facilitate improved wetting of garnets by the Li anode and swift Li^+ conduction. COF-based layers serve as interlayers to enhance garnet lithiophilicity and diminish interfacial impedance. For instance, sulfonated COFs were prepared to boost the lithiophilicity of LLZTO against the Li anode and establish a pathway for Li^+ diffusion at the anode interface (Fig. 13B) [191]. The resulting symmetric solid-state Li cells demonstrated lower interfacial impedance and a high CCD of 3 mA cm^{-2}.

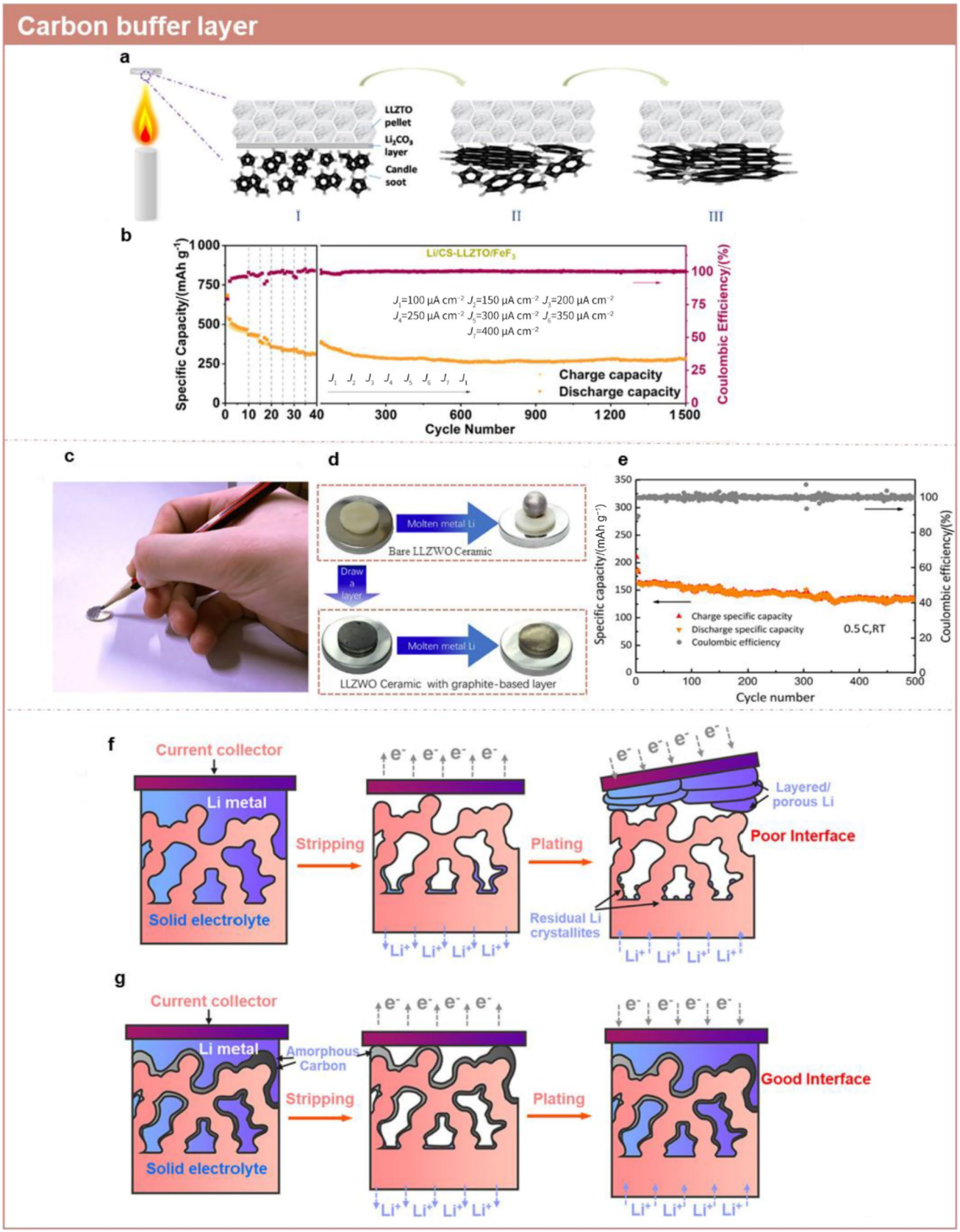
Carbon buffer layer
a
LLZTO pellet
Li2CO3 layer
Candle soot
I
II
III
b
Li/CS-LLZTO/FeF3
Specific Capacity/(mAh g-1)
Coulombic Efficiency/(%)
Cycle Number
Charge capacity
Discharge capacity
c
d
Molten metal Li
Bare LLZWO Ceramic
Draw a layer
LLZWO Ceramic with graphite-based layer
e
Specific capacity/(mAh g-1)
Coulombic efficiency/(%)
Cycle number
Charge specific capacity
Discharge specific capacity
Coulombic efficiency
0.5 C,RT
f
Current collector
Li metal
Solid electrolyte
Stripping
Plating
Layered/ porous Li
Poor Interface
Residual Li crystallites
g
Current collector
Li metal
Amorphous Carbon
Solid electrolyte
Stripping
Plating
Good Interface

◂**Fig. 12** Insertion of the carbon buffer layer between Li anodes and garnet-type SEs. **a** Illustration of CS preparation processes. **b** Cycling tests results of the Li|CS–LLZTO|FeF_3 ASSLBs under different current densities from 100 to 400 μA cm^{-2}. Reprinted with permission from Ref. [184]. Copyright © 2020, ACS Publications. **c** Schematic illustration of preparation processes for graphite-based interlayers through pencil drawing. **d** Comparison of wettability for molten Li metal on $Li_{5.9}Al_{0.2}La_3Zr_{1.75}W_{0.25}O_{12}$ (LLZWO) with and without interlayers. **e** Cycling performance of ASSLBs at 0.5 C. Reprinted with permission from Ref. [185]. Copyright © 2018, ACS Publications. **f** and **g** Schematics illustration of Li^+ transport behaviors without and with carbon interlayers during plating/stripping process. Reprinted with permission from Ref. [186]. Copyright © 2021, ACS Publications

4.1.2 Interlayer for Li–NASICONs

The reduction of NASICONs by Li metal can be controlled by incorporating an SEI interlayer. In the case of LATP, various artificial buffer interlayers have been explored to tackle interfacial issues, spanning from inorganic to organic solutions. For instance, the use of ultrathin ZnO helped create a multifunctional SEI with low electronic conductivity on LATP [192]. Similarly, like LLZTO, an Al_2O_3 protective interlayer applied via ALD technology can safeguard the Li–LATP interface [193]. Employing organic LEs on the Li anode allows the formation of an artificial SEI at the Li–LATP interface. A stable interphase containing LiF, MgF_2, and B_2O_3 was achieved by using a DME solution containing $LiBF_4$ and $Mg(ClO_4)_2$, showcasing excellent capacity retention (84.6%) over 500 cycles [194, 195]. Polymer SEs, known for their viscoelastic and flexible properties, particularly PEO-based polymers, have been utilized, although PEO's efficiency tends to decrease below 60 °C [196–198]. Additionally, a biomaterial-derived interlayer made of a conformal sericin protein film (SPF) has emerged as a novel prospect for NASICONs-based ASSLBs, effectively preventing LATP reduction and Li dendrite formation (Fig. 14A) [199].

Various interlayers have been employed to enhance surface stability and reduce impedance for LAGP. Strategies like the implementation of a LiF-Li_3N layer as an SEI or using a metallic Bi thin film have been proposed to boost compatibility and inhibit side reactions at the Li–LAGP interface [200, 201]. Additionally, the application of LiPON thin films as separators on B_2O_3-added LAGP, generated via RF-sputtering technology, has shown promise in mitigating side reactions [202]. Efforts have also focused on creating PEO-based buffer interlayers to stabilize the anode interface for LAGP. For instance, a poly(vinylene carbonate) (PVCA)-based buffer interlayer successfully improved interfacial compatibility, achieving a full cell with exceptional cycling performance, retaining 96% capacity over 200 cycles [203]. Similarly to garnets, the GPE employing an 8.85 μm thickness PMMA as an SEI exhibited efficient suppression of side reactions and Li dendrite formation, showcasing good cycling stability for 200 cycles at 25 °C (Fig. 14B) [204].

4.2 Optimization of Oxide SEs

The diversity in ionic conductivities and chemical properties across various types of oxide SEs results in distinct advantages and disadvantages. For example, garnets demonstrate acceptable high ionic conduction properties ranging from 0.1 to 1 mS cm^{-1}. They exhibit relatively high stability but are plagued by issues such as large impedance and limited wettability toward the Li anode. On the other hand, NASICONs showcase remarkable ionic conduction properties within the range of 1 to 10 mS cm^{-1}. However, they also suffer from significant side reactions and poor contact with Li. Consequently, modifications in various approaches are essential for optimizing oxide SEs to achieve ASSLBs with high capacity and stable long-term cycling performance.

4.2.1 Conditioning of Electrolyte Surface

The primary challenge with garnets lies in their inadequate physical contact, leading to substantial interfacial impedance. Moreover, garnets exhibit a propensity to spontaneously exchange Li^+ and H^+, making them susceptible to water and air, resulting in impurities like LiOH and Li_2CO_3 on their surface. These impurities hinder effective contact with Li metal and diminish ionic conductivity, posing significant barriers to the commercial use of garnets. Surface conditioning emerges as a promising method to address these issues through physical or chemical means [205]. Physical methods like polishing or heat treatment have been employed to eliminate the Li_2CO_3/LiOH passivation layer, although complete impurity removal via polishing alone remains challenging. Elevated temperature treatment aids in breaking down Li_2CO_3 to form garnets without Li_2CO_3, as depicted in Fig. 15A. Chemical treatments, such as using acids like HCl or H_3PO_4, have proven effective in removing the passivation layer [206]. For instance, Wen et al. utilized H_3PO_4 to eliminate the passivation layer, forming desirable Li_3PO_4 with enhanced wettability and ionic conductivity, illustrated in Fig. 15B [164]. An alternative surface chemistry method involves creating a fluorinated interface to facilitate ionic diffusion. However, precise control over the acid treatment duration is crucial to preserve the garnet's volume and prevent further corrosion [207].

4.2.2 Doping of Exotic Elements

High grain boundary resistance is a critical factor leading to cell failure, especially in garnets. Two effective approaches involve doping exotic elements or inorganics into oxide SEs and optimizing the preparation processes. The former

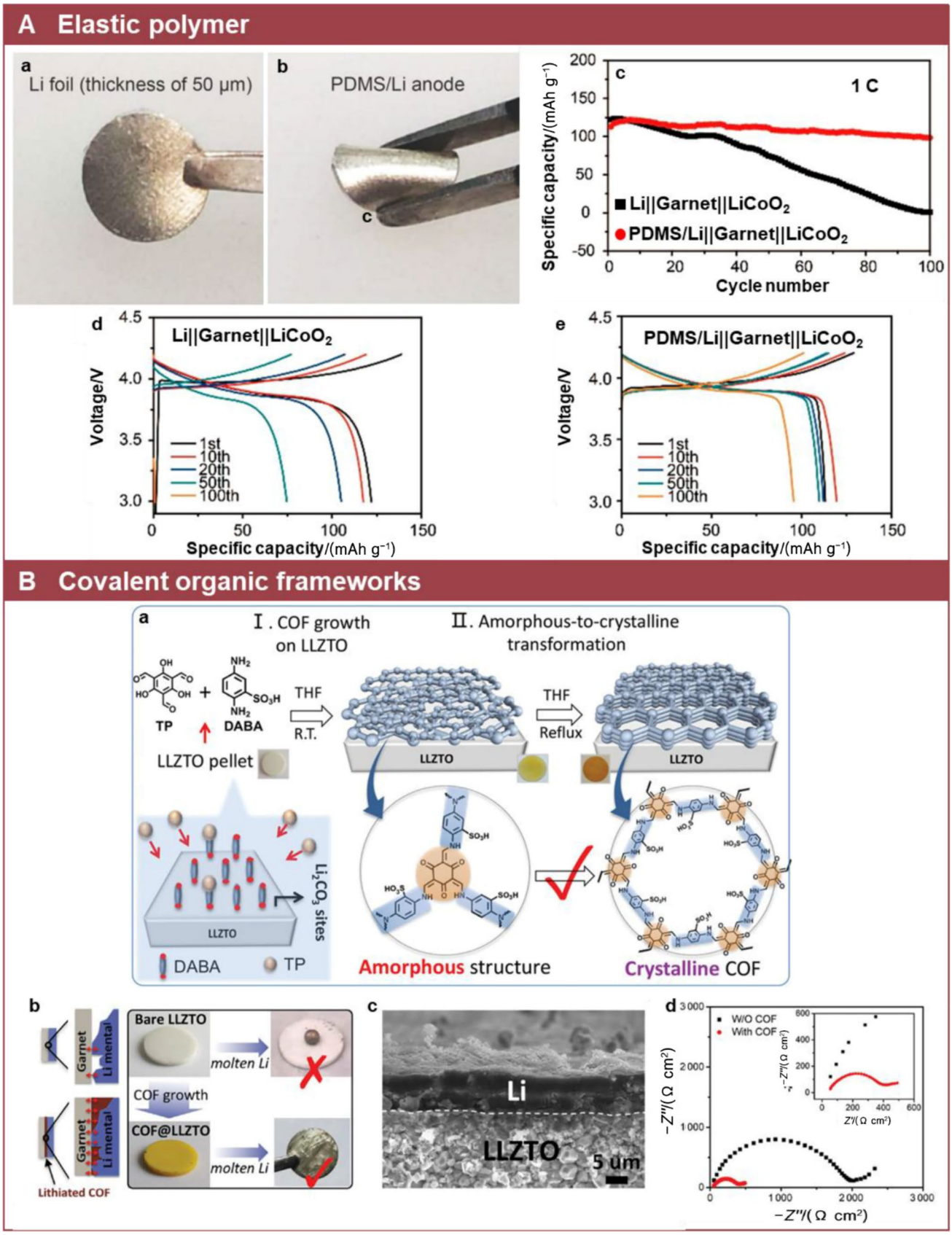
A Elastic polymer
a
Li foil (thickness of 50 μm)
b
PDMS/Li anode
c
1 C
Specific capacity/(mAh g⁻¹)
Cycle number
Li||Garnet||LiCoO2
PDMS/Li||Garnet||LiCoO2
d
Voltage/V
Specific capacity/(mAh g⁻¹)
1st
10th
20th
50th
100th
e
B Covalent organic frameworks
a
I. COF growth on LLZTO
II. Amorphous-to-crystalline transformation
TP
DABA
THF
R.T.
Reflux
LLZTO pellet
LLZTO
Li2CO3 sites
DABA
TP
Amorphous structure
Crystalline COF
b
Garnet
Li mental
Lithiated COF
Bare LLZTO
molten Li
COF growth
COF@LLZTO
molten Li
c
Li
LLZTO
5 um
d
W/O COF
With COF
−Z''/(Ω cm²)
Z'/(Ω cm²)

◂**Fig. 13** Organic materials interlayer between Li and garnets. **A** Integration of the Li anode with the PDMS substrate. **a** Optical illustration of Li foil. **b** Optical illustration of compressible PDMS/the Li soft anode. **c** Cycling performance of ASSLBs with and without PDMS with $LiCoO_2$ at 1 C for 100 cycles. **d** and **e** Electrochemical profiles of ASSLBs with and without PDMS after different cycles. Reprinted with permission from Ref. [188]. Copyright © 2020, ACS Publications. **B** Constructed COF interlayer between the Li anode and LLZTO. **a** Preparation process for building the COF interlayer on the garnet surface. **b** Comparison of wettability for molten Li on garnetw with and without COF interlayers. **c** Cross-section scanning electron microscopy of the interface between LLZTO and Li metal with COF interlayers. **d** EIS results of the symmetric cells with and without COF interlayers. Reprinted with permission from Ref. [191]. Copyright © 2020, John Wiley and Sons

method is a compelling strategy to enhance the relative density of oxide SEs, reducing microdefects like voids and pores while eliminating grain boundaries. For instance, Murugan et al. explored Al-doped $Li_7La_3Zr_2O_{12}$ with 1 wt% Li_4SiO_4 additives, achieving an impressive relative density of 98% [208]. Similarly, Ti-doping, Ta-substitution, and Al_2O_3-additives for garnets have shown promise in enhancing density and improving interfacial wettability [209–211]. These modifications result in garnets with a relative density exceeding 99%, significantly reducing grain boundary effects. Regarding the optimization of the preparation process, various strategies have been employed to enhance

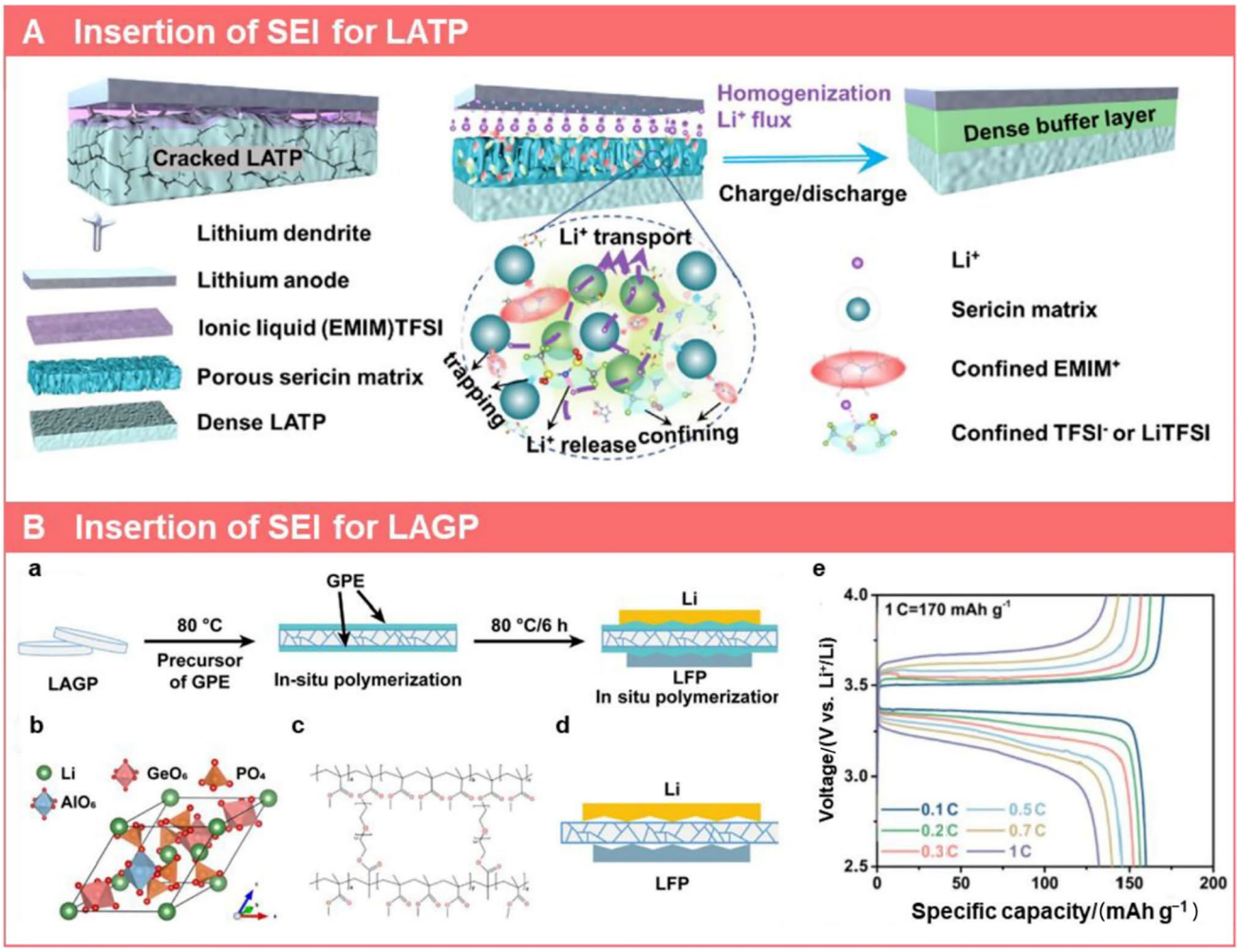

Fig. 14 Insertion of the SEI for NASICONs. **A** Schematic illustration of interface environment of Li/IL–LATP (left) and Li/IL@SPF–LATP (right) during cycling processes. Reprinted with permission from Ref. [199]. Copyright © 2022, Elsevier. **B** GPE layer for stabilizing the interface between LAGP and the Li anode. **a** Diagram of processes for preparing the GPE modified at the interface between LAGP and Li. **b** The crystal structure of LAGP. **c** The cross-linked PMMA's chemical structure. **d** Schematic illustration of ASSLBs with the pristine LAGP. **e** Charge/discharge profiles of ASSLBs at different rates at RT. Reprinted with permission from Ref. [204]. Copyright © 2022, Elsevier

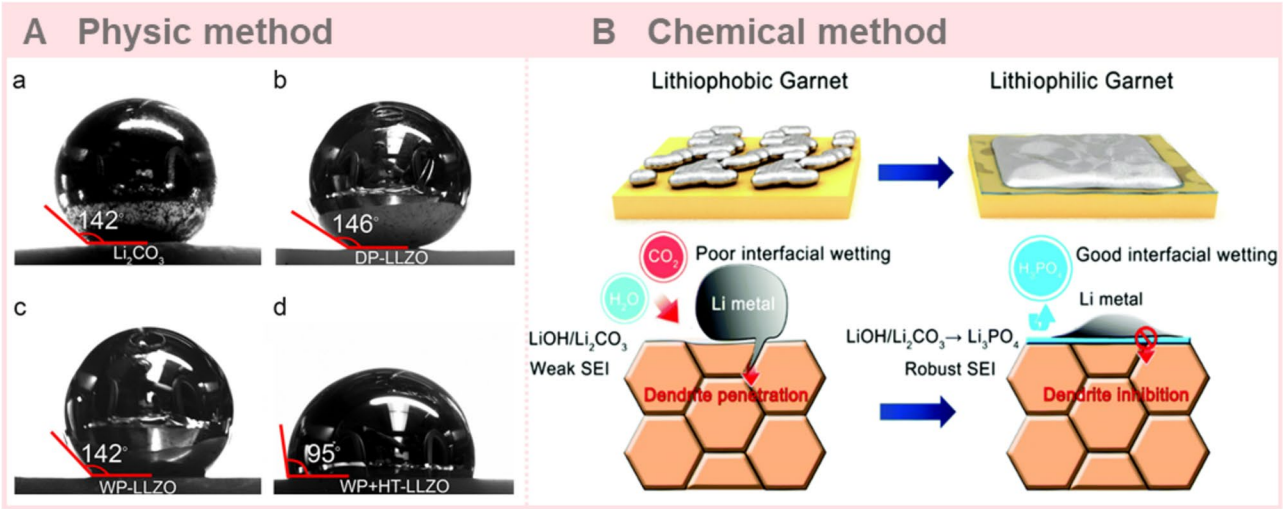

Fig. 15 Physic and chemical method for garnet surface conditioning. **A** Contact angle measurements for oxide SEs with different physical treatments for molten metallic Li. **a** Molten metallic Li on Li_2CO_3 without any treatment. **b** Molten metallic Li on dry polishing (DP) LLZO. **c** Molten metallic Li on wet polishing (WP) LLZO. **d** Molten metallic Li on wet-polishing–heat-treatment (DP–HT) LLZO. Reprinted with permission from Ref. [205]. Copyright © 2017, ACS Publications. **B** Diagram of processes for the Li_3PO_4 modified interlayer for improving the interface between garnet SEs and molten metallic Li. Reprinted with permission from Ref. [164]. Copyright © 2019, The Royal Society of Chemistry

the densification of oxide SEs. Techniques such as sintering processes, rapid induction hot pressing, and cold isostatic pressing have been pivotal in this regard [212–214]. Guo et al., utilizing flowing oxygen sintering technology, achieved garnets with an exceptional relative density of up to 96% and an impressive ionic conduction rate of 0.74 mS cm^{-1} [215]. Another innovative approach by Wen et al. involved a Li_2TiO_3-assisted sintering strategy for modifying grain boundaries in $Li_{6.5}La_3Zr_{1.5}Ta_{0.5}O_{12}$. The presence of Li_2TiO_3 at the grain boundary reduced electronic conductivity while enhancing mechanical properties and bonding strength in the modified oxide SEs [216].

4.2.3 Design of Electrolyte Structures

Due to the inherent challenge of establishing a strong connection between oxide SEs and the Li anode, applying high stack pressure has been a reliable method to eliminate pores and foster their contact. However, excessive pressure, acting as a driving force, can lead to mechanical short circuits in ASSLBs if it surpasses a critical threshold [86]. To address this issue, Cui et al. introduced an innovative three-dimensional (3D) micropatterned approach, ensuring a stable morphology at the Li metal interface even under limited stack pressure and high current density [217]. The adapted ASSLBs displayed exceptional performance, sustaining stable cycling for over 500 h at 0.5 mA cm^{-2}. This innovation mitigated local current density and reduced mechanical stress at the anode interface. The 3D framework, facilitating robust ionic conduction, played a pivotal role in suppressing Li dendrites [218–220]. Additionally, a multilayer design for LLZO has emerged as another viable strategy to address interfacial challenges, notably through bilayer and trilayer garnet frameworks [221]. Hu et al. introduced a 3D garnet framework, maintaining a porous-dense-porous (PDP) trilayer structure that concurrently supported both ionic and electronic conduction [220]. During controlled electrochemical deposition, this structure facilitated the formation of a 3D Li anode with increased contact area and reduced interfacial resistance. Similar PDP designs have been employed in Li-S batteries, resulting in outstanding specific capacities exceeding 1 200 mAh g^{-1} and nearly 100% Coulombic efficiency [219].

4.3 Composition of Li Anode

The optimal Li anode–garnets interface requires expansive contact, minimal interfacial resistance (< 100 Ω cm^2), and a dendrite-free environment. Creating composite Li anodes serves a dual purpose: reducing interfacial impedance and enhancing garnets' wettability. For example, casting 0.5 wt% Na-doped Li melt ($Li^{☆}$) on LLZTO surfaces successfully transferred impurities from the oxide SE's grain boundaries to the $Li^{☆}$ top layer (Fig. 16A) [222]. This innovative approach resolves wettability issues, enabling high-performance full cells with interfacial resistance < 1 Ω cm^2, a high current density of 1.5 mA cm^2, and a lifespan exceeding 1 250 cycles. A design strategy introduces a 3D $LiCu_x$ nanowire network infiltrated with Li metal at the Li–garnets interface, facilitating high-performance cells with a reversible

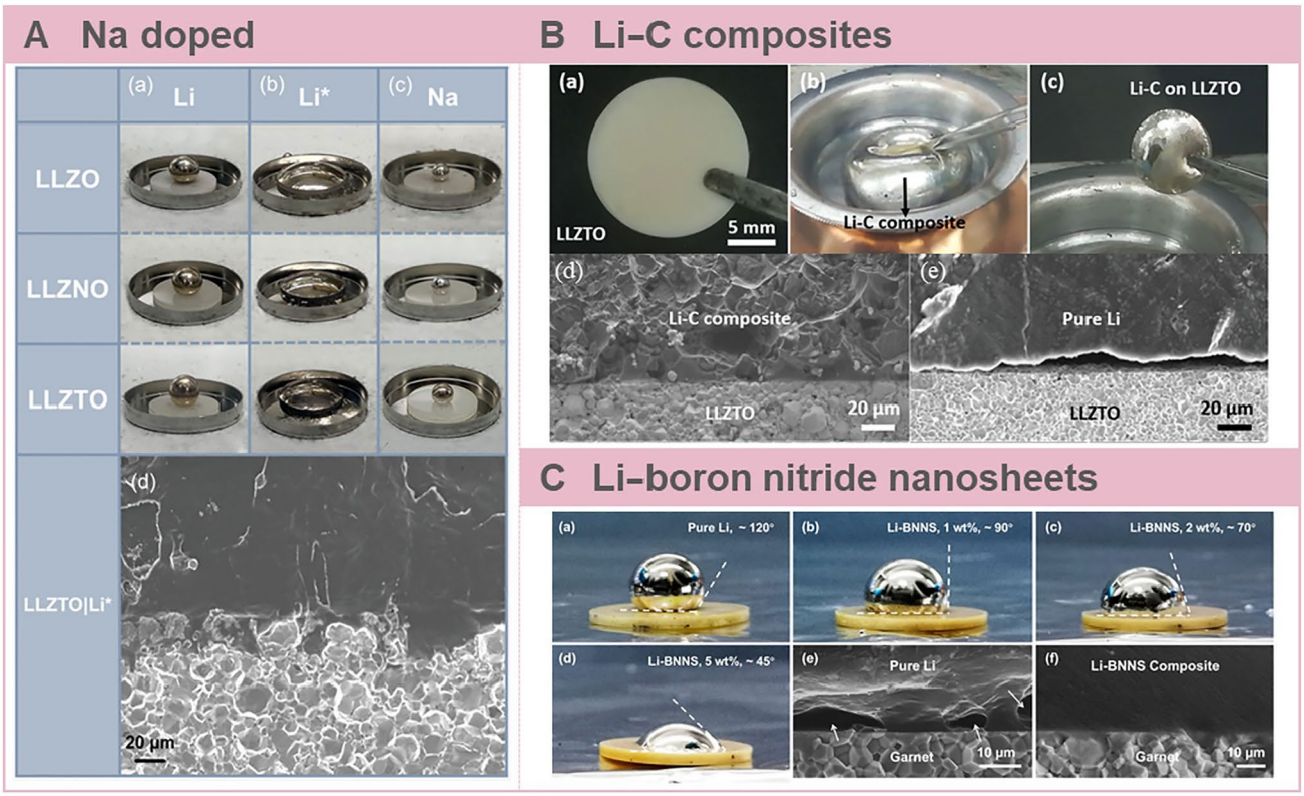

Fig. 16 Li metal modification for improving compatibility with oxide SEs. **A** The wettability performance of garnets toward different liquid metals. **a** The digital photos of Li on different garnet surfaces; **b** The digital photos of Li☆ on different garnet surfaces; **c** The digital photos of Na on different garnet surfaces. **d** Cross-section of scanning electron microscopy for Li☆–LLZTO interfaces. Reprinted with permission from Ref. [222]. Copyright © 2020, John Wiley and Sons. **B** Interfacial performance for the LLZTO/pure Li or Li–C composite anode. **a** The photos of the LLZTO surface. **b** Digital photos of molten Li–C. **c** Digital photos of molten Li–C on LLZTO. **d** Scanning electron microscopy images of the garnet/Li–C interface. **e** Scanning electron microscopy images of the garnet–pure Li interface. Reprinted with permission from Ref. [224]. Copyright © 2019, John Wiley and Sons. **C** Li-BNNS composite strategy for improving the garnet/Li interface. **a** Contact angle measurements of pure Li on garnets. **b** Contact angle measurements of Li-BNNS composites (1%). **c** Contact angle measurements of Li-BNNS composites (2%). **d** Contact angle measurements of Li-BNNS composites (5%). **e** Scanning electron microscopy images of pure Li–garnets. **f** Scanning electron microscopy images of pure Li-BNNS–garnets. Reprinted with permission from Ref. [225]. Copyright © 2019, ACS Publications

capacity of 147 mAh g^{-1} and long-term cycling capabilities [223]. Efforts to improve Li's viscosity and enhance the anode interface wettability remain paramount. While a low-fluidity, high-viscosity Li–C composite anode improves cell performance (Fig. 16B), lithiated Li–C's high electronic conductivity poses risks of MIEC interphase formation, leading to Li dendrite formation [224]. A solution arrives in the form of a high-viscosity Li-BN nanosheets (Li-BNNS) composite anode adhering to garnets, resulting in an in situ formed Li_3N interphase that effectively inhibits Li dendrite generation (Fig. 16C) [225]. Introducing $Li_{0.3}La_{0.5}TiO_3$ into the Li anode resolves the physical contact issue at the Li–garnets interface. This composite anode enhances anode interface wettability, decreases interfacial impedance, and offers additional Li storage owing to $Li_{0.3}La_{0.5}TiO_3$'s inherent storage capacity [226]. Similarly, the Li–Mo composite anode reduces cohesive energy and improves interfacial binding energy with garnets [227].

The pursuit of reducing interfacial impedance between garnets and Li anodes has been a central focus. Achieving a lithiophilic interphase to enhance wetting while simultaneously managing electronic conductivity to prevent Li dendrite formation poses a significant challenge. Balancing these factors in interface design has been a persistent challenge for researchers. Taking cues from biological functional gradient materials, Goodenough et al. devised a functional gradient Li anode (FGLA), comprising Li–LiAl–LiF with substantial interfacial energy differences, illustrated in Fig. 17A [228]. This FGLA not only lowers interfacial resistance but also supports a CCD exceeding 3.0 mA cm^{-2}. In a divergence from the lithiophilic interlayer strategy, Huang et al. introduced Sr doping into the Li anode to create a lithiophilic/lithiophobic bifunctional layer, encompassing Li–Sr/SrO-doped Li_2O, detailed in Fig. 17B. This bifunctional layer aims to inhibit reduction reactions between Li and oxide SEs by positioning the lithiophilic layer

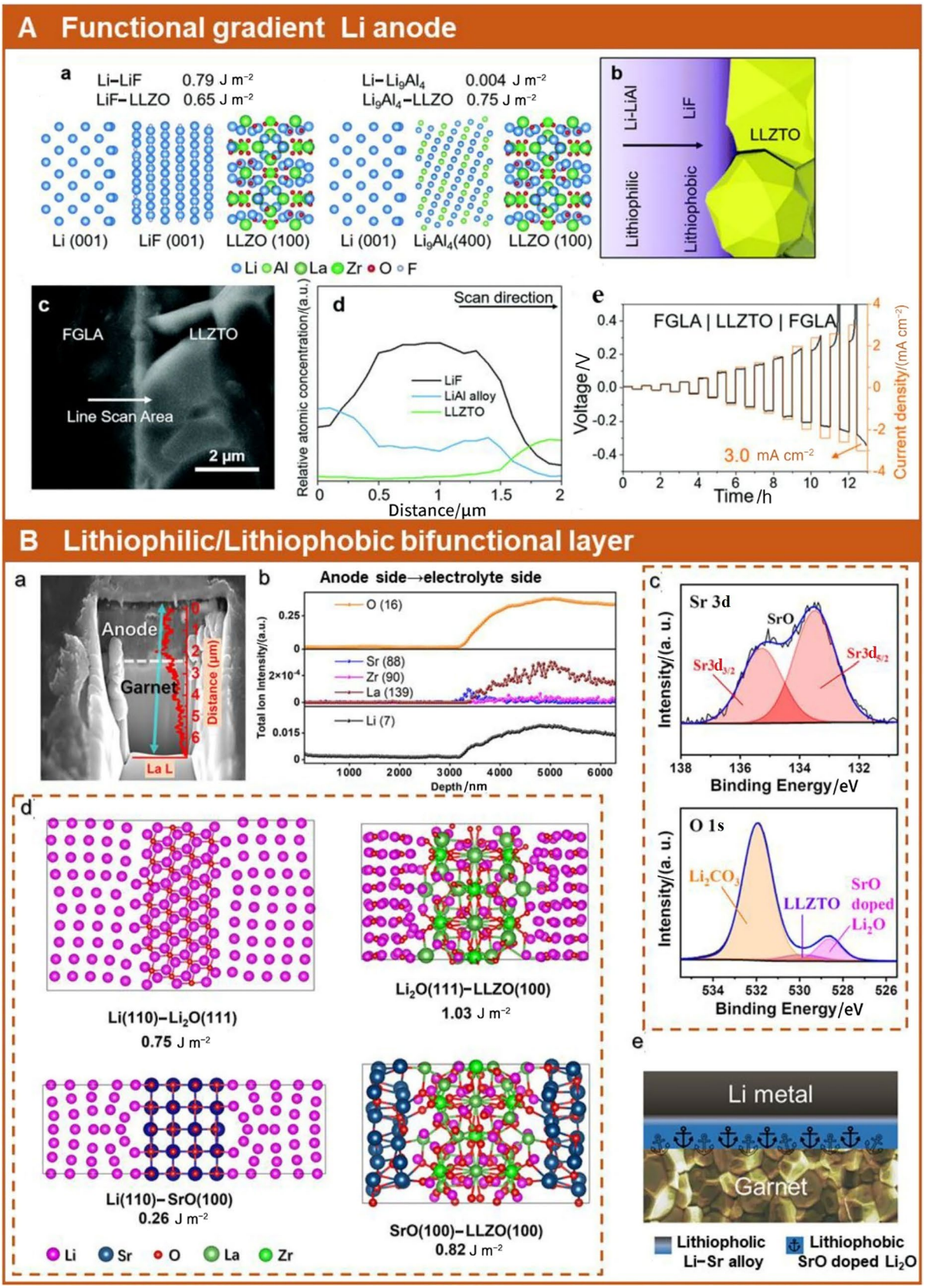
A Functional gradient Li anode
a
Li–LiF 0.79 J m-2
LiF–LLZO 0.65 J m-2
Li–Li9Al4 0.004 J m-2
Li9Al4–LLZO 0.75 J m-2
Li (001)
LiF (001)
LLZO (100)
Li (001)
Li9Al4(400)
LLZO (100)
Li Al La Zr O F
b
Li-LiAl
LiF
LLZTO
Lithiophilic
Lithiophobic
c
FGLA
LLZTO
Line Scan Area
2 μm
d
Scan direction
Relative atomic concentration/(a.u.)
LiF
LiAl alloy
LLZTO
Distance/μm
e
FGLA | LLZTO | FGLA
Voltage /V
Current density/(mA cm-2)
3.0 mA cm-2
Time /h
B Lithiophilic/Lithiophobic bifunctional layer
a
Anode
Garnet
La L
Distance (μm)
b
Anode side→electrolyte side
O (16)
Sr (88)
Zr (90)
La (139)
Li (7)
Total Ion Intensity/(a.u.)
Depth /nm
c
Sr 3d
SrO
Sr3d3/2
Sr3d5/2
Intensity/(a. u.)
Binding Energy/eV
O 1s
Li2CO3
LLZTO
SrO doped Li2O
Intensity/(a. u.)
Binding Energy/eV
d
Li(110)–Li2O(111)
0.75 J m-2
Li2O(111)–LLZO(100)
1.03 J m-2
Li(110)–SrO(100)
0.26 J m-2
SrO(100)–LLZO(100)
0.82 J m-2
Li Sr O La Zr
e
Li metal
Garnet
Lithiopholic Li–Sr alloy
Lithiophobic SrO doped Li2O

◂**Fig. 17** Composite Li anode to balance the low impedance and suppress Li dendrites. **A** The functional gradient Li anode strategy for improving anode–garnet interfaces. **a** The atomic structures and interfacial energies for different materials of Li, LiF, LLZTO and Li_9Al_4. **b** Schematic illustration of the FGLA strategy for improving the LLZTO–anode interface. **c** Scanning electron microscopy images of the FGLA–LLZTO interface. **d** Energy dispersive X-ray spectroscopy results of the FGLA–LLZTO interface. **e** CCD profiles of FGLA|LLZTO|FGLA symmetrical cells. Reprinted with permission from Ref. [228]. Copyright © 2022, John Wiley and Sons. **B** Lithiophilic/lithiophobic bifunctional layers for improving the Li–garnet interface. **a** Scanning electron microscopy images of the cross-section for the Li–Sr-1%|LLZTO interface. **b** TOF–SIMS profiles for the Li–Sr-1%|LLZTO interface. **c** XPS results for the Li–Sr-1%|LLZTO interface. **d** Atomic structures of the Li (110)–Li_2O (111) interface, the Li_2O (111)–garnet (100) interface, the Li (110)–SrO (100) interface, and the SrO (100)–garnet (100) interface, with the corresponding calculated interface energy γ by DFT. **e** Diagram of the Li–Sr alloy|SrO-doped Li_2O|garnet. Reprinted with permission from Ref. [229]. Copyright © 2022, ACS Publications

toward the Li anode and the lithiophobic layer toward the garnets [229].

5 Interfacial Engineering Toward Li and Polymer SEs

Unlike sulfide and oxide SEs, polymer-based SEs present advantages in adhesion to Li–polymer interfaces. However, practical applications still face various unresolved challenges. These include low Li^+ conductivity, elevated interfacial resistance, limited chemical and mechanical stability against Li metal, potential side reactions, and the formation and growth of Li dendrites. Moreover, the persistent hurdle of the shuttle effect leads to internal short circuits, self-discharge, and compromises in cycle efficiency for polymer SEs. Interactions between the polymer SEs, the lithium salt system, and the Li anode are pronounced, making the formation of a stable SEI difficult. This results in substantial interfacial resistance, even during cell inactivity. Addressing the interfacial issues within Li–polymer SEs necessitates enhancements in Li^+ conductivity and SEI stability, alongside bolstering the mechanical properties of polymer SEs to surpass a shear modulus of > 9.6 GPa [94]. Various design strategies, predominantly interlayer construction and electrolyte optimization, have been introduced to tackle these challenges.

5.1 Insertion of Interlayer

The formation of a stable SEI between the Li anode and polymer SEs stands as a pivotal factor in suppressing Li dendrite formation, ultimately ensuring exceptional cycle efficiency and longevity for the cells [230]. Zhou et al. delved into a series of polyoxalate (POE) structural polymer SEs terminating with trifluoroacetate (POE–F) units to lower the HOMO value and enhance antioxidative capacity [231]. Consequently, this approach facilitated the creation of a LiF-based interphase, optimizing the compatibility between Li and POE–F at the interface. Goodenough et al. proposed an in situ Li_3P interphase formation at the Li–polymer SEs interface using black phosphorus additives to reduce interfacial impedance and enhance the wettability of polymer SEs [232]. This interlayer exhibited robust adhesion to the Li anode, accommodating volume changes and mitigating internal stress during the cycling of assembled ASSLBs. Cui's group developed an ultrathin polymer SE comprising polyacrylonitrile (PAN)–PEO/LiTFSI with a PAN membrane matrix, displaying remarkable mechanical strength and effective suppression of Li dendrite formation. The resulting stable interphase, consisting of LiF and Li_3N (Fig. 18), was attributed to PEO for the LiF interphase and PAN for generating the Li_3N interphase [233]. PAN's robustness also enhances the safety and stability of assembled ASSLBs, ensuring improved performance even at higher temperatures. Compared to PEO-based counterparts, PVDF-based polymer SEs present a wider ESW, heightened mechanical strength, and superior ionic conductivity [234]. An intricately structured interphase with a mere 20 nm thickness emerged between the PVDF–LiFSI electrolyte and the Li anode, encompassing LiF, Li_2CO_3, Li_2O, and sulfur compounds [235]. This high ionic conductivity, low electronic conductivity, and impressive mechanical strength in the interphase promote uniform Li deposition and stripping during cycling.

Furthermore, ALD-prepared Al_2O_3 finds application in stabilizing the interface between the Li anode and PEO–LiTFSI polymer SEs, effectively curbing the shuttle effect caused by lithium polysulfides. This ALD–Al_2O_3 layer enhances the electrochemical properties of Li–S batteries, manifesting in heightened areal capacity, improved CE, and reduced self-discharge rates [236]. Addressing the compatibility concerns between the Li anode and polymer SEs, Shen et al. utilized a GO coating on PPC-based SE membranes, leading to the formation of reduced GO at the interface with the Li anode. This modification resulted in an enhanced ion conduction property (0.222 mS cm^{-1}), a widened ESW reaching up to 4.8 V, and improved Li^+ migration capability [237]. Similarly, a graphite layer serves as a protective element to enhance the compatibility between polymer SEs and Li, effectively suppressing Li dendrite formation [238].

In the realm of LEs-based LIBs, the integration of 3D structural Li anodes is considered a strategy to inhibit Li dendrites while providing an enlarged surface area with lithiophilic sites. Inspired by this concept, 3D structural Li/Cu mesh anodes [239] and 3D Li/Ni anodes [240] have been employed in assembling polymer SEs-based ASSLBs,

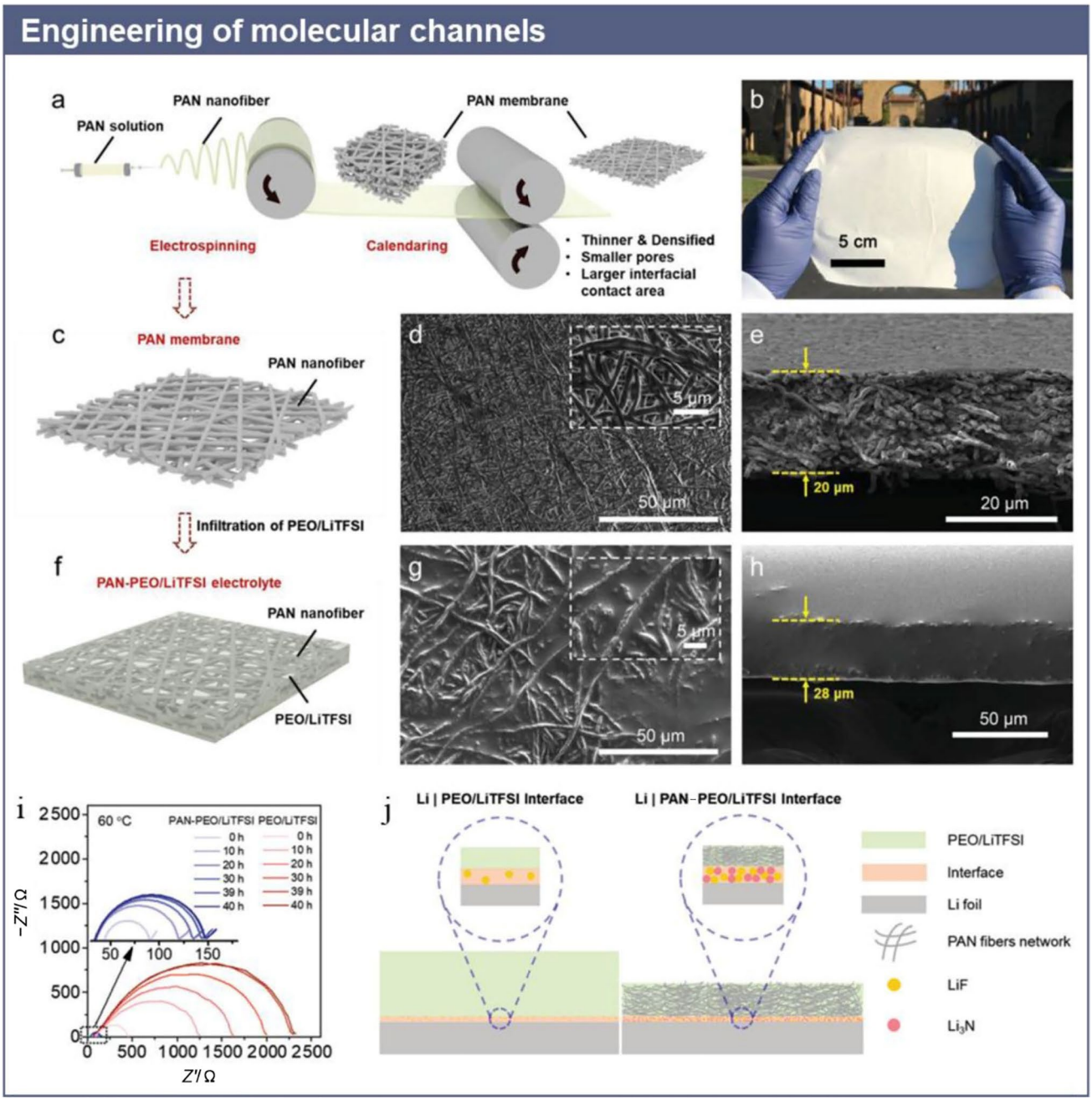

Fig. 18 a Diagram of preparation processes for PAN membranes. **b** Digital photo for PAN membranes. **c** Structure of PAN membranes. **d** SEM images of PAN membranes. **e** SEM images for the cross-section of PAN membranes. **f** Diagram of PAN–PEO/LiTFSI SEs. **g** SEM images of PAN–PEO/LiTFSI SEs. **h** SEM images for the cross-section of PAN–PEO/LiTFSI SEs. **i** EIS results for different times for symmetrical cells. **j** Diagram of the SE–Li interface, where the SE is with and without PAN. Reprinted with permission from Ref. [233]. Copyright © 2022, John Wiley and Sons.

showcasing exceptional cycling performance. However, relying solely on 3D Li anodes might not suffice in reducing local current density and optimizing physical contact with polymer SEs. Hence, it is imperative to complement these approaches with additional strategies for anode interfacial modification [56].

5.2 Optimization of Polymer SEs

In the domain of soft polymer SEs, enhancing the mechanical properties can effectively inhibit Li dendrite growth to a certain extent. Strategies to optimize polymer SEs encompass various approaches: incorporating fillers like inorganic materials, choosing high modulus polymer hosts,

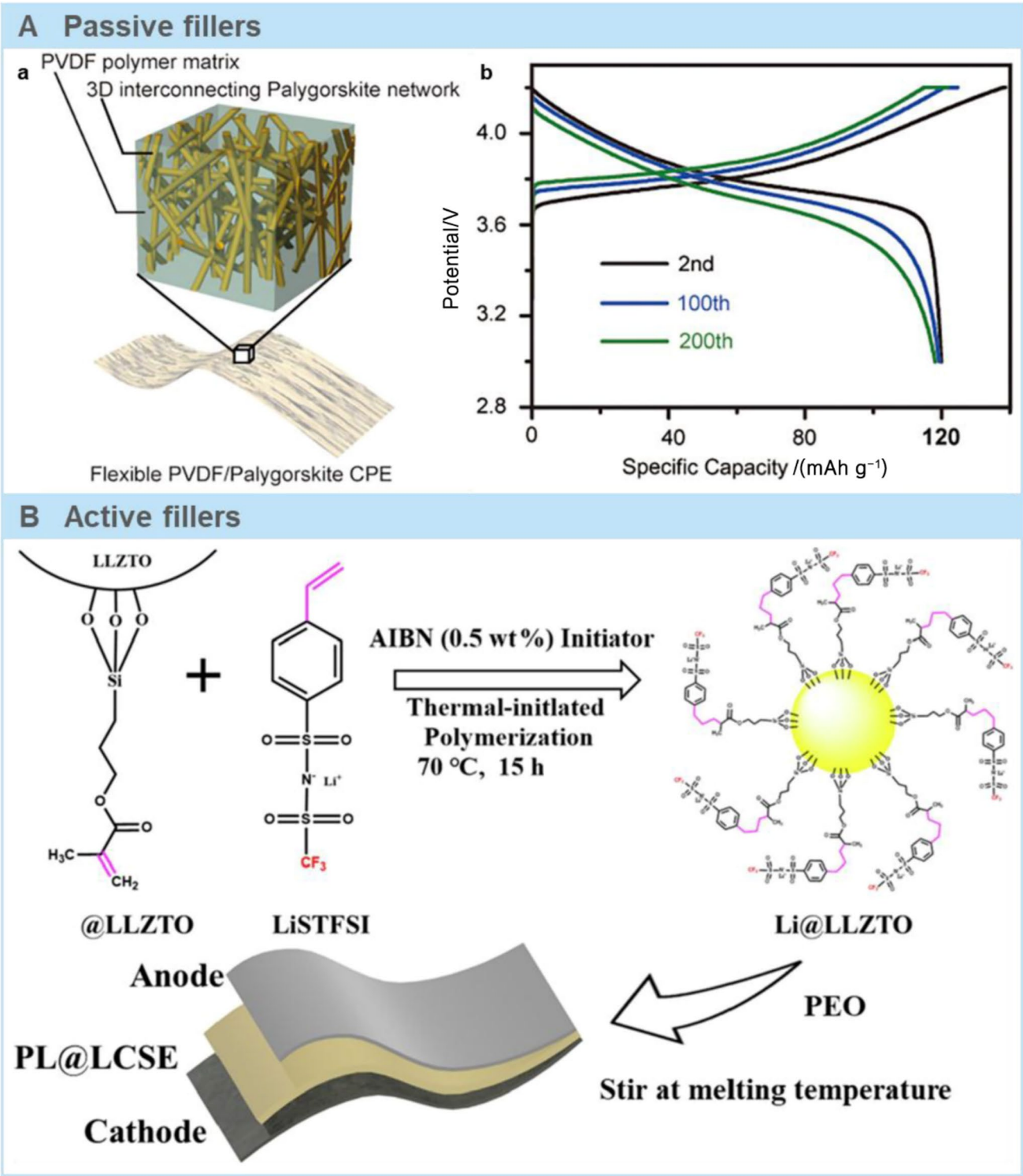

Fig. 19 Schematic illustration of fillers for polymer SEs to enhance properties. **A** PVDF/palygorskite nanowires CPE with passive fillers. **a** Schematic diagram of the PVDF/palygorskite CPE. **b** Voltage profile of NCM|PVDF/palygorskite nanowires|Li cells at 1 C. Reprinted with permission from Ref. [249]. Copyright © 2018, ACS Publications. **B** Polymer SEs with active fillers to form the PEO–Li@LLZTO composite electrolyte (PL@LCSE). **a** The diagram of PL@LCSE synthesis processes. Schematics of the difference on the surface of Li electrodes with **b** PLCSE and **c** PL@LCSE during Li plating/stripping processes. Reprinted with permission from Ref. [250]. Copyright © 2022, Elsevier

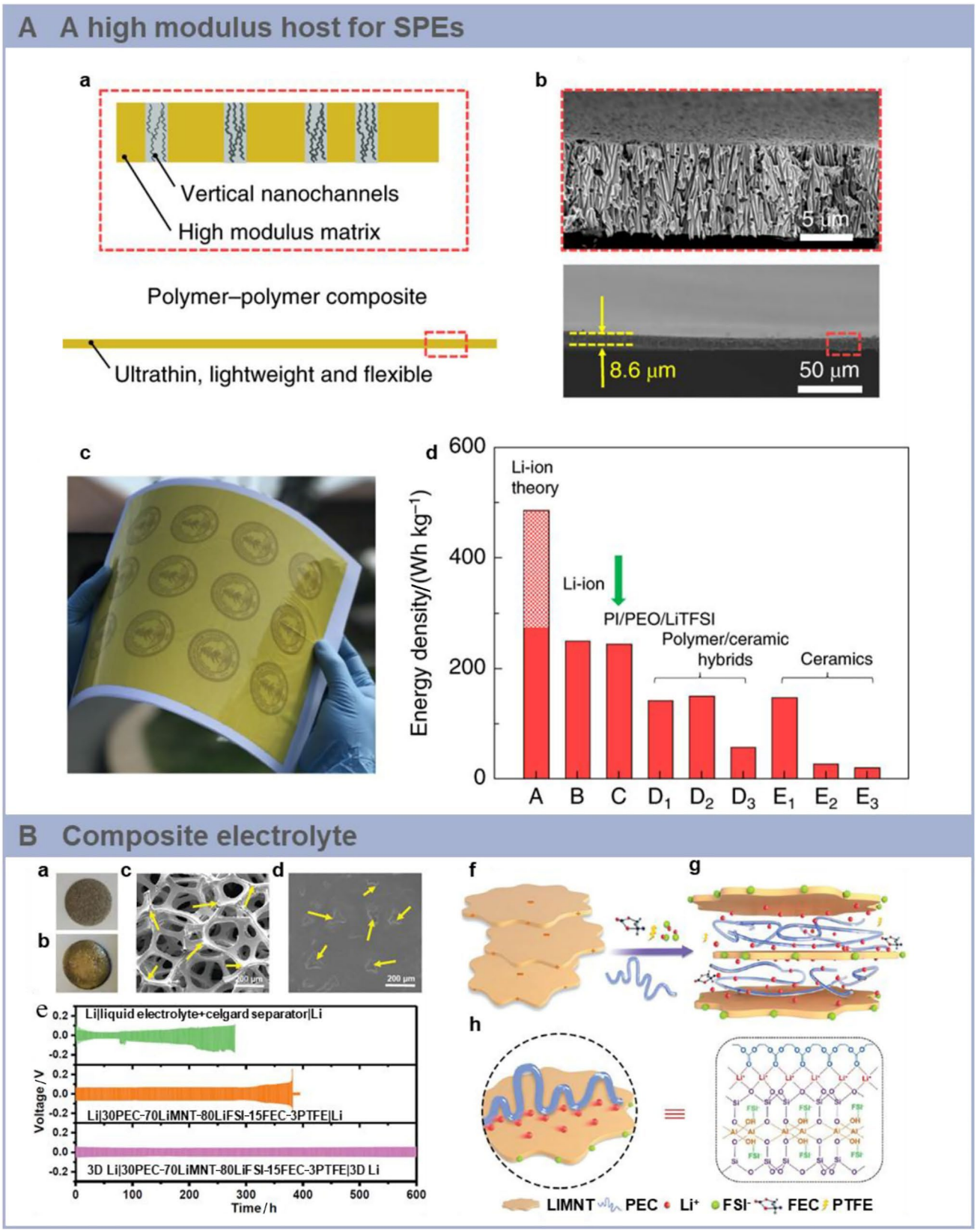
A A high modulus host for SPEs
a
Vertical nanochannels
High modulus matrix
Polymer–polymer composite
Ultrathin, lightweight and flexible
b
5 μm
8.6 μm
50 μm
c
d
Energy density/(Wh kg⁻¹)
Li-ion theory
Li-ion
PI/PEO/LiTFSI
Polymer/ceramic hybrids
Ceramics
A B C D1 D2 D3 E1 E2 E3
B Composite electrolyte
a
b
c
d
e
Li|liquid electrolyte+celgard separator|Li
Li|30PEC-70LiMNT-80LiFSI-15FEC-3PTFE|Li
3D Li|30PEC-70LiMNT-80LiFSI-15FEC-3PTFE|3D Li
Voltage / V
Time / h
f
g
h
LIMNT PEC Li+ FSI- FEC PTFE

◂**Fig. 20** **A** Design of ultrathin, lightweight and flexible composite polymer SEs. **a** Illustration of design principles for composite polymer SEs. **b** SEM images of the cross-section for the PI film. **c** Digital photo for the PI film. **d** Diagram of energy density with different electrolytes. Reprinted with permission from Ref. [54]. Copyright © 2019, Springer Nature. **B** An intercalated PEC–LiMNT CSE. **a** Digital images of the Ni foam. **b** Digital images of the Li–Ni composite. **c** SEM images of the Ni foam. **d** SEM images of the Li–Ni composite. **e** Long-term cycling performance for different systems for polymer SEs-based ASSLBs at 25 °C. **f–h** Principles of ion-transfer-number enhancement composite solid electrolytes. Reprinted with permission from Ref. [240]. Copyright © 2019, John Wiley and Sons

creating composite electrolytes, initiating cross-link networks through in situ lighting or heating, and engineering molecular channels. These techniques aim to augment ionic conductivity, bolster mechanical strength, and improve the interfacial stability of polymer SEs.

5.2.1 Addition of Fillers

Fillers integrated into polymer SEs facilitate the creation of composite polymer electrolytes (CPEs), employing a rigid-flexible coupling design that enhances Li^+ transference and interfacial stability, extends the ESW, and fortifies mechanical properties. These fillers encompass Li^+-insulating agents like Al_2O_3[241], SiO_2[242] and TiO_2[243], alongside Li^+-conductive substances such as LLZTO [244], LATP [197, 245, 246] and LAGP [247]. Using an in situ sol–gel method, Chen et al. developed a dual-network structure, combining 1 mol L^{-1} LiTFSI/[Py_{13}][TFSI], PEO, and Al_2O_3 [248]. This design broadened the ESW, enhanced nonflammability, and improved Li compatibility in PEO-based CPEs. The addition of Al_2O_3 aimed at augmenting the ionic conductivity of the CPE. Palygorskite ($(Mg,Al)_2Si_4O_{10}(OH)$) fibers as inorganic fillers create an interconnecting network within the polymer matrix, significantly enhancing mechanical properties. Yang et al. engineered CPEs using a PVDF polymer matrix and Palygorskite fillers, enhancing nonflammability, mechanical strength, ionic conduction, and the Li^+ transference number of the SEs (Fig. 19A) [249].

Li^+-conductive fillers are pivotal in Li^+ transport and suppressing Li dendrites compared to their Li^+-insulating counterparts. Zhang et al. coupled Li single-ion polymer (Li (4-styrenesulfonyl) (trifluoromethanesulfonyl) imide (LiSTFSI)) onto LLZTO surfaces via silane coupling to create PEO–Li@LLZTO composite electrolytes (PL@LCSE) [250]. This design effectively reduced PEO crystallinity and dendrite generation, showcasing exceptional cycling performance in the assembled full cell (Fig. 19B). PEO integrated with LLZTO, fluorinated carbonate (FEC), and SN additives produced a CPE with improved Li^+ transfer efficiency, exhibiting superior cycling performance (over 700 cycles at 1 C and RT) [251].

Furthermore, the addition of Li salts and plasticizers into polymer SEs enhances Li^+ conductivity and suppresses Li dendrites. For example, the introduction of Li_2S into PEO tackles its relatively low Li^+ conductivity, promoting the formation of a LiF-rich interphase. This effectively augments Li^+ diffusion capacity and curtails side reactions by inhibiting C–O bond breakage [196]. PVDF-based polymer SEs show reduced flammability compared to PEO-based SEs, presenting a promising avenue for solid-state electrolytes in ASSLBs [249].

5.2.2 Utilization of High Modulus Host

Overcoming the intrinsic softness and low ionic conductivity of polymer SEs involves utilizing a high modulus polymer host to optimize interfacial stability, augment ionic conduction, and bolster the hardness of polymer SEs for suppressing Li dendrite formation. In a study by Cui et al., a CPE was developed by embedding PEO/LiTFSI into a nano-porous polyimide (PI) film (8.6 μm thick), as depicted in Fig. 20A. The vertically aligned nanochannels within the PI film enhance ionic conductivity and $Li.^+$ transport rates, while the high modulus of the PI host effectively suppresses Li dendrite formation [54]. In another approach, Goodenough et al. highlighted the significance of a single polymer host's energy gap concerning Li plating and stripping processes under high voltage. Their work introduced a bilayer electrolyte comprising PEO interfacing with the Li anode and poly(*N*-methyl-malonic amide) interfacing with the cathode. This innovative electrolyte-based full cell showcased remarkable performance, notably Li dendrite-free operation and low impedance [81]. Research attention has been drawn toward CPEs employing diverse polymer matrices, showcasing higher ionic conductivity and mechanical strength at RT. Fan et al., for instance, utilized porous PI film and PVDF as hosts to create a CPE by incorporating LiTFSI salts and LLZTO filler. This CPE demonstrated improved mechanical properties and efficient suppression of Li dendrite formation [252].

5.2.3 Fabrication of Composite Electrolytes

Zhang et al. illustrated in Fig. 20B their development of a poly(ethylene carbonates)–Li montmorillonite CPE exhibiting desirable ionic conduction properties and a high Li^+ transference number of 0.83. The incorporation of Li montmorillonite improved electrochemical and thermal stability, while additives such as FEC and poly(tetrafluoroethylene) binders optimized ion conduction and film-forming properties. When coupled with a 3D Li anode, the assembled ASSLBs displayed exceptional performance with a Li dendrite-free characteristic [240]. Similarly, various CPEs utilizing different polymer hosts, including triblock

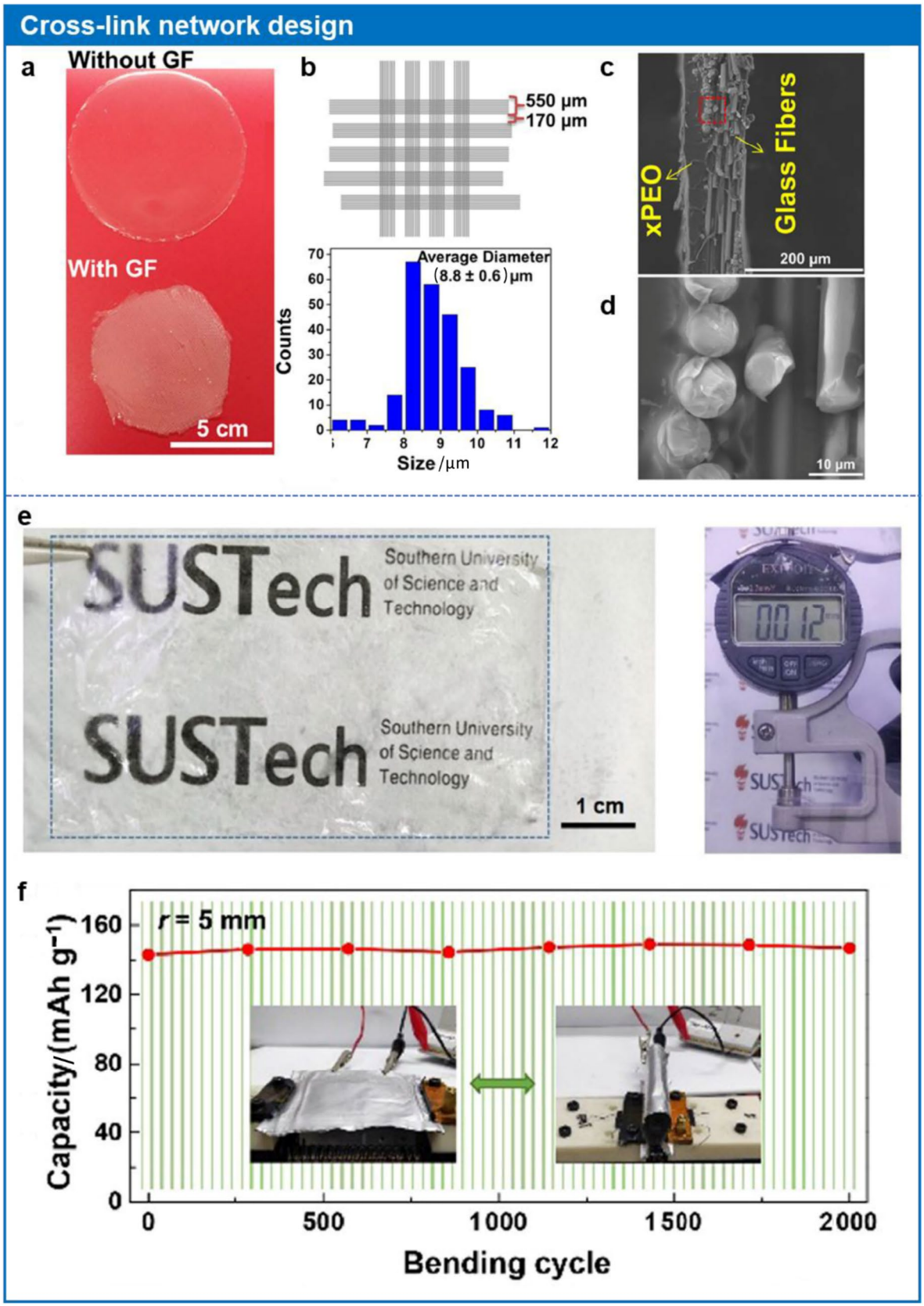
Cross-link network design
a
Without GF
With GF
5 cm
b
550 μm
170 μm
Average Diameter
(8.8 ± 0.6) μm
Counts
Size /μm
c
xPEO
Glass Fibers
200 μm
d
10 μm
e
SUSTech
Southern University of Science and Technology
1 cm
f
r = 5 mm
Capacity/(mAh g⁻¹)
Bending cycle

◂**Fig. 21** Cross-linked network polymer electrolytes. **a** Digital photo of cross-linked membranes with and without glass fibers. **b** Geometric construction and diameter distribution of glass fibers. **c** SEM images of the cross-section for the CPE. **d** Magnified view detailing of (c). Reprinted with permission from Ref. [95]. Copyright © 2021, Elsevier. **e** Optical photos of the ultrathin cross-linked polymer SE and SE thickness. **f** Specific capacity of the pouch cells under different bending tests. Reprinted with permission from Ref. [260]. Copyright © 2022, Elsevier

copolymer polystyrene–poly(ethylene glycol)–polystyrene (PS–PEG–PS) [253], sandwich-like poly(propylene carbonate)/polypropylene/poly(propylene carbonate) (PPC/PP/PPC) [254], and PEO–LiTFSI–Ni phosphate [255], exhibited high ionic conductivity and favorable compatibility with the Li anode. Elastomers, renowned for their mechanical elasticity and dispersion capabilities, have been recently introduced as polymer SE hosts for metal-based batteries (e.g., Na, K, Mg, Zn) via the polymerization-induced phase separation method [256]. Lee et al. innovated a plastic crystal-embedded elastomer electrolyte (PCEE) featuring mechanical robustness, acceptable Li^+ conductivity (1.1 mS cm^{-1}), and a high Li^+ transference number (0.75). The symmetric Li cell based on PCEE showed uniform morphologies without Li dendrite formation after 100 cycles at 10 mA cm^{-1}, owing to the formation of an inorganic–organic hybrid SEI layer. Furthermore, the asymmetric Li|PCEE|Cu cell demonstrated outstanding cycling performance with low voltage hysteresis below 26 mV and 100% Coulombic efficiency, achieving an exceptional energy density of 410 Wh kg^{-1}. Dimethyl sulfoxide (DMSO), known for its high flash point of 95 °C and a high dielectric permittivity of 47.2, is desirable for dissolving Li salts, although free DMSO molecules are unstable with a Li anode. To address this, Li et al. utilized DMSO as a Li^+ carrier and PVDF–HFP as a polymer matrix to create a solidified localized high-concentration electrolyte (S–LHCE) through a freeze-drying method [257]. This strategy enhanced compatibility with the Li anode, broadened the ESW, and decoupled electrolytes with a non-solvating solid framework. The stable interphase formed during cycling, composed of LiF at the anode interface, facilitated uniform Li deposition. Consequently, the assembled solid-state batteries exhibited exceptional electrochemical performance across a wide temperature range of − 10 to 100 °C.

5.2.4 Design of Cross-Link Networks

Polymer SEs featuring 3D cross-linked amorphous polymer hosts demonstrate exceptional mechanical robustness and ionic conduction, crucial for enhancing Li deposition uniformity on the anode and suppressing Li dendrite growth. In their work, Nanda et al. developed a cross-linked polymer SE derived from PEO and woven glass fiber matrices (Fig. 21a–e) [95]. This SE displayed a robust elastic modulus surpassing 1 GPa, effectively curbing Li dendrite formation, and showcased noteworthy ionic conductivity, moderate mechanical strength, and high tolerance to stretching during the manufacturing process. Li et al. introduced polymer SEs by cross-linking hierarchical structured g-C_3N_4, PEO, and LiTFSI, yielding SEs that offer excellent robustness and mechanical properties to inhibit Li dendrite growth even under substantial bending and prolonged cycling [258]. Consequently, the assembled cells demonstrated longevity with over 1 200 cycles and maintained an outstanding capacity (200 mAh g^{-1}) at a high rate of 5 C. Another compelling development involved a well-cross-linked polymer SE comprised of LiSTFSI and PEGDA with PC plasticizer on PAN nanofibers (SIPE–PAN–NFs), showcasing remarkable ionic conduction (0.809 mS cm^{-1} at RT), improved mechanical strength, flexibility, and excellent cycling performance [259]. Furthermore, an ultrathin cross-linked polymer SE, just 12 μm thick, was devised by integrating 1,3-dioxolane and trimethylolpropane triglycidyl ether (TTE) into a mesoporous polymer host releasing Li nitrate. This SE exhibited favorable ionic conductivity, high mechanical strength, a preferred SEI composed of Li_3N and LiF, and remarkable durability even with 2000 cycles of bending (Fig. 20f–h) [260]. Additionally, the cross-linking of polysiloxane-based polymer SEs with natural terpenes emerges as a promising avenue for ASSLBs, particularly in mitigating Li dendrite formation [261].

5.2.5 Engineering of Molecular Channels

Numerous promising polymer SEs have emerged from these methodologies. Yet, advancing novel strategies for improved polymer SEs remains imperative. Hu et al. pioneered a groundbreaking approach utilizing molecular channel engineering to craft a novel polymer SE by coordinating Cu^{2+} with cellulose nanofibrils (CNFs), resulting in an SE boasting outstanding attributes (Fig. 22) [262]. This innovation showcased exceptional ionic conduction (1.5 mS cm^{-1}), a wide ESW (0 − 4.5 V), strong compatibility with both the Li anode and cathode, and a high transference number (0.78). The one-dimensional CNFs, embedded with oxygen-containing polar functional groups derived from wood, play a pivotal role in facilitating Li^+ solvation and efficient Li^+ movement within the SE. Furthermore, the Li–Cu–CNFs composite exhibited versatility across various metals and polymers, setting a precedent for the development of other high-performance SEs.

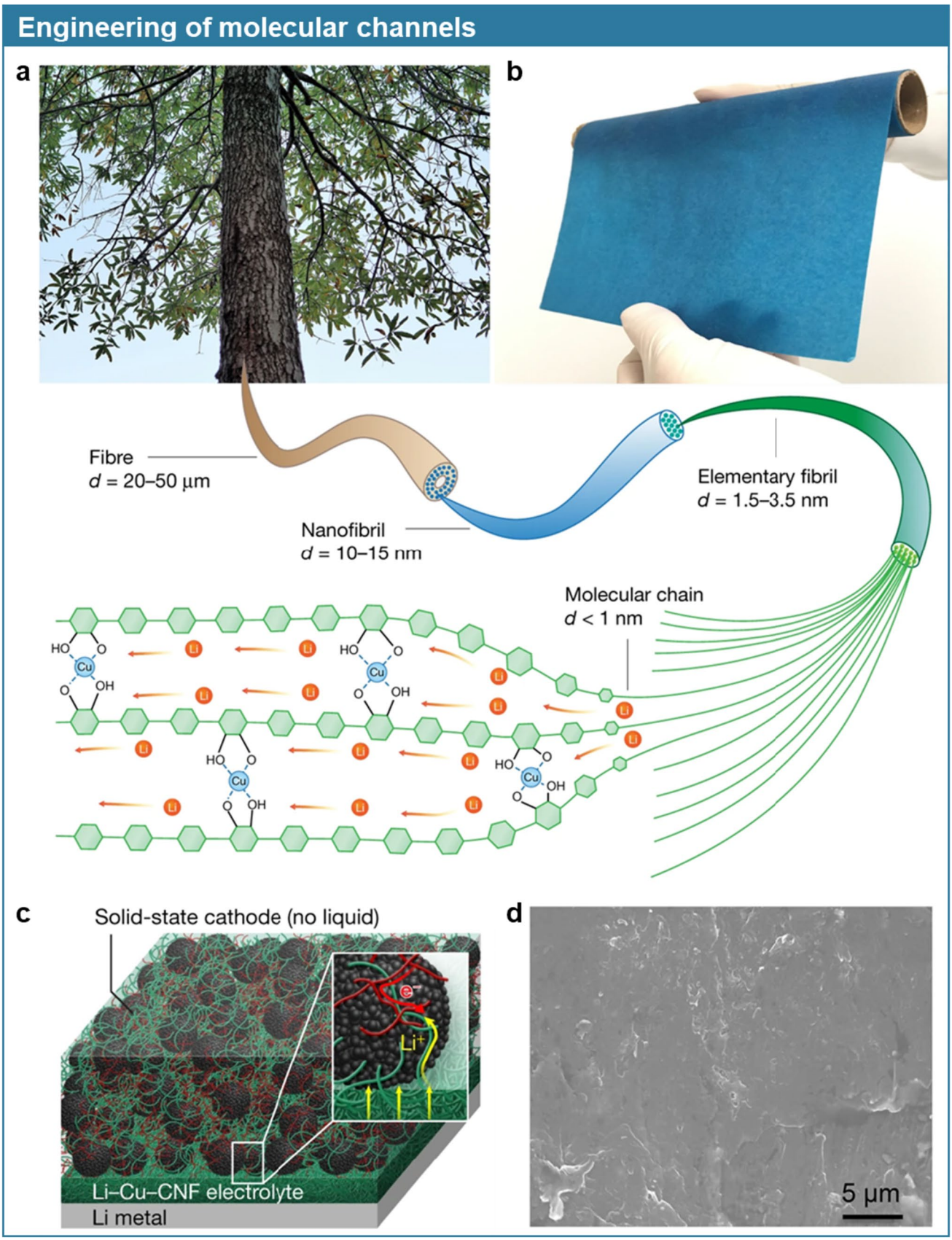
Engineering of molecular channels
a
b
Fibre
d = 20–50 µm
Nanofibril
d = 10–15 nm
Elementary fibril
d = 1.5–3.5 nm
Molecular chain
d < 1 nm
c
Solid-state cathode (no liquid)
Li–Cu–CNF electrolyte
Li metal
d
5 µm

◂**Fig. 22** Design concept of Li–Cu–CNF SEs. **a** Origins, structures and Li^+ transport pathways for Li–Cu–CNF. **b** Digital photo for the Li–Cu–CNF film. **c** Illustration of ASSLBs structure, including the Li anode, the Li–Cu–CNF SEs and the cathode with Li–Cu–CNF binders. **d** SEM image of the Li surface after long cycling for Li–Cu–CNF–based SEs ASSLBs. Reprinted with permission from Ref. [262]. Copyright © 2021, Springer Nature

6 Interfacial Engineering Toward Li and Halide SEs

Numerous studies have explored functional interlayers and electrolyte modifications to stabilize the interface between Li and halide SEs. While considerable efforts aim to establish a direct coupling between halide SEs and Li anodes, utilizing Li–In alloy or In foil [58, 60, 263–267] and $Li_{11}Sn_6$[268] remains an effective strategy to circumvent interfacial side reactions. Despite the limitation of direct contact between halide SEs and Li anode, they present promising potential as protective layers for cathodes due to their remarkable oxidation stability [269].

6.1 Insertion of Interlayer

Due to the inherent instability of halide electrolytes toward Li anodes, the use of an LPSC layer has been a common approach to stabilize the interface between halide SEs and Li. This strategy leverages the minimal interfacial ion transport resistance between sulfide SEs and halide SEs [111]. Among the halide SEs employed, Li_3YCl_6, Li_3ScCl_6, Li_3HoCl_6, and Li_3InCl_6 have been investigated [85, 269–271]. Sun et al. demonstrated that despite the thermodynamic instability of sulfide SEs toward Li anodes, the interaction between LPSC and Li generates a stable and conductive interface comprising Li_2S, Li_3P, and LiCl (depicted in Fig. 23A). This Li^+ conductive interface mitigates the compatibility issues between Li and Li_3YCl_6, showcasing a commendable initial CE of 98.1% [85].

6.2 Optimization of Halide SEs

6.2.1 Development of New Electrolytes

Yao et al. pioneered an innovative approach by employing stochastic surface walking global optimization in tandem with global neural network potential methods to strategically design halide SEs. Through this method, they identified two unique layered halide SE candidates: Li_2ZrCl_6 and Li_2HfCl_6, exhibiting exceptional stability (as depicted in Fig. 23B) [272]. The synthesized Li_2ZrCl_6 and Li_2HfCl_6 demonstrated unprecedented endurance against the Li anode, setting a remarkable record with a cycling time reaching 4 000 h. This groundbreaking utilization of machine learning strategies not only enhances the development of halide SEs but also presents a promising avenue for advancing SEs in ASSLBs.

6.2.2 Doping of Exotic Elements

The strategic doping of elements in SEs requires a delicate balance between enhancing ionic conductivity and widening the ESW. Pan et al. conducted an insightful study by doping varying amounts of Zr into Li_3ErCl_6, revealing that Zr doping improved the ionic conductivity of halide SEs but concurrently narrowed the ESW [267]. Employing a fluorine doping strategy optimized the stability of the Li–Li_3YBr_6 interface. The resultant $Li_3YBr_{5.7}F_{0.3}$ exhibited a wider ESW compared to Li_3YBr_6, attributed to the in situ formation of a fluorine-rich interlayer during the cycling process [274].

7 Summary and Outlook

In this review, recent progress in addressing critical interfacial challenges between Li anodes and various SEs—including sulfide, oxide, polymer, and halide SEs—has been discussed. These SEs present diverse physical, chemical, electrochemical, and mechanical properties, necessitating distinct strategies to mitigate their respective interfacial problems.

Sulfide SEs are regarded as promising options for commercial ASSLBs due to their high RT ionic conductivities, akin to liquid electrolytes, and good ductility. However, their limitations such as a narrow ESW, sensitivity to air and humidity, and high cost pose significant challenges. The main solutions involve integrating stable SEI layers—either in situ or ex situ—to curb parasitic reactions, optimizing electrolytes to minimize residual electron conductivity, and alloying the Li anode to prevent dendrite formation and undesirable interactions with sulfide SEs.

Oxide SEs encompass a broad spectrum, notably garnets and NASICONs, exhibiting excellent Li^+ conduction at room temperature (~ 1 mS cm^{-1}), mechanical robustness, and wider ESWs. While garnets' mechanical rigidity inhibits Li dendrite penetration, it also leads to less dense interfaces and higher resistance. Strategies include surface conditioning to remove impurities, doping to enhance density, and structural designs to reduce resistance. For NASICONs like LAGP and LATP, stable SEI interlayers effectively mitigate their poor stability toward Li anodes.

Polymer SEs boast flexibility, good adhesion, and membrane-forming capabilities, but suffer from low RT ionic conductivity, poor mechanical properties, narrow ESWs, and weak interfacial compatibility with Li anodes. Improving their intrinsic properties and integrating protective interlayers are crucial strategies to enhance ionic conductivity, mechanical strength, and compatibility with Li anodes, addressing interfacial impedance.

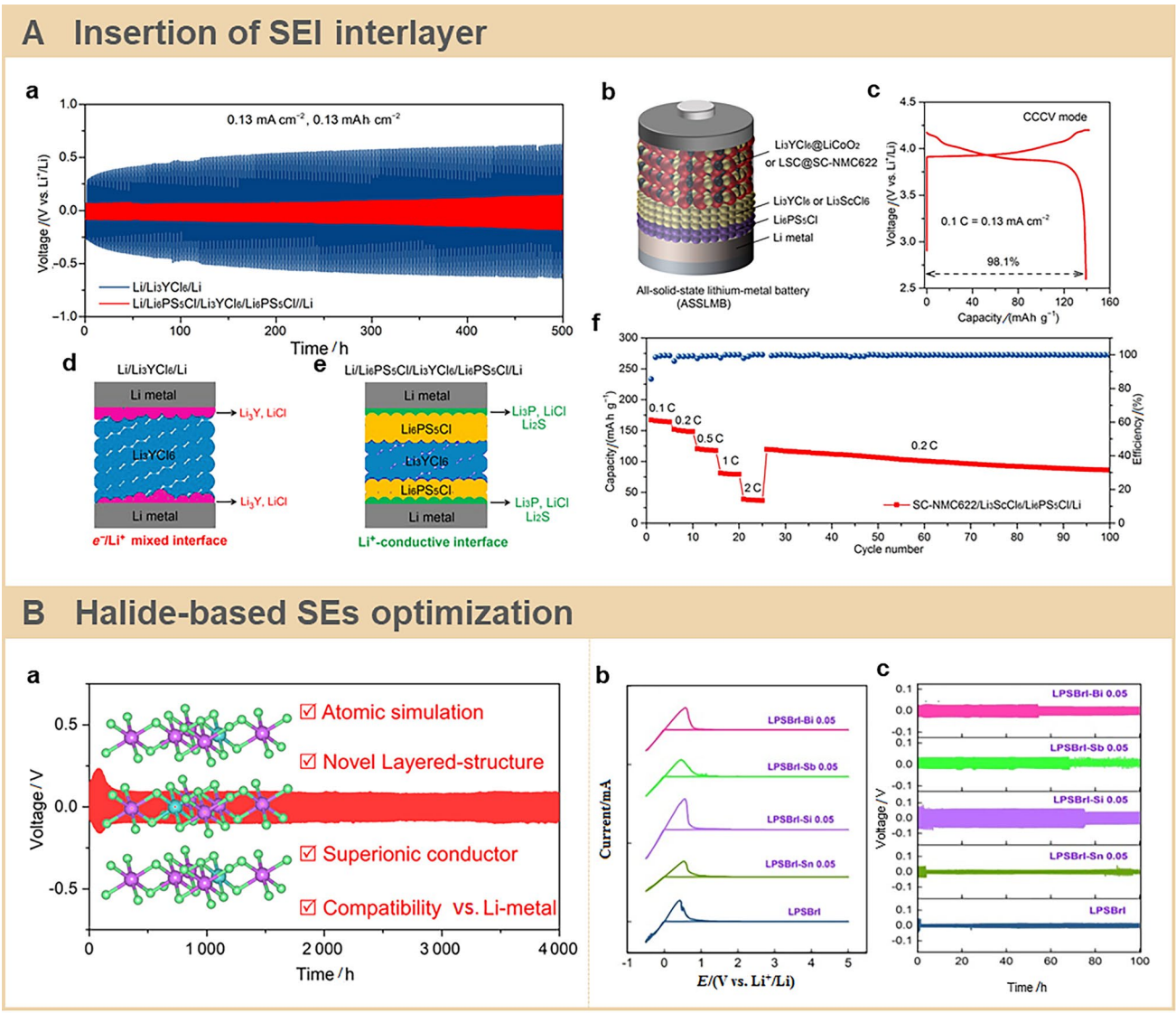

Fig. 23 Insertion of LPSC as an interlayer to stabilize the surface between the Li anode and Li_3YCl_6. **A a** The symmetric cell performance comparison with and without LPSC interlayers. **b** Schematic diagram of Li_3YCl_6-based ASSLBs. **c** The initial charge/discharge profiles for halide SEs-based ASSLBs. **d** The MIEC for the Li–Li_3YCl_6 interface. **e** LPSC protector for the Li–Li_3YCl_6 interface. **f** Rate performance of Li_3ScCl_6-based ASSLBs coupled with Li metal and NMC622, as well as the LPSC protector for the anode interface. Reprinted with permission from Ref. [85]. Copyright © 2021, Science family of journals/AAAS. **B** Development of new halide SEs with good compatibility toward Li metal. **a** Advantages and voltage of new halide SEs (Li_2ZrCl_6 and Li_2HfCl_6). Reprinted with permission from Ref. [272]. Copyright © 2022, ACS Publications. **b** CV graph of various metal-doped LPSBrI SEs. **c** DC charge–discharge graph of various metal-doped LPSBrI SEs. Reprinted with permission from Ref. [273]. Copyright © 2022, Elsevier

Halide SEs, lauded for their desirable RT ionic conductivity, wide ESWs, and excellent compatibility with oxide cathodes, yet face stability issues with Li anodes due to the high valence states of metal elements. Approaches often include utilizing LPSC interlayers or Li–In alloys instead of Li metal. Strategies involve optimizing halide SEs' stability, such as fluorine doping and exploring unique layered structures like Li_2ZrCl_6 and Li_2HfCl_6.

ASSLBs aim for a delicate balance between exceptional safety and robust electrochemical performance. Despite extensive strategies for anode interfacial engineering, there are still notable areas for improvement in SEs, Li anodes, and their interfaces in ASSLBs.

I. Multilayer SEs Exploration. Exploring multilayer SEs offers an opportunity to leverage the distinct advantages of individual SE layers while addressing stability issues at the electrode–SE interface. This approach allows the design of SEs structures that can withstand concurrent reduction and oxidation at the

anode and cathode. Luo et al. extensively summarize recent progress on multilayer SEs, emphasizing the potential of vertically hetero-structured designs [71]. However, additional interfacial engineering remains crucial to stabilize the anode interface, recognizing that no SEs are entirely immune to instability with Li metal.

II. SEI Interlayer Optimization. While SEI interlayers have proven successful in enhancing anode interfacial properties, practical ASSLBs still face challenges in accommodating high current density and real capacity. Designing an optimized 3D porous scaffold anode with superior ionic and electronic transport properties is crucial to achieving higher current density and area capacity.

III. Li Alloy Anode Consideration. Li alloy anodes, compared to Li anodes, offer enhanced stability to SEs. Notably, the volume change effect of Li alloy anodes in ASSLBs is more manageable than in LIBs. Various representative Li alloys, such as Li–In, Li–Al, Li–Ag, Ag–C and Li–Sn alloys, and pure Si anodes (forming Li–Si alloys during cycling), show promise. However, these alloys often have higher density and potential, thereby potentially reducing the overall energy density of ASSLBs. Therefore, the ideal alloy anode should exhibit lower density and potential while maintaining high compactness. Li–Si alloys, especially, emerge as a promising candidate for new commercial ASSLBs due to their properties.

Acknowledgements This work was financially sponsored by National Natural Science Foundation of China (Grant No. 52177218), the National Key Special Projects for International Cooperation in Science and Technology Innovation (2019YFE0100200) and Shanghai Pujiang Program (22PJ1408700).

Declarations

Conflict of interest The authors declare that they have no known competing financial interests or personal relationships that could have appeared to influence the work reported in this paper.

Open Access This article is licensed under a Creative Commons Attribution 4.0 International License, which permits use, sharing, adaptation, distribution and reproduction in any medium or format, as long as you give appropriate credit to the original author(s) and the source, provide a link to the Creative Commons licence, and indicate if changes were made. The images or other third party material in this article are included in the article's Creative Commons licence, unless indicated otherwise in a credit line to the material. If material is not included in the article's Creative Commons licence and your intended use is not permitted by statutory regulation or exceeds the permitted use, you will need to obtain permission directly from the copyright holder. To view a copy of this licence, visit http://creativecommons.org/licenses/by/4.0/.

References

1. Whittingham, M.S.: Electrical energy storage and intercalation chemistry. Science **192**, 1126–1127 (1976). https://doi.org/10.1126/science.192.4244.1126
2. Mizushima, K., Jones, P.C., Wiseman, P.J., et al.: Li_xCoO_2 ($0<x<1$): a new cathode material for batteries of high energy density. Mater. Res. Bull. **15**, 783–789 (1980). https://doi.org/10.1016/0025-5408(80)90012-4
3. Yoshino, A.: The birth of the lithium-ion battery. Angew. Chem. Int. Ed. **51**, 5798–5800 (2012). https://doi.org/10.1002/anie.201105006
4. Song, R.S., Ge, Y.Q., Wang, B., et al.: A new reflowing strategy based on lithiophilic substrates towards smooth and stable lithium metal anodes. J. Mater. Chem. A **7**, 18126–18134 (2019). https://doi.org/10.1039/c9ta05503g
5. Tan, D.H.S., Banerjee, A., Chen, Z., et al.: From nanoscale interface characterization to sustainable energy storage using all-solid-state batteries. Nat. Nanotechnol. **15**, 170–180 (2020). https://doi.org/10.1038/s41565-020-0657-x
6. Al-Salih, H., Houache, M.S.E., Baranova, E.A., et al.: Composite cathodes for solid-state lithium batteries: "catholytes" the underrated giants. Adv. Energy Sustain. Res. **3**, 2200032 (2022). https://doi.org/10.1002/aesr.202200032
7. Wu, J.H., Liu, S.F., Han, F.D., et al.: Lithium/sulfide all-solid-state batteries using sulfide electrolytes. Adv. Mater. **33**, 2000751 (2021). https://doi.org/10.1002/adma.202000751
8. Dietrich, C., Weber, D.A., Sedlmaier, S.J., et al.: Lithium ion conductivity in Li_2S–P_2S_5 glasses-building units and local structure evolution during the crystallization of superionic conductors Li_3PS_4, $Li_7P_3S_{11}$ and $Li_4P_2S_7$. J. Mater. Chem. A **5**, 18111–18119 (2017). https://doi.org/10.1039/C7TA06067J
9. Tatsumisago, M., Hayashi, A.: Superionic glasses and glass–ceramics in the Li_2S–P_2S_5 system for all-solid-state lithium secondary batteries. Solid State Ion. **225**, 342–345 (2012). https://doi.org/10.1016/j.ssi.2012.03.013
10. Zhang, Q., Cao, D.X., Ma, Y., et al.: Sulfide-based solid-state electrolytes: synthesis, stability, and potential for all-solid-state batteries. Adv. Mater. **31**, 1901131 (2019). https://doi.org/10.1002/adma.201901131
11. Homma, K., Yonemura, M., Nagao, M., et al.: Crystal structure of high-temperature phase of lithium ionic conductor, Li_3PS_4. J. Phys. Soc. Jpn. **79**, 90–93 (2010). https://doi.org/10.1143/jpsjs.79sa.90
12. Mizuno, F., Hayashi, A., Tadanaga, K., et al.: New, highly ion-conductive crystals precipitated from Li_2S–P_2S_5 glasses. Adv. Mater. **17**, 918–921 (2005). https://doi.org/10.1002/adma.200401286
13. Deiseroth, H.J., Kong, S.T., Eckert, H., et al.: Li_6PS_5X: a class of crystalline Li-rich solids with an unusually high Li^+ mobility. Angew. Chem. Int. Ed. Engl. **47**, 755–758 (2008). https://doi.org/10.1002/anie.200703900
14. Rao, R.P., Adams, S.: Studies of lithium argyrodite solid electrolytes for all-solid-state batteries. Phys. Status Solidi A **208**, 1804–1807 (2011). https://doi.org/10.1002/pssa.201001117
15. Bai, X.T., Duan, Y., Zhuang, W.D., et al.: Research progress in Li–argyrodite-based solid-state electrolytes. J. Mater. Chem. A **8**, 25663–25686 (2020). https://doi.org/10.1039/d0ta08472g
16. Feng, X.Y., Chien, P.H., Wang, Y., et al.: Enhanced ion conduction by enforcing structural disorder in Li-deficient argyrodites $Li_{6-x}PS_{5-x}Cl_{1+x}$. Energy Storage Mater. **30**, 67–73 (2020). https://doi.org/10.1016/j.ensm.2020.04.042
17. Kamaya, N., Homma, K., Yamakawa, Y., et al.: A lithium superionic conductor. Nat. Mater. **10**, 682–686 (2011). https://doi.org/10.1038/nmat3066

18. Kato, Y., Hori, S., Saito, T., et al.: High-power all-solid-state batteries using sulfide superionic conductors. Nat. Energy **1**, 16030 (2016). https://doi.org/10.1038/nenergy.2016.30
19. Iwasaki, R., Hori, S., Kanno, R., et al.: Weak anisotropic lithium-ion conductivity in single crystals of $Li_{10}GeP_2S_{12}$. Chem. Mater. **31**, 3694–3699 (2019). https://doi.org/10.1021/acs.chemmater.9b00420
20. Luo, W., Gong, Y.H., Zhu, Y.Z., et al.: Reducing interfacial resistance between garnet-structured solid-state electrolyte and Li-metal anode by a germanium layer. Adv. Mater. **29**, 1606042 (2017). https://doi.org/10.1002/adma.201606042
21. Hu, S.Q., Li, Y.F., Yang, R., et al.: Structure and ionic conductivity of $Li_7La_3Zr_{2-x}Ge_xO_{12}$ garnet-like solid electrolyte for all solid state lithium ion batteries. Ceram. Int. **44**, 6614–6618 (2018). https://doi.org/10.1016/j.ceramint.2018.01.065
22. Cussen, E.J.: Structure and ionic conductivity in lithium garnets. J. Mater. Chem. **20**, 5167–5173 (2010). https://doi.org/10.1039/B925553B
23. O'Callaghan, M.P., Lynham, D.R., Cussen, E.J., et al.: Structure and ionic-transport properties of lithium-containing garnets $Li_3Ln_3Te_2O_{12}$ (Ln = Y, Pr, Nd, Sm–Lu). Chem. Mater. **18**, 4681–4689 (2006). https://doi.org/10.1021/cm060992t
24. Cussen, E.J., Yip, T.W.S., O'Neill, G., et al.: A comparison of the transport properties of lithium-stuffed garnets and the conventional phases $Li_3Ln_3Te_2O_{12}$. J. Solid State Chem. **184**, 470–475 (2011). https://doi.org/10.1016/j.jssc.2010.12.021
25. Murugan, R., Thangadurai, V., Weppner, W.: Lattice parameter and sintering temperature dependence of bulk and grain-boundary conduction of garnet-like solid Li–electrolytes. J. Electrochem. Soc. **155**, A90 (2008). https://doi.org/10.1149/1.2800764
26. Murugan, R., Thangadurai, V., Weppner, W.: Fast lithium ion conduction in garnet-type $Li_7La_3Zr_2O_{12}$. Angew. Chem. Int. Ed. **46**, 7778–7781 (2007). https://doi.org/10.1002/anie.200701144
27. Percival, J., Kendrick, E., Smith, R.I., et al.: Cation ordering in Li containing garnets: synthesis and structural characterisation of the tetragonal system, $Li_7La_3Sn_2O_{12}$. Dalton Trans (2009). https://doi.org/10.1039/B907331K
28. Gupta, A., Murugan, R., Paranthaman, M.P., et al.: Optimum lithium-ion conductivity in cubic $Li_{7-x}La_3Hf_{2-x}Ta_xO_{12}$. J. Power. Sources **209**, 184–188 (2012). https://doi.org/10.1016/j.jpowsour.2012.02.099
29. Huang, X., Liu, C., Lu, Y., et al.: A Li-Garnet composite ceramic electrolyte and its solid-state Li–S battery. J. Power. Sources **382**, 190–197 (2018). https://doi.org/10.1016/j.jpowsour.2017.11.074
30. Wang, D.W., Zhu, C.B., Fu, Y.P., et al.: Interfaces in garnet-based all-solid-state lithium batteries. Adv. Energy Mater. **10**, 2001318 (2020). https://doi.org/10.1002/aenm.202001318
31. Zhu, Y.Z., He, X.F., Mo, Y.F.: Origin of outstanding stability in the lithium solid electrolyte materials: insights from thermodynamic analyses based on first-principles calculations. ACS Appl. Mater. Interfaces **7**, 23685–23693 (2015). https://doi.org/10.1021/acsami.5b07517
32. Han, F.D., Zhu, Y.Z., He, X.F., et al.: Electrochemical stability of $Li_{10}GeP_2S_{12}$ and $Li_7La_3Zr_2O_{12}$ solid electrolytes. Adv. Energy Mater. **6**, 1501590 (2016). https://doi.org/10.1002/aenm.201501590
33. Campanella, D., Belanger, D., Paolella, A.: Beyond garnets, phosphates and phosphosulfides solid electrolytes: new ceramic perspectives for all solid lithium metal batteries. J. Power. Sources **482**, 228949 (2021). https://doi.org/10.1016/j.jpowsour.2020.228949
34. Reddy, M.V., Julien, C.M., Mauger, A., et al.: Sulfide and oxide inorganic solid electrolytes for all-solid-state Li batteries: a review. Nanomaterials **10**, 1606 (2020). https://doi.org/10.3390/nano10081606
35. Goodenough, J.B., Hong, H.Y.P., Kafalas, J.A.: Fast Na^+-ion transport in skeleton structures. Mater. Res. Bull. **11**, 203–220 (1976). https://doi.org/10.1016/0025-5408(76)90077-5
36. Hong, H.Y.P.: Crystal structures and crystal chemistry in the system $Na_{1+x}Zr_2Si_xP_{3-x}O_{12}$. Mater. Res. Bull. **11**, 173–182 (1976). https://doi.org/10.1016/0025-5408(76)90073-8
37. Kohler, H., Schulz, H.: NASICON solid electrolytes part I: the Na^+-diffusion path and its relation to the structure. Mater. Res. Bull. **20**, 1461–1471 (1985). https://doi.org/10.1016/0025-5408(85)90164-3
38. Aono, H., Imanaka, N., Adachi, G.Y.: High Li^+ conducting ceramics. Acc. Chem. Res. **27**, 265–270 (1994). https://doi.org/10.1021/ar00045a002
39. Zheng, F., Kotobuki, M., Song, S.F., et al.: Review on solid electrolytes for all-solid-state lithium-ion batteries. J. Power. Sources **389**, 198–213 (2018). https://doi.org/10.1016/j.jpowsour.2018.04.022
40. Feng, J.K., Lu, L., Lai, M.O.: Lithium storage capability of lithium ion conductor $Li_{1.5}Al_{0.5}Ge_{1.5}(PO_4)_3$. J. Alloys Compd. **501**, 255–258 (2010). https://doi.org/10.1016/j.jallcom.2010.04.084
41. Itoh, M., Inaguma, Y., Jung, W.H., et al.: High lithium ion conductivity in the perovskite-type compounds $Ln_{12}Li_{12}TiO_3$(Ln=La, Pr, Nd, Sm). Solid State Ion. **70**(71), 203–207 (1994). https://doi.org/10.1016/0167-2738(94)90310-7
42. Inaguma, Y., Yu, J.D., Shan, Y.J., et al.: The effect of the hydrostatic pressure on the ionic conductivity in a perovskite lanthanum lithium titanate. J. Electrochem. Soc. **142**, L8–L11 (1995). https://doi.org/10.1149/1.2043988
43. Inaguma, Y., Itoh, M.: Influences of carrier concentration and site percolation on lithium ion conductivity in perovskite-type oxides. Solid State Ion. **86**(87/88), 257–260 (1996). https://doi.org/10.1016/0167-2738(96)00100-2
44. Fenton, D.E., Parker, J.M., Wright, P.V.: Complexes of alkali metal ions with poly(ethylene oxide). Polymer **14**, 589 (1973). https://doi.org/10.1016/0032-3861(73)90146-8
45. Xue, Z.G., He, D., Xie, X.L.: Poly(ethylene oxide)-based electrolytes for lithium-ion batteries. J. Mater. Chem. A **3**, 19218–19253 (2015). https://doi.org/10.1039/C5TA03471J
46. Wu, Y.X., Li, Y., Wang, Y., et al.: Advances and prospects of PVDF based polymer electrolytes. J. Energy Chem. **64**, 62–84 (2022). https://doi.org/10.1016/j.jechem.2021.04.007
47. Kim, J.U., Sung, C.H., Moon, S.I., et al.: Conductivity and transference number of poly(ethylene oxide)/poly(vinylidene fluoride) blend plasticized polymer electrolytes. In: Proceedings of 5th International Conference on Properties and Applications of Dielectric Materials. IEEE, pp. 646–649, Seoul, (1997). https://ieeexplore.ieee.org/document/616518
48. Kim, H.S., Paik, C.H., Cho, B.W., et al.: Discharge characteristics of an Li/$LiCoO_2$ cell with poly(acrylonitirile)-based polymer electrolyte. J. Power. Sources **68**, 361–363 (1997). https://doi.org/10.1016/S0378-7753(97)02654-2
49. Zhang, Z., Zhang, G.Z., Chao, L.: Three-dimensional fiber network reinforced polymer electrolyte for dendrite-free all-solid-state lithium metal batteries. Energy Storage Mater. **41**, 631–641 (2021). https://doi.org/10.1016/j.ensm.2021.06.030
50. Such, K., Stevens, J.R., Wieczorek, W., et al.: Polymer solid electrolytes from the PEG–PMMA–$LiCF_3SO_3$ system. J. Polym. Sci. B Polym. Phys. **32**, 2221–2233 (1994). https://doi.org/10.1002/polb.1994.090321309
51. Borah, S., Guha, A.K., Saikia, L., et al.: Nanofiber induced enhancement of electrical and electrochemical properties in polymer gel electrolytes for application in energy storage devices. J. Alloys Compd. **886**, 161173 (2021). https://doi.org/10.1016/j.jallcom.2021.161173
52. Lv, Z.L., Tang, Y., Dong, S.M., et al.: Polyurethane-based polymer electrolytes for lithium batteries: advances and perspectives. Chem. Eng. J. **430**, 132659 (2022). https://doi.org/10.1016/j.cej.2021.132659
53. Cong, B., Song, Y.X., Ren, N.Q., et al.: Polyethylene glycol-based waterborne polyurethane as solid polymer electrolyte for

all-solid-state lithium ion batteries. Mater. Des. **142**, 221–228 (2018). https://doi.org/10.1016/j.matdes.2018.01.039
54. Wan, J.Y., Xie, J., Kong, X., et al.: Ultrathin, flexible, solid polymer composite electrolyte enabled with aligned nanoporous host for lithium batteries. Nat. Nanotechnol. **14**, 705–711 (2019). https://doi.org/10.1038/s41565-019-0465-3
55. Wang, B.Y., Wang, G.X., He, P.G., et al.: Rational design of ultrathin composite solid-state electrolyte for high-performance lithium metal batteries. J. Membr. Sci. **642**, 119952 (2022). https://doi.org/10.1016/j.memsci.2021.119952
56. Ding, P.P., Lin, Z.Y., Guo, X.W., et al.: Polymer electrolytes and interfaces in solid-state lithium metal batteries. Mater. Today **51**, 449–474 (2021). https://doi.org/10.1016/j.mattod.2021.08.005
57. Liang, J.W., Li, X.N., Adair, K.R., et al.: Metal halide superionic conductors for all-solid-state batteries. Acc. Chem. Res. **54**, 1023–1033 (2021). https://doi.org/10.1021/acs.accounts.0c00762
58. Asano, T., Sakai, A., Ouchi, S., et al.: Solid halide electrolytes with high lithium-ion conductivity for application in 4 V class bulk-type all-solid-state batteries. Adv. Mater. **30**, 1803075 (2018). https://doi.org/10.1002/adma.201803075
59. Li, X.N., Liang, J.W., Yang, X.F., et al.: Progress and perspectives on halide lithium conductors for all-solid-state lithium batteries. Energy Environ. Sci. **13**, 1429–1461 (2020). https://doi.org/10.1039/C9EE03828K
60. Liu, Z.T., Ma, S., Liu, J., et al.: High ionic conductivity achieved in $Li_3Y(Br\ 3C_l3)$ mixed halide solid electrolyte via promoted diffusion pathways and enhanced grain boundary. ACS Energy Lett. **6**, 298–304 (2021). https://doi.org/10.1021/acsenergylett.0c01690
61. Emly, A., Kioupakis, E., Van der Ven, A.: Phase stability and transport mechanisms in antiperovskite Li_3OCl and Li_3OBr superionic conductors. Chem. Mater. **25**, 4663–4670 (2013). https://doi.org/10.1021/cm4016222
62. Wang, S., Bai, Q., Nolan, A.M., et al.: Lithium chlorides and bromides as promising solid-state chemistries for fast ion conductors with good electrochemical stability. Angew. Chem. Int. Ed. Engl. **58**, 8039–8043 (2019). https://doi.org/10.1002/anie.201901938
63. Wang, X.Y., He, K., Li, S.Y., et al.: Realizing high-performance all-solid-state batteries with sulfide solid electrolyte and silicon anode: a review. Nano Res. **16**, 3741–3765 (2023). https://doi.org/10.1007/s12274-022-4526-9
64. Lv, Q., Jiang, Y.P., Wang, B., et al.: Suppressing lithium dendrites within inorganic solid-state electrolytes. Cell Rep. Phys. Sci. **3**, 100706 (2022). https://doi.org/10.1016/j.xcrp.2021.100706
65. Paul, P.P., Chen, B.R., Langevin, S.A., et al.: Interfaces in all solid state Li-metal batteries: a review on instabilities, stabilization strategies, and scalability. Energy Storage Mater. **45**, 969–1001 (2022). https://doi.org/10.1016/j.ensm.2021.12.021
66. Liang, Y.H., Liu, H., Wang, G.X., et al.: Challenges, interface engineering, and processing strategies toward practical sulfide-based all-solid-state lithium batteries. InfoMat **4**, e12292 (2022). https://doi.org/10.1002/inf2.12292
67. Xu, K.: Interfaces and interphases in batteries. J. Power. Sources **559**, 232652 (2023). https://doi.org/10.1016/j.jpowsour.2023.232652
68. Lee, D., Lee, H., Song, T., et al.: Toward high rate performance solid-state batteries. Adv. Energy Mater. **12**, 2200948 (2022). https://doi.org/10.1002/aenm.202200948
69. Goodenough, J.B., Park, K.S.: The Li-ion rechargeable battery: a perspective. J. Am. Chem. Soc. **135**, 1167–1176 (2013). https://doi.org/10.1021/ja3091438
70. Schwietert, T.K., Arszelewska, V.A., Wang, C., et al.: Clarifying the relationship between redox activity and electrochemical stability in solid electrolytes. Nat. Mater. **19**, 428–435 (2020). https://doi.org/10.1038/s41563-019-0576-0
71. He, F., Hu, Z.L., Tang, W.J., et al.: Vertically heterostructured solid electrolytes for lithium metal batteries. Adv. Funct. Mater. **32**, 2201465 (2022). https://doi.org/10.1002/adfm.202201465
72. Wenzel, S., Leichtweiss, T., Krüger, D., et al.: Interphase formation on lithium solid electrolytes: an in situ approach to study interfacial reactions by photoelectron spectroscopy. Solid State Ion. **278**, 98–105 (2015). https://doi.org/10.1016/j.ssi.2015.06.001
73. Nolan, A.M., Zhu, Y.Z., He, X.F., et al.: Computation-accelerated design of materials and interfaces for all-solid-state lithium-ion batteries. Joule **2**, 2016–2046 (2018). https://doi.org/10.1016/j.joule.2018.08.017
74. Banerjee, A., Wang, X.F., Fang, C.C., et al.: Interfaces and interphases in all-solid-state batteries with inorganic solid electrolytes. Chem. Rev. **120**, 6878–6933 (2020). https://doi.org/10.1021/acs.chemrev.0c00101
75. Yan, M., Liang, J.Y., Zuo, T.T., et al.: Stabilizing polymer–lithium interface in a rechargeable solid battery. Adv. Funct. Mater. **30**, 1908047 (2020). https://doi.org/10.1002/adfm.201908047
76. Wenzel, S., Randau, S., Leichtweiß, T., et al.: Direct observation of the interfacial instability of the fast ionic conductor $Li_{10}GeP_2S_{12}$ at the lithium metal anode. Chem. Mater. **28**, 2400–2407 (2016). https://doi.org/10.1021/acs.chemmater.6b00610
77. Xiao, Y.H., Wang, Y., Bo, S.H., et al.: Understanding interface stability in solid-state batteries. Nat. Rev. Mater. **5**, 105–126 (2019). https://doi.org/10.1038/s41578-019-0157-5
78. Richards, W.D., Miara, L.J., Wang, Y., et al.: Interface stability in solid-state batteries. Chem. Mater. **28**, 266–273 (2016). https://doi.org/10.1021/acs.chemmater.5b04082
79. Li, J.C., Ma, C., Chi, M.F., et al.: Lithium-ion batteries: solid electrolyte: the key for high-voltage lithium batteries (adv. energy mater. 4/2015). Adv. Energy Mater. **5**, 1401408 (2015). https://doi.org/10.1002/aenm.201570018
80. Hartmann, P., Leichtweiss, T., Busche, M.R., et al.: Degradation of NASICON-type materials in contact with lithium metal: formation of mixed conducting interphases (MCI) on solid electrolytes. J. Phys. Chem. C **117**, 21064–21074 (2013). https://doi.org/10.1021/jp4051275
81. Zhou, W.D., Wang, Z.X., Pu, Y., et al.: Double-layer polymer electrolyte for high-voltage all-solid-state rechargeable batteries. Adv. Mater. **31**, 1805574 (2019). https://doi.org/10.1002/adma.201805574
82. Duan, H., Fan, M., Chen, W.P., et al.: Extended electrochemical window of solid electrolytes via heterogeneous multilayered structure for high-voltage lithium metal batteries. Adv. Mater. **31**, 1807789 (2019). https://doi.org/10.1002/adma.201807789
83. Khurana, R., Schaefer, J.L., Archer, L.A., et al.: Suppression of lithium dendrite growth using cross-linked polyethylene/poly(ethylene oxide) electrolytes: a new approach for practical lithium–metal polymer batteries. J. Am. Chem. Soc. **136**, 7395–7402 (2014). https://doi.org/10.1021/ja502133j
84. Lu, Q.W., Fang, J.H., Yang, J., et al.: A novel solid composite polymer electrolyte based on poly(ethylene oxide) segmented polysulfone copolymers for rechargeable lithium batteries. J. Membr. Sci. **425**(426), 105–112 (2013). https://doi.org/10.1016/j.memsci.2012.09.038
85. Wang, C.H., Liang, J.W., Luo, J., et al.: A universal wet-chemistry synthesis of solid-state halide electrolytes for all-solid-state lithium-metal batteries. Sci. Adv. **7**, eabh1896 (2021). https://doi.org/10.1126/sciadv.abh1896
86. Doux, J.M., Nguyen, H., Tan, D.H.S., et al.: Stack pressure considerations for room-temperature all-solid-state lithium metal batteries. Adv. Energy Mater. **10**, 1903253 (2020). https://doi.org/10.1002/aenm.201903253
87. Pang, Y.P., Pan, J.Y., Yang, J.H., et al.: Electrolyte/electrode interfaces in all-solid-state lithium batteries: a review.

Electrochem. Energy Rev. **4**, 169–193 (2021). https://doi.org/10.1007/s41918-020-00092-1
88. Han, X.G., Gong, Y.H., Fu, K., et al.: Negating interfacial impedance in garnet-based solid-state Li metal batteries. Nat. Mater. **16**, 572–579 (2017). https://doi.org/10.1038/nmat4821
89. Huo, H.Y., Chen, Y., Li, R.Y., et al.: Design of a mixed conductive garnet/Li interface for dendrite-free solid lithium metal batteries. Energy Environ. Sci. **13**, 127–134 (2020). https://doi.org/10.1039/C9EE01903K
90. Feng, X.Y., Fang, H., Wu, N., et al.: Review of modification strategies in emerging inorganic solid-state electrolytes for lithium, sodium, and potassium batteries. Joule **6**, 543–587 (2022). https://doi.org/10.1016/j.joule.2022.01.015
91. Ha, H.J., Kil, E.H., Kwon, Y.H., et al.: UV-curable semi-interpenetrating polymer network-integrated, highly bendable plastic crystal composite electrolytes for shape-conformable all-solid-state lithium ion batteries. Energy Environ. Sci. **5**, 6491–6499 (2012). https://doi.org/10.1039/C2EE03025J
92. Nagao, M., Hayashi, A., Tatsumisago, M., et al.: In situ SEM study of a lithium deposition and dissolution mechanism in a bulk-type solid-state cell with a Li_2S–P_2S_5 solid electrolyte. Phys. Chem. Chem. Phys. **15**, 18600–18606 (2013). https://doi.org/10.1039/C3CP51059J
93. Porz, L., Swamy, T., Sheldon, B.W., et al.: Mechanism of lithium metal penetration through inorganic solid electrolytes. Adv. Energy Mater. **7**, 1701003 (2017). https://doi.org/10.1002/aenm.201701003
94. Monroe, C., Newman, J.: The impact of elastic deformation on deposition kinetics at lithium/polymer interfaces. J. Electrochem. Soc. **152**, A396 (2005). https://doi.org/10.1149/1.1850854
95. Yang, G., Lehmann, M.L., Zhao, S., et al.: Anomalously high elastic modulus of a poly(ethylene oxide)-based composite electrolyte. Energy Storage Mater. **35**, 431–442 (2021). https://doi.org/10.1016/j.ensm.2020.11.031
96. Kasemchainan, J., Zekoll, S., Spencer Jolly, D., et al.: Critical stripping current leads to dendrite formation on plating in lithium anode solid electrolyte cells. Nat. Mater. **18**, 1105–1111 (2019). https://doi.org/10.1038/s41563-019-0438-9
97. Sarkar, S., Thangadurai, V.: Critical current densities for high-performance all-solid-state Li–metal batteries: fundamentals, mechanisms, interfaces, materials, and applications. ACS Energy Lett. **7**, 1492–1527 (2022). https://doi.org/10.1021/acsenergylett.2c00003
98. Liang, J.W., Li, X.N., Zhao, Y., et al.: An air-stable and dendrite-free Li anode for highly stable all-solid-state sulfide-based Li batteries. Adv. Energy Mater. **9**, 1902125 (2019). https://doi.org/10.1002/aenm.201902125
99. Fan, X.L., Ji, X., Han, F.D., et al.: Fluorinated solid electrolyte interphase enables highly reversible solid-state Li metal battery. Sci. Adv. **4**, eaau9245 (2018). https://doi.org/10.1126/sciadv.aau9245
100. Xu, R.C., Han, F.D., Ji, X., et al.: Interface engineering of sulfide electrolytes for all-solid-state lithium batteries. Nano Energy **53**, 958–966 (2018). https://doi.org/10.1016/j.nanoen.2018.09.061
101. Zhao, F.P., Sun, Q., Yu, C., et al.: Ultrastable anode interface achieved by fluorinating electrolytes for all-solid-state Li metal batteries. ACS Energy Lett. **5**, 1035–1043 (2020). https://doi.org/10.1021/acsenergylett.0c00207
102. Su, H., Liu, Y., Zhong, Y., et al.: Stabilizing the interphase between Li and argyrodite electrolyte through synergistic phosphating process for all-solid-state lithium batteries. Nano Energy **96**, 107104 (2022). https://doi.org/10.1016/j.nanoen.2022.107104
103. Xu, H.J., Cao, G.Q., Shen, Y.L., et al.: Enabling argyrodite sulfides as superb solid-state electrolyte with remarkable interfacial stability against electrodes. Energy Environ. Mater. **5**, 852–864 (2022). https://doi.org/10.1002/eem2.12282
104. Wang, Y.H., Yue, J.P., Wang, W.P., et al.: Constructing a stable interface between the sulfide electrolyte and the Li metal anode via a Li^+-conductive gel polymer interlayer. Mater. Chem. Front. **5**, 5328–5335 (2021). https://doi.org/10.1039/D1QM00395J
105. Li, J.R., Su, H., Li, M., et al.: A deformable dual-layer interphase for high-performance $Li_{10}GeP_2S_{12}$-based solid-state Li metal batteries. Chem. Eng. J. **431**, 134019 (2022). https://doi.org/10.1016/j.cej.2021.134019
106. Gao, Y., Wang, D.W., Li, Y.C., et al.: Salt-based organic–inorganic nanocomposites: towards a stable lithium metal/$Li_{10}GeP_2S_{12}$ solid electrolyte interface. Angew. Chem. Int. Ed. **57**, 13608–13612 (2018). https://doi.org/10.1002/anie.201807304
107. Duan, C., Cheng, Z., Li, W., et al.: Realizing the compatibility of a Li metal anode in an all-solid-state Li−S battery by chemical iodine–vapor deposition. Energy Environ. Sci. **15**, 3236–3245 (2022). https://doi.org/10.1039/D2EE01358D
108. Zhang, Z.H., Chen, S.J., Yang, J., et al.: Interface re-engineering of $Li_{10}GeP_2S_{12}$ electrolyte and lithium anode for all-solid-state lithium batteries with ultralong cycle life. ACS Appl. Mater. Interfaces **10**, 2556–2565 (2018). https://doi.org/10.1021/acsami.7b16176
109. Chen, Y.M., Wang, Z.Q., Li, X.Y., et al.: Li metal deposition and stripping in a solid-state battery via Coble creep. Nature **578**, 251–255 (2020). https://doi.org/10.1038/s41586-020-1972-y
110. Su, Y.B., Ye, L.H., Fitzhugh, W., et al.: A more stable lithium anode by mechanical constriction for solid state batteries. Energy Environ. Sci. **13**, 908–916 (2020). https://doi.org/10.1039/C9EE04007B
111. Ye, L.H., Li, X.: A dynamic stability design strategy for lithium metal solid state batteries. Nature **593**, 218–222 (2021). https://doi.org/10.1038/s41586-021-03486-3
112. Gil-González, E., Ye, L.H., Wang, Y.C., et al.: Synergistic effects of chlorine substitution in sulfide electrolyte solid state batteries. Energy Storage Mater. **45**, 484–493 (2022). https://doi.org/10.1016/j.ensm.2021.12.008
113. Alarco, P.J., Abu-Lebdeh, Y., Abouimrane, A., et al.: The plastic-crystalline phase of succinonitrile as a universal matrix for solid-state ionic conductors. Nat. Mater. **3**, 476–481 (2004). https://doi.org/10.1038/nmat1158
114. MacFarlane, D.R., Forsyth, M.: Plastic crystal electrolyte materials: new perspectives on solid state ionics. Adv. Mater. **13**, 957–966 (2001). https://doi.org/10.1002/1521-4095(200107)13:12/13957:aid-adma957%3e3.0.co;2-#
115. Wang, C.H., Adair, K.R., Liang, J.W., et al.: Solid-state plastic crystal electrolytes: effective protection interlayers for sulfide-based all-solid-state lithium metal batteries. Adv. Funct. Mater. **29**, 1900392 (2019). https://doi.org/10.1002/adfm.201900392
116. Kazyak, E., Wood, K.N., Dasgupta, N.P.: Improved cycle life and stability of lithium metal anodes through ultrathin atomic layer deposition surface treatments. Chem. Mater. **27**, 6457–6462 (2015). https://doi.org/10.1021/acs.chemmater.5b02789
117. Jung, S.C., Han, Y.K.: How do Li atoms pass through the Al_2O_3 coating layer during lithiation in Li-ion batteries? J. Phys. Chem. Lett. **4**, 2681–2685 (2013). https://doi.org/10.1021/jz401231e
118. Kozen, A.C., Lin, C.F., Pearse, A.J., et al.: Next-generation lithium metal anode engineering via atomic layer deposition. ACS Nano **9**, 5884–5892 (2015). https://doi.org/10.1021/acsnano.5b02166
119. Zhang, Z.H., Wu, L.P., Zhou, D., et al.: Flexible sulfide electrolyte thin membrane with ultrahigh ionic conductivity for all-solid-state lithium batteries. Nano Lett. **21**, 5233–5239 (2021). https://doi.org/10.1021/acs.nanolett.1c01344
120. Wang, C.H., Zhao, Y., Sun, Q., et al.: Stabilizing interface between $Li_{10}SnP_2S_{12}$ and Li metal by molecular layer deposition.

Nano Energy **53**, 168–174 (2018). https://doi.org/10.1016/j.nanoen.2018.08.030
121. Ji, X., Hou, S., Wang, P.F., et al.: Solid-state electrolyte design for lithium dendrite suppression. Adv. Mater. **32**, 2002741 (2020). https://doi.org/10.1002/adma.202002741
122. Kato, A., Suyama, M., Hotehama, C., et al.: High-temperature performance of all-solid-state lithium-metal batteries having Li/Li_3PS_4 interfaces modified with Au thin films. J. Electrochem. Soc. **165**, A1950–A1954 (2018). https://doi.org/10.1149/2.1451809jes
123. Su, J., Pasta, M., Ning, Z.Y., et al.: Interfacial modification between argyrodite-type solid-state electrolytes and Li metal anodes using LiPON interlayers. Energy Environ. Sci. **15**, 3805–3814 (2022). https://doi.org/10.1039/D2EE01390H
124. Zhu, Y.Z., He, X.F., Mo, Y.F.: First principles study on electrochemical and chemical stability of solid electrolyte-electrode interfaces in all-solid-state Li-ion batteries. J. Mater. Chem. A **4**, 3253–3266 (2016). https://doi.org/10.1039/C5TA08574H
125. Xiao, R.J., Li, H., Chen, L.Q.: High-throughput design and optimization of fast lithium ion conductors by the combination of bond-valence method and density functional theory. Sci. Rep. **5**, 14227 (2015). https://doi.org/10.1038/srep14227
126. Wang, X.L., Xiao, R.J., Li, H., et al.: Oxygen-driven transition from two-dimensional to three-dimensional transport behaviour in β-Li_3PS_4 electrolyte. Phys. Chem. Chem. Phys. **18**, 21269–21277 (2016). https://doi.org/10.1039/C6CP03179J
127. Chen, T., Zhang, L., Zhang, Z.X., et al.: Argyrodite solid electrolyte with a stable interface and superior dendrite suppression capability realized by ZnO co-doping. ACS Appl. Mater. Interfaces **11**, 40808–40816 (2019). https://doi.org/10.1021/acsami.9b13313
128. Liu, G.Z., Xie, D.J., Wang, X.L., et al.: High air-stability and superior lithium ion conduction of $Li_{3+3x}P_{1-x}Zn_xS_{4-x}O_x$ by aliovalent substitution of ZnO for all-solid-state lithium batteries. Energy Storage Mater. **17**, 266–274 (2019). https://doi.org/10.1016/j.ensm.2018.07.008
129. Trevey, J.E., Gilsdorf, J.R., Miller, S.W., et al.: Li_2S–Li_2O–P_2S_5 solid electrolyte for all-solid-state lithium batteries. Solid State Ion. **214**, 25–30 (2012). https://doi.org/10.1016/j.ssi.2012.02.034
130. Ohtomo, T., Hayashi, A., Tatsumisago, M., et al.: Characteristics of the Li_2O–Li_2S–P_2S_5 glasses synthesized by the two-step mechanical milling. J. Non Cryst. Solids **364**, 57–61 (2013). https://doi.org/10.1016/j.jnoncrysol.2012.12.044
131. Xie, D.J., Chen, S.J., Zhang, Z.H., et al.: High ion conductive Sb_2O_5-doped β-Li_3PS_4 with excellent stability against Li for all-solid-state lithium batteries. J. Power. Sources **389**, 140–147 (2018). https://doi.org/10.1016/j.jpowsour.2018.04.021
132. Cengiz, M., Oh, H., Lee, S.H.: Lithium dendrite growth suppression and ionic conductivity of Li_2S–P_2S_5–P_2O_5 Glass solid electrolytes prepared by mechanical milling. J. Electrochem. Soc. **166**, A3997–A4004 (2019). https://doi.org/10.1149/2.0311916jes
133. Jiang, Z., Liang, T.B., Liu, Y., et al.: Improved ionic conductivity and Li dendrite suppression capability toward $Li_7P_3S_{11}$-based solid electrolytes triggered by Nb and O cosubstitution. ACS Appl. Mater. Interfaces **12**, 54662–54670 (2020). https://doi.org/10.1021/acsami.0c15903
134. Mercier, R., Malugani, J.P., Fahys, B., et al.: Superionic conduction in Li_2S-P_2S_5-LiI - glasses. Solid State Ion. **5**, 663–666 (1981). https://doi.org/10.1016/0167-2738(81)90341-6
135. Rangasamy, E., Liu, Z.C., Gobet, M., et al.: An iodide-based $Li_7P_2S_8I$ superionic conductor. J. Am. Chem. Soc. **137**, 1384–1387 (2015). https://doi.org/10.1021/ja508723m
136. Han, F.D., Yue, J., Zhu, X.Y., et al.: Suppressing Li dendrite formation in Li_2S–P_2S_5 solid electrolyte by LiI incorporation. Adv. Energy Mater. **8**, 1703644 (2018). https://doi.org/10.1002/aenm.201703644
137. Zhao, F.P., Liang, J.W., Yu, C., et al.: A versatile Sn-substituted argyrodite sulfide electrolyte for all-solid-state Li metal batteries. Adv. Energy Mater. **10**, 1903422 (2020). https://doi.org/10.1002/aenm.201903422
138. Park, C., Lee, S., Kim, M., et al.: Li metal stability enhancement of Sn-doped Li_2S–P_2S_5 glass-ceramics electrolyte. Electrochim. Acta **390**, 138808 (2021). https://doi.org/10.1016/j.electacta.2021.138808
139. Yao, X.Y., Huang, N., Han, F.D., et al.: High-performance all-solid-state lithium–sulfur batteries enabled by amorphous sulfur-coated reduced graphene oxide cathodes. Adv. Energy Mater. **7**, 1602923 (2017). https://doi.org/10.1002/aenm.201602923
140. Shin, B.R., Nam, Y.J., Oh, D.Y., et al.: Comparative study of TiS_2/Li–In all-solid-state lithium batteries using glass-ceramic Li_3PS_4 and $Li_{10}GeP_2S_{12}$ solid electrolytes. Electrochim. Acta **146**, 395–402 (2014). https://doi.org/10.1016/j.electacta.2014.08.139
141. Li, J.W., Li, Y.Y., Cheng, J., et al.: A graphene oxide coated sulfide-based solid electrolyte for dendrite-free lithium metal batteries. Carbon **177**, 52–59 (2021). https://doi.org/10.1016/j.carbon.2021.01.159
142. Li, J.W., Li, Y.Y., Cheng, J., et al.: In situ modified sulfide solid electrolyte enabling stable lithium metal batteries. J. Power. Sources **518**, 230739 (2022). https://doi.org/10.1016/j.jpowsour.2021.230739
143. Li, Y., Cao, D.X., Arnold, W., et al.: Regulated lithium ionic flux through well-aligned channels for lithium dendrite inhibition in solid-state batteries. Energy Storage Mater. **31**, 344–351 (2020). https://doi.org/10.1016/j.ensm.2020.06.029
144. Jiang, W., Yan, L.J., Zeng, X.M., et al.: Adhesive sulfide solid electrolyte interface for lithium metal batteries. ACS Appl. Mater. Interfaces **12**, 54876–54883 (2020). https://doi.org/10.1021/acsami.0c17828
145. Lewis, J.A., Cavallaro, K.A., Liu, Y., et al.: The promise of alloy anodes for solid-state batteries. Joule **6**, 1418–1430 (2022). https://doi.org/10.1016/j.joule.2022.05.016
146. Hou, L.P., Yuan, H., Zhao, C.Z., et al.: Improved interfacial electronic contacts powering high sulfur utilization in all-solid-state lithium–sulfur batteries. Energy Storage Mater. **25**, 436–442 (2020). https://doi.org/10.1016/j.ensm.2019.09.037
147. Nagao, M., Hayashi, A., Tatsumisago, M.: Bulk-type lithium metal secondary battery with indium thin layer at interface between Li electrode and Li_2S–P_2S_5 solid electrolyte. Electrochemistry **80**, 734–736 (2012). https://doi.org/10.5796/electrochemistry.80.734
148. Santhosha, A.L., Medenbach, L., Buchheim, J.R., et al.: The indium–lithium electrode in solid-state lithium-ion batteries: phase formation, redox potentials, and interface stability. Batter. Supercaps **2**, 524–529 (2019). https://doi.org/10.1002/batt.201800149
149. Luo, S.T., Wang, Z.Y., Li, X.L., et al.: Growth of lithium-indium dendrites in all-solid-state lithium-based batteries with sulfide electrolytes. Nat. Commun. **12**, 6968 (2021). https://doi.org/10.1038/s41467-021-27311-7
150. Park, S.W., Choi, H.J., Yoo, Y., et al.: Stable cycling of all-solid-state batteries with sacrificial cathode and lithium-free indium layer (adv. funct. mater. 5/2022). Adv. Funct. Mater. **32**, 2108203 (2022). https://doi.org/10.1002/adfm.202270030
151. Lee, G.H., Lee, S.G., Park, S.H., et al.: Interface engineering on a Li metal anode for an electro-chemo-mechanically stable anodic interface in all-solid-state batteries. J. Mater. Chem. A **10**, 10662–10671 (2022). https://doi.org/10.1039/D1TA11066G
152. Sakuma, M., Suzuki, K., Hirayama, M., et al.: Reactions at the electrode/electrolyte interface of all-solid-state lithium batteries incorporating Li–M (M=Sn, Si) alloy electrodes and

sulfide-based solid electrolytes. Solid State Ion. **285**, 101–105 (2016). https://doi.org/10.1016/j.ssi.2015.07.010
153. Hashimoto, Y., Machida, N., Shigematsu, T.: Preparation of $Li_{4.4}Ge_xSi_{1-x}$ alloys by mechanical milling process and their properties as anode materials in all-solid-state lithium batteries. Solid State Ion. **175**, 177–180 (2004). https://doi.org/10.1016/j.ssi.2004.08.022
154. Cangaz, S., Hippauf, F., Reuter, F.S., et al.: Enabling high-energy solid-state batteries with stable anode interphase by the use of columnar silicon anodes. Adv. Energy Mater. **10**, 2001320 (2020). https://doi.org/10.1002/aenm.202001320
155. Tan, D.H.S., Chen, Y.T., Yang, H.D., et al.: Carbon-free high-loading silicon anodes enabled by sulfide solid electrolytes. Science **373**, 1494–1499 (2021). https://doi.org/10.1126/science.abg7217
156. Cao, D.X., Sun, X., Li, Y.J., et al.: Long-cycling sulfide-based all-solid-state batteries enabled by electrochemo-mechanically stable electrodes. Adv. Mater. **34**, 2200401 (2022). https://doi.org/10.1002/adma.202200401
157. Cao, D.X., Sun, X., Wang, Y., et al.: Bipolar stackings high voltage and high cell level energy density sulfide based all-solid-state batteries. Energy Storage Mater. **48**, 458–465 (2022). https://doi.org/10.1016/j.ensm.2022.03.012
158. Choi, H.J., Kang, D.W., Park, J.W., et al.: In situ formed Ag–Li intermetallic layer for stable cycling of all-solid-state lithium batteries (adv. sci. 1/2022). Adv. Sci. **9**, 2103826 (2022). https://doi.org/10.1002/advs.202270001
159. Lee, Y.G., Fujiki, S., Jung, C., et al.: High-energy long-cycling all-solid-state lithium metal batteries enabled by silver–carbon composite anodes. Nat. Energy **5**, 299–308 (2020). https://doi.org/10.1038/s41560-020-0575-z
160. Chen, Z.R., Liang, Z.T., Zhong, H.Y., et al.: Bulk/interfacial synergetic approaches enable the stable anode for high energy density all-solid-state lithium–sulfur batteries. ACS Energy Lett. **7**, 2761–2770 (2022). https://doi.org/10.1021/acsenergylett.2c01334
161. Oh, J., Choi, S.H., Chang, B., et al.: Elastic binder for high-performance sulfide-based all-solid-state batteries. ACS Energy Lett. **7**, 1374–1382 (2022). https://doi.org/10.1021/acsenergylett.2c00461
162. Pan, H., Zhang, M.H., Cheng, Z., et al.: Carbon-free and binder-free Li–Al alloy anode enabling an all-solid-state Li–S battery with high energy and stability. Sci. Adv. **8**, eabn4372 (2022). https://doi.org/10.1126/sciadv.abn4372
163. Bates, J.B., Dudney, N.J., Gruzalski, G.R., et al.: Fabrication and characterization of amorphous lithium electrolyte thin films and rechargeable thin-film batteries. J. Power. Sources **43**, 103–110 (1993). https://doi.org/10.1016/0378-7753(93)80106-Y
164. Ruan, Y.D., Lu, Y., Huang, X., et al.: Acid induced conversion towards a robust and lithiophilic interface for Li–$Li_7La_3Zr_2O_{12}$ solid-state batteries. J. Mater. Chem. A **7**, 14565–14574 (2019). https://doi.org/10.1039/C9TA01911A
165. Guo, S.J., Wu, T.T., Sun, Y.G., et al.: Interface engineering of a ceramic electrolyte by Ta_2O_5 nanofilms for ultrastable lithium metal batteries. Adv. Funct. Mater. **32**, 2201498 (2022). https://doi.org/10.1002/adfm.202201498
166. Lou, J.T., Wang, G.G., Xia, Y., et al.: Achieving efficient and stable interface between metallic lithium and garnet-type solid electrolyte through a thin indium tin oxide interlayer. J. Power. Sources **448**, 227440 (2020). https://doi.org/10.1016/j.jpowsour.2019.227440
167. He, M.H., Cui, Z.H., Chen, C., et al.: Formation of self-limited, stable and conductive interfaces between garnet electrolytes and lithium anodes for reversible lithium cycling in solid-state batteries. J. Mater. Chem. A **6**, 11463–11470 (2018). https://doi.org/10.1039/C8TA02276C
168. Zhou, D., Ren, G.X., Zhang, N., et al.: Garnet electrolytes with ultralow interfacial resistance by SnS_2 coating for dendrite-free all-solid-state batteries. ACS Appl. Energy Mater. **4**, 2873–2880 (2021). https://doi.org/10.1021/acsaem.1c00193
169. Luo, W., Gong, Y.H., Zhu, Y.Z., et al.: Transition from superlithiophobicity to superlithiophilicity of garnet solid-state electrolyte. J. Am. Chem. Soc. **138**, 12258–12262 (2016). https://doi.org/10.1021/jacs.6b06777
170. Luo, Y.L., Feng, W.W., Meng, Z.J., et al.: Interface modification in solid-state lithium batteries based on garnet-type electrolytes with high ionic conductivity. Electrochim. Acta **397**, 139285 (2021). https://doi.org/10.1016/j.electacta.2021.139285
171. Feng, W.L., Dong, X.L., Li, P.L., et al.: Interfacial modification of Li/Garnet electrolyte by a lithiophilic and breathing interlayer. J. Power. Sources **419**, 91–98 (2019). https://doi.org/10.1016/j.jpowsour.2019.02.066
172. Alexander, G.V., Sreejith, O.V., Indu, M.S., et al.: Interface-compatible and high-cyclability lithiophilic lithium–zinc alloy anodes for garnet-structured solid electrolytes. ACS Appl. Energy Mater. **3**, 9010–9017 (2020). https://doi.org/10.1021/acsaem.0c01430
173. Wan, Z.P., Shi, K., Huang, Y.F., et al.: Three-dimensional alloy interface between $Li_{6.4}La_3Zr_{1.4}Ta_{0.6}O_{1.2}$ and Li metal to achieve excellent cycling stability of all-solid-state battery. J. Power Sources **505**, 230062 (2021). https://doi.org/10.1016/j.jpowsour.2021.230062
174. Fu, K.K., Gong, Y.H., Liu, B.Y., et al.: Toward garnet electrolyte-based Li metal batteries: an ultrathin, highly effective, artificial solid-state electrolyte/metallic Li interface. Sci. Adv. **3**, e1601659 (2017). https://doi.org/10.1126/sciadv.1601659
175. Huang, Y., Chen, B., Duan, J., et al.: Graphitic carbon nitride (g-C_3N_4): an interface enabler for solid-state lithium metal batteries. Angew. Chem. Int. Ed. **59**, 3699–3704 (2020). https://doi.org/10.1002/anie.201914417
176. Lu, G.J., Dong, Z.C., Liu, W., et al.: Universal lithiophilic interfacial layers towards dendrite-free lithium anodes for solid-state lithium-metal batteries. Sci. Bull. **66**, 1746–1753 (2021). https://doi.org/10.1016/j.scib.2021.04.034
177. Huang, W.L., Bi, Z.J., Zhao, N., et al.: Chemical interface engineering of solid garnet batteries for long-life and high-rate performance. Chem. Eng. J. **424**, 130423 (2021). https://doi.org/10.1016/j.cej.2021.130423
178. Hu, B.K., Yu, W., Xu, B.Q., et al.: An in situ-formed mosaic Li_7Sn_3/LiF interface layer for high-rate and long-life garnet-based lithium metal batteries. ACS Appl. Mater. Interfaces **11**, 34939–34947 (2019). https://doi.org/10.1021/acsami.9b10534
179. Baniya, A., Gurung, A., Pokharel, J., et al.: Mitigating interfacial mismatch between lithium metal and garnet-type solid electrolyte by depositing metal nitride lithiophilic interlayer. ACS Appl. Energy Mater. **5**, 648–657 (2022). https://doi.org/10.1021/acsaem.1c03157
180. Du, M.J., Sun, Y., Liu, B., et al.: Smart construction of an intimate lithium|garnet interface for all-solid-state batteries by tuning the tension of molten lithium. Adv. Funct. Mater. **31**, 2101556 (2021). https://doi.org/10.1002/adfm.202101556
181. Zhao, B., Ma, W.C., Li, B.B., et al.: A fast and low-cost interface modification method to achieve high-performance garnet-based solid-state lithium metal batteries. Nano Energy **91**, 106643 (2022). https://doi.org/10.1016/j.nanoen.2021.106643
182. Leng, J., Liang, H.M., Wang, H.Y., et al.: A facile and low-cost wet-chemistry artificial interface engineering for garnet-based solid-state Li metal batteries. Nano Energy **101**, 107603 (2022). https://doi.org/10.1016/j.nanoen.2022.107603
183. Zhong, Y.R., Xie, Y.J., Hwang, S., et al.: A highly efficient all-solid-state lithium/electrolyte interface induced by an energetic reaction. Angew. Chem. Int. Ed. **59**, 14003–14008 (2020). https://doi.org/10.1002/anie.202004477
184. Zhang, Y., Meng, J.W., Chen, K.Y., et al.: Behind the candelabra: a facile flame vapor deposition method for interfacial engineering

of garnet electrolyte to enable ultralong cycling solid-state Li–FeF_3 conversion batteries. ACS Appl. Mater. Interfaces **12**, 33729–33739 (2020). https://doi.org/10.1021/acsami.0c08203
185. Shao, Y.J., Wang, H.C., Gong, Z.L., et al.: Drawing a soft interface: an effective interfacial modification strategy for garnet-type solid-state Li batteries. ACS Energy Lett. **3**, 1212–1218 (2018). https://doi.org/10.1021/acsenergylett.8b00453
186. Xie, H., Yang, C.P., Ren, Y.Y., et al.: Amorphous-carbon-coated 3D solid electrolyte for an electro-chemomechanically stable lithium metal anode in solid-state batteries. Nano Lett. **21**, 6163–6170 (2021). https://doi.org/10.1021/acs.nanolett.1c01748
187. Cui, C., Ye, Q., Zeng, C., et al.: One-step fabrication of garnet solid electrolyte with integrated lithiophilic surface. Energy Storage Mater. **45**, 814–820 (2022). https://doi.org/10.1016/j.ensm.2021.12.027
188. Zhang, X.Y., Xiang, Q., Tang, S., et al.: Long cycling life solid-state Li metal batteries with stress self-adapted Li/garnet interface. Nano Lett. **20**, 2871–2878 (2020). https://doi.org/10.1021/acs.nanolett.0c00693
189. Bi, Z.J., Huang, W.L., Mu, S., et al.: Dual-interface reinforced flexible solid garnet batteries enabled by in situ solidified gel polymer electrolytes. Nano Energy **90**, 106498 (2021). https://doi.org/10.1016/j.nanoen.2021.106498
190. Chi, S.S., Liu, Y.C., Zhao, N., et al.: Solid polymer electrolyte soft interface layer with 3D lithium anode for all-solid-state lithium batteries. Energy Storage Mater. **17**, 309–316 (2019). https://doi.org/10.1016/j.ensm.2018.07.004
191. Cheng, Z.Y., Xie, M.L., Mao, Y.Y., et al.: Building lithiophilic ion-conduction highways on garnet-type solid-state Li^+ conductors. Adv. Energy Mater. **10**, 1904230 (2020). https://doi.org/10.1002/aenm.201904230
192. Hao, X.G., Zhao, Q., Su, S.M., et al.: Constructing multifunctional interphase between $Li_{1.4}Al_{0.4}Ti_{1.6}(PO_4)_3$ and Li metal by magnetron sputtering for highly stable solid-state lithium metal batteries. Adv. Energy Mater. **9**, 1901604 (2019). https://doi.org/10.1002/aenm.201901604
193. Liu, Y.L., Sun, Q., Zhao, Y., et al.: Stabilizing the interface of NASICON solid electrolyte against Li metal with atomic layer deposition. ACS Appl. Mater. Interfaces **10**, 31240–31248 (2018). https://doi.org/10.1021/acsami.8b06366
194. Yang, K., Chen, L.K., Ma, J.B., et al.: Progress and perspective of $Li_{1+x}Al_xTi_{2-x}(PO_4)_3$ ceramic electrolyte in lithium batteries. Infomat. **3**, 1195–1217 (2021). https://doi.org/10.1002/inf2.12222
195. Yang, L.Y., Song, Y.L., Liu, H., et al.: Nanocomposite coatings: stable interface between lithium and electrolyte facilitated by a nanocomposite protective layer (small methods 3/2020). Small Methods **4**, 1900751 (2020). https://doi.org/10.1002/smtd.202070014
196. Sheng, O.W., Zheng, J.H., Ju, Z.J., et al.: In situ construction of a LiF-enriched interface for stable all-solid-state batteries and its origin revealed by cryo-TEM. Adv. Mater. **32**, 2000223 (2020). https://doi.org/10.1002/adma.202000223
197. Wang, Y., Wang, G.X., He, P.G., et al.: Sandwich structured NASICON-type electrolyte matched with sulfurized polyacrylonitrile cathode for high performance solid-state lithium–sulfur batteries. Chem. Eng. J. **393**, 124705 (2020). https://doi.org/10.1016/j.cej.2020.124705
198. Yang, L.Y., Wang, Z.J., Feng, Y.C., et al.: Lithium-ion batteries: flexible composite solid electrolyte facilitating highly stable "soft contacting" Li–electrolyte interface for solid state lithium-ion batteries (adv. energy. mater 22/2017). Adv. Energy Mater. **7**, 1701437 (2017). https://doi.org/10.1002/aenm.201770130
199. Lei, M., Fan, S.S., Yu, Y.F., et al.: NASICON-based solid state Li–Fe–F conversion batteries enabled by multi-interface-compatible sericin protein buffer layer. Energy Storage Mater. **47**, 551–560 (2022). https://doi.org/10.1016/j.ensm.2022.02.031
200. Hou, G.M., Ma, X.X., Sun, Q.D., et al.: Lithium dendrite suppression and enhanced interfacial compatibility enabled by an ex situ SEI on Li anode for LAGP-based all-solid-state batteries. ACS Appl. Mater. Interfaces **10**, 18610–18618 (2018). https://doi.org/10.1021/acsami.8b01003
201. Hu, F., Li, Y.Y., Wei, Y., et al.: Construct an ultrathin bismuth buffer for stable solid-state lithium metal batteries. ACS Appl. Mater. Interfaces **12**, 12793–12800 (2020). https://doi.org/10.1021/acsami.9b21717
202. Jadhav, H.S., Kalubarme, R.S., Jadhav, A.H., et al.: Highly stable bilayer of LiPON and B_2O_3 added $Li_{1.5}Al_{0.5}Ge_{1.5}(PO_4)$ solid electrolytes for non-aqueous rechargeable Li–O_2 batteries. Electrochim. Acta **199**, 126–132 (2016). https://doi.org/10.1016/j.electacta.2016.03.143
203. Zhang, S.N., Zeng, Z., Zhai, W., et al.: Bifunctional in situ polymerized interface for stable LAGP-based lithium metal batteries. Adv. Mater. Interfaces **8**, 2100072 (2021). https://doi.org/10.1002/admi.202100072
204. Wang, Q.C., Ding, X.Y., Li, J.B., et al.: Minimizing the interfacial resistance for a solid-state lithium battery running at room temperature. Chem. Eng. J. **448**, 137740 (2022). https://doi.org/10.1016/j.cej.2022.137740
205. Sharafi, A., Kazyak, E., Davis, A.L., et al.: Surface chemistry mechanism of ultra-low interfacial resistance in the solid-state electrolyte $Li_7La_3Zr_2O_{12}$. Chem. Mater. **29**, 7961–7968 (2017). https://doi.org/10.1021/acs.chemmater.7b03002
206. Huo, H.Y., Chen, Y., Zhao, N., et al.: In situ formed Li_2CO_3-free garnet/Li interface by rapid acid treatment for dendrite-free solid-state batteries. Nano Energy **61**, 119–125 (2019). https://doi.org/10.1016/j.nanoen.2019.04.058
207. Duan, H., Chen, W.P., Fan, M., et al.: Building an air stable and lithium deposition regulable garnet interface from moderate-temperature conversion chemistry. Angew. Chem. Int. Ed. Engl. **59**, 12069–12075 (2020). https://doi.org/10.1002/anie.202003177
208. Patra, S., Krupa, B.R., Chakravarty, V., et al.: Microstructural engineering in lithium garnets by hot isostatic press to cordon lithium dendrite growth and negate interfacial resistance for all solid state battery applications. Electrochim Acta **312**, 320–328 (2019). https://doi.org/10.1016/j.electacta.2019.05.003
209. Tsai, C.L., Roddatis, V., Chandran, C.V., et al.: $Li_7La_3Zr_2O_{12}$ interface modification for Li dendrite prevention. ACS Appl. Mater. Interfaces **8**, 10617–10626 (2016). https://doi.org/10.1021/acsami.6b00831
210. Suzuki, Y., Kami, K., Watanabe, K., et al.: Transparent cubic garnet-type solid electrolyte of Al_2O_3-doped $Li_7La_3Zr_2O_{12}$. Solid State Ion. **278**, 172–176 (2015). https://doi.org/10.1016/j.ssi.2015.06.009
211. Zhu, J.X., Li, X.L., Wu, C.W., et al.: A multilayer ceramic electrolyte for all-solid-state Li batteries. Angew. Chem. Int. Ed. **60**, 3781–3790 (2021). https://doi.org/10.1002/anie.202014265
212. Rangasamy, E., Wolfenstine, J., Sakamoto, J.: The role of Al and Li concentration on the formation of cubic garnet solid electrolyte of nominal composition $Li_7La_3Zr_2O_{12}$. Solid State Ion. **206**, 28–32 (2012). https://doi.org/10.1016/j.ssi.2011.10.022
213. Sharafi, A., Meyer, H.M., Nanda, J., et al.: Characterizing the Li–$Li_7La_3Zr_2O_{12}$ interface stability and kinetics as a function of temperature and current density. J. Power. Sources **302**, 135–139 (2016). https://doi.org/10.1016/j.jpowsour.2015.10.053
214. Kumar, P.J., Nishimura, K., Senna, M., et al.: A novel low-temperature solid-state route for nanostructured cubic garnet $Li_7La_3Zr_2O_{12}$ and its application to Li-ion battery. RSC Adv. **6**, 62656–62667 (2016). https://doi.org/10.1039/C6RA09695F
215. Li, Y.Q., Wang, Z., Li, C.L., et al.: Densification and ionic-conduction improvement of lithium garnet solid electrolytes by flowing oxygen sintering. J. Power. Sources **248**, 642–646 (2014). https://doi.org/10.1016/j.jpowsour.2013.09.140

216. Zheng, C.J., Lu, Y., Su, J.M., et al.: Grain boundary engineering enabled high-performance garnet-type electrolyte for lithium dendrite free lithium metal batteries. Small Methods **6**, 2200667 (2022). https://doi.org/10.1002/smtd.202200667
217. Xu, R., Liu, F., Ye, Y.S., et al.: A morphologically stable Li/electrolyte interface for all-solid-state batteries enabled by 3D-micropatterned garnet. Adv. Mater. **33**, 2104009 (2021). https://doi.org/10.1002/adma.202104009
218. Xu, S.M., McOwen, D.W., Wang, C.W., et al.: Three-dimensional, solid-state mixed electron-ion conductive framework for lithium metal anode. Nano Lett. **18**, 3926–3933 (2018). https://doi.org/10.1021/acs.nanolett.8b01295
219. Xu, S.M., McOwen, D.W., Zhang, L., et al.: All-in-one lithium-sulfur battery enabled by a porous-dense-porous garnet architecture. Energy Storage Mater. **15**, 458–464 (2018). https://doi.org/10.1016/j.ensm.2018.08.009
220. Yang, C.P., Zhang, L., Liu, B.Y., et al.: Continuous plating/stripping behavior of solid-state lithium metal anode in a 3D ion-conductive framework. Proc. Natl. Acad. Sci. U. S. A. **115**, 3770–3775 (2018). https://doi.org/10.1073/pnas.1719758115
221. Yi, E., Shen, H., Heywood, S., et al.: All-solid-state batteries using rationally designed garnet electrolyte frameworks. ACS Appl. Energy Mater. **3**, 170–175 (2020). https://doi.org/10.1021/acsaem.9b02101
222. Fu, X.J., Wang, T.T., Shen, W.Z., et al.: A high-performance carbonate-free lithium|garnet interface enabled by a trace amount of sodium. Adv. Mater. **32**, 2000575 (2020). https://doi.org/10.1002/adma.202000575
223. Dai, Q.S., Zhao, J., Ye, H.J., et al.: Ultrastable anode/electrolyte interface in solid-state lithium–metal batteries using $LiCu_x$ nanowire network host. ACS Appl. Mater. Interfaces **13**, 42822–42831 (2021). https://doi.org/10.1021/acsami.1c11613
224. Duan, J., Wu, W.Y., Nolan, A.M., et al.: Solid-state batteries: lithium–graphite paste: an interface compatible anode for solid-state batteries (adv. mater. 10/2019). Adv. Mater. **31**, 1807243 (2019). https://doi.org/10.1002/adma.201970068
225. Wen, J.Y., Huang, Y., Duan, J., et al.: Highly adhesive Li-BN nanosheet composite anode with excellent interfacial compatibility for solid-state Li metal batteries. ACS Nano **13**, 14549–14556 (2019). https://doi.org/10.1021/acsnano.9b08803
226. Cao, C.C., Zhong, Y.J., Wasalathilake, K.C., et al.: A low resistance and stable lithium-garnet electrolyte interface enabled by a multifunctional anode additive for solid-state lithium batteries. J. Mater. Chem. A **10**, 2519–2527 (2022). https://doi.org/10.1039/d1ta07804f
227. Liu, B., Du, M.J., Chen, B.B., et al.: A simple strategy that may effectively tackle the anode-electrolyte interface issues in solid-state lithium metal batteries. Chem. Eng. J. **427**, 131001 (2022). https://doi.org/10.1016/j.cej.2021.131001
228. Wang, T.R., Duan, J., Zhang, B., et al.: A self-regulated gradient interphase for dendrite-free solid-state Li batteries. Energy Environ. Sci. **15**, 1325–1333 (2022). https://doi.org/10.1039/d1ee03604a
229. He, X.Z., Ji, X., Zhang, B., et al.: Tuning interface lithiophobicity for lithium metal solid-state batteries. ACS Energy Lett. **7**, 131–139 (2022). https://doi.org/10.1021/acsenergylett.1c02122
230. Lu, Q.W., He, Y.B., Yu, Q.P., et al.: Dendrite-free, high-rate, long-life lithium metal batteries with a 3D cross-linked network polymer electrolyte. Adv. Mater. **29**, 1604460 (2017). https://doi.org/10.1002/adma.201604460
231. Sun, H., Xie, X.X., Huang, Q., et al.: Fluorinated poly-oxalate electrolytes stabilizing both anode and cathode interfaces for all-solid-state Li/NMC811 batteries. Angew. Chem. Int. Ed. Engl. **60**, 18335–18343 (2021). https://doi.org/10.1002/anie.202107667
232. Wu, N., Li, Y.T., Dolocan, A., et al.: In situ formation of Li_3P layer enables fast Li^+ conduction across Li/solid polymer electrolyte interface. Adv. Funct. Mater. **30**, 2000831 (2020). https://doi.org/10.1002/adfm.202000831
233. Ma, Y.X., Wan, J.Y., Yang, Y.F., et al.: Scalable, ultrathin, and high-temperature-resistant solid polymer electrolytes for energy-dense lithium metal batteries. Adv. Energy Mater. **12**, 2103720 (2022). https://doi.org/10.1002/aenm.202103720
234. Zhang, X., Liu, T., Zhang, S.F., et al.: Synergistic coupling between $Li_{6.75}La_3Zr_{1.75}Ta_{0.25}O_{12}$ and poly(vinylidene fluoride) induces high ionic conductivity, mechanical strength, and thermal stability of solid composite electrolytes. J. Am. Chem. Soc. **139**, 13779–13785 (2017). https://doi.org/10.1021/jacs.7b06364
235. Zhang, X., Wang, S., Xue, C.J., et al.: Self-suppression of lithium dendrite in all-solid-state lithium metal batteries with poly(vinylidene difluoride)-based solid electrolytes. Adv. Mater. **31**, 1806082 (2019). https://doi.org/10.1002/adma.201806082
236. Fan, Z.J., Ding, B., Zhang, T.F., et al.: Solid/solid interfacial architecturing of solid polymer electrolyte-based all-solid-state lithium–sulfur batteries by atomic layer deposition. Small **15**, 1903952 (2019). https://doi.org/10.1002/smll.201903952
237. Zhang, L.K., Xu, H.M., Jing, M.X., et al.: Solid electrolyte/lithium anodes stabilized by reduced graphene oxide interlayers: implications for solid-state lithium batteries. ACS Appl. Nano Mater. **4**, 9471–9478 (2021). https://doi.org/10.1021/acsanm.1c01932
238. Zhang, L.K., Jing, M.X., Yang, H., et al.: Highly efficient interface modification between poly(propylene carbonate)-based solid electrolytes and a lithium anode by facile graphite coating. ACS Sustain. Chem. Eng. **8**, 17106–17115 (2020). https://doi.org/10.1021/acssuschemeng.0c05153
239. Ye, Y., Deng, Z., Gao, L., et al.: Lithium-rich anti-perovskite Li_2OHBr-based polymer electrolytes enabling an improved interfacial stability with a three-dimensional-structured lithium metal anode in all-solid-state batteries. ACS Appl. Mater. Interfaces **13**, 28108–28117 (2021). https://doi.org/10.1021/acsami.1c04514
240. Chen, L., Li, W.X., Fan, L.Z., et al.: Solid-state lithium batteries: intercalated electrolyte with high transference number for dendrite-free solid-state lithium batteries (adv. funct. Mater. 28/2019). Adv. Funct. Mater. **29**, 1901047 (2019). https://doi.org/10.1002/adfm.201970196
241. Croce, F., Appetecchi, G.B., Persi, L., et al.: Nanocomposite polymer electrolytes for lithium batteries. Nature **394**, 456–458 (1998). https://doi.org/10.1038/28818
242. Zhou, D., Liu, R.L., He, Y.B., et al.: SiO_2 hollow nanosphere-based composite solid electrolyte for lithium metal batteries to suppress lithium dendrite growth and enhance cycle life. Adv. Energy Mater. **6**, 1502214 (2016). https://doi.org/10.1002/aenm.201502214
243. Gurevitch, I., Buonsanti, R., Teran, A.A., et al.: Nanocomposites of titanium dioxide and polystyrene-poly(ethylene oxide) block copolymer as solid-state electrolytes for lithium metal batteries. J. Electrochem. Soc. **160**, A1611–A1617 (2013). https://doi.org/10.1149/2.117309jes
244. Zhao, C.Z., Zhang, X.Q., Cheng, X.B., et al.: An anion-immobilized composite electrolyte for dendrite-free lithium metal anodes. Proc. Natl. Acad. Sci. U. S. A. **114**, 11069–11074 (2017). https://doi.org/10.1073/pnas.1708489114
245. Yu, X.W., Manthiram, A.: A long cycle life, all-solid-state lithium battery with a ceramic–polymer composite electrolyte. ACS Appl. Energy Mater. **3**, 2916–2924 (2020). https://doi.org/10.1021/acsaem.9b02547
246. Yu, X.W., Manthiram, A.: Enhanced interfacial stability of hybrid-electrolyte lithium–sulfur batteries with a layer of multifunctional polymer with intrinsic nanoporosity. Adv. Funct. Mater. **29**, 1805996 (2019). https://doi.org/10.1002/adfm.201805996
247. Wang, C.H., Yang, Y.F., Liu, X.J., et al.: Suppression of lithium dendrite formation by using LAGP–PEO (LiTFSI) composite solid electrolyte and lithium metal anode modified by PEO (LiTFSI)

in all-solid-state lithium batteries. ACS Appl. Mater. Interfaces **9**, 13694–13702 (2017). https://doi.org/10.1021/acsami.7b00336
248. Wu, F., Wen, Z.Y., Zhao, Z.K., et al.: Double-network composite solid electrolyte with stable interface for dendrite-free Li metal anode. Energy Storage Mater. **38**, 447–453 (2021). https://doi.org/10.1016/j.ensm.2021.03.020
249. Yao, P.C., Zhu, B., Zhai, H.W., et al.: PVDF/palygorskite nanowire composite electrolyte for 4 V rechargeable lithium batteries with high energy density. Nano Lett. **18**, 6113–6120 (2018). https://doi.org/10.1021/acs.nanolett.8b01421
250. Liu, M., Guan, X., Liu, H.M., et al.: Composite solid electrolytes containing single-ion lithium polymer grafted garnet for dendrite-free, long-life all-solid-state lithium metal batteries. Chem. Eng. J. **445**, 136436 (2022). https://doi.org/10.1016/j.cej.2022.136436
251. Song, C., Li, Z.G., Peng, J., et al.: Enhancing Li ion transfer efficacy in PEO-based solid polymer electrolytes to promote cycling stability of Li–metal batteries. J. Mater. Chem. A **10**, 16087–16094 (2022). https://doi.org/10.1039/D2TA03283J
252. Hu, J.K., He, P.G., Zhang, B.C., et al.: Porous film host-derived 3D composite polymer electrolyte for high-voltage solid state lithium batteries. Energy Storage Mater. **26**, 283–289 (2020). https://doi.org/10.1016/j.ensm.2020.01.006
253. Zhang, B.H., Zhang, Y.H., Zhang, N., et al.: Synthesis and interface stability of polystyrene-poly(ethylene glycol)-polystyrene triblock copolymer as solid-state electrolyte for lithium-metal batteries. J. Power. Sources **428**, 93–104 (2019). https://doi.org/10.1016/j.jpowsour.2019.04.033
254. Yue, H.Y., Li, J.X., Wang, Q.X., et al.: Sandwich-like poly(propylene carbonate)-based electrolyte for ambient-temperature solid-state lithium ion batteries. ACS Sustain. Chem. Eng. **6**, 268–274 (2018). https://doi.org/10.1021/acssuschemeng.7b02401
255. Wu, Z.J., Xie, Z.K., Yoshida, A., et al.: Nickel phosphate nanorod-enhanced polyethylene oxide-based composite polymer electrolytes for solid-state lithium batteries. J. Colloid Interface Sci. **565**, 110–118 (2020). https://doi.org/10.1016/j.jcis.2020.01.005
256. Lee, M.J., Han, J., Lee, K., et al.: Elastomeric electrolytes for high-energy solid-state lithium batteries. Nature **601**, 217–222 (2022). https://doi.org/10.1038/s41586-021-04209-4
257. Xu, S.J., Xu, R.G., Yu, T., et al.: Decoupling of ion pairing and ion conduction in ultrahigh-concentration electrolytes enables wide-temperature solid-state batteries. Energy Environ. Sci. **15**, 3379–3387 (2022). https://doi.org/10.1039/D2EE01053D
258. Hu, J.L., Chen, K.Y., Yao, Z.G., et al.: Unlocking solid-state conversion batteries reinforced by hierarchical microsphere stacked polymer electrolyte. Sci. Bull. **66**, 694–707 (2021). https://doi.org/10.1016/j.scib.2020.11.017
259. Cheng, H., Yan, C.Y., Orenstein, R., et al.: Polyacrylonitrile nanofiber-reinforced flexible single-ion conducting polymer electrolyte for high-performance, room-temperature all-solid-state Li–metal batteries. Adv. Fiber Mater. **4**, 532–546 (2022). https://doi.org/10.1007/s42765-021-00128-1
260. Wen, S.J., Luo, C., Wang, Q.R., et al.: Integrated design of ultrathin crosslinked network polymer electrolytes for flexible and stable all-solid-state lithium batteries. Energy Storage Mater. **47**, 453–461 (2022). https://doi.org/10.1016/j.ensm.2022.02.035
261. Shim, J., Lee, J.W., Bae, K.Y., et al.: Dendrite suppression by synergistic combination of solid polymer electrolyte crosslinked with natural terpenes and lithium-powder anode for lithium–metal batteries. Chemsuschem **10**, 2274–2283 (2017). https://doi.org/10.1002/cssc.201700408
262. Yang, C.P., Wu, Q.S., Xie, W.Q., et al.: Copper-coordinated cellulose ion conductors for solid-state batteries. Nature **598**, 590–596 (2021). https://doi.org/10.1038/s41586-021-03885-6
263. Xu, G.F., Luo, L., Liang, J.W., et al.: Origin of high electrochemical stability of multi-metal chloride solid electrolytes for high energy all-solid-state lithium-ion batteries. Nano Energy **92**, 106674 (2022). https://doi.org/10.1016/j.nanoen.2021.106674
264. Liang, J.W., Li, X.N., Wang, S., et al.: Site-occupation-tuned superionic Li_xScCl_{3+x} halide solid electrolytes for all-solid-state batteries. J. Am. Chem. Soc. **142**, 7012–7022 (2020). https://doi.org/10.1021/jacs.0c00134
265. Li, X.N., Liang, J.W., Luo, J., et al.: Air-stable Li_3InCl_6 electrolyte with high voltage compatibility for all-solid-state batteries. Energy Environ. Sci. **12**, 2665–2671 (2019). https://doi.org/10.1039/C9EE02311A
266. Kwak, H., Han, D., Lyoo, J., et al.: All-solid-state batteries: new cost-effective halide solid electrolytes for all-solid-state batteries: mechanochemically prepared Fe^{3+}-substituted Li_2ZrCl_6 (adv. energy mater. 12/2021). Adv. Energy Mater. **11**, 2003190 (2021). https://doi.org/10.1002/aenm.202170045
267. Shao, Q.N., Yan, C.H., Gao, M.X., et al.: New insights into the effects of Zr substitution and carbon additive on $Li_{3-x}Er_{1-x}Zr_xCl_6$ halide solid electrolytes. ACS Appl. Mater. Interfaces **14**, 8095–8105 (2022). https://doi.org/10.1021/acsami.1c25087
268. Park, K.H., Kaup, K., Assoud, A., et al.: High-voltage superionic halide solid electrolytes for all-solid-state Li-ion batteries. ACS Energy Lett. **5**, 533–539 (2020). https://doi.org/10.1021/acsenergylett.9b02599
269. Riegger, L.M., Schlem, R., Sann, J., et al.: Lithium–metal anode instability of the superionic halide solid electrolytes and the implications for solid-state batteries. Angew. Chem. Int. Ed. **60**, 6718–6723 (2021). https://doi.org/10.1002/anie.202015238
270. Li, X.N., Liang, J.W., Kim, J.T., et al.: Highly stable halide-electrolyte-based all-solid-state Li–Se batteries. Adv. Mater. **34**, 2200856 (2022). https://doi.org/10.1002/adma.202200856
271. Ji, W.X., Zheng, D., Zhang, X.X., et al.: A kinetically stable anode interface for Li_3YCl_6-based all-solid-state lithium batteries. J. Mater. Chem. A **9**, 15012–15018 (2021). https://doi.org/10.1039/D1TA03042F
272. Li, F., Cheng, X.B., Lu, L.L., et al.: Stable all-solid-state lithium metal batteries enabled by machine learning simulation designed halide electrolytes. Nano Lett. **22**, 2461–2469 (2022). https://doi.org/10.1021/acs.nanolett.2c00187
273. Rajagopal, R., Cho, J.U., Subramanian, Y., et al.: Preparation of highly conductive metal doped/substituted $Li_7P_2S_8Br_{(1-x)}I_x$ type lithium superionic conductor for all-solid-state lithium battery applications. Chem. Eng. J. **428**, 132155 (2022). https://doi.org/10.1016/j.cej.2021.132155
274. Yu, T.W., Liang, J.W., Luo, L., et al.: Superionic fluorinated halide solid electrolytes for highly stable Li–metal in all-solid-state Li batteries. Adv. Energy Mater. **11**, 2101915 (2021). https://doi.org/10.1002/aenm.202101915
275. Tachez, M., Malugani, J.P., Mercier, R., et al.: Ionic conductivity of and phase transition in lithium thiophosphate Li_3PS_4. Solid State Ion. **14**, 181–185 (1984). https://doi.org/10.1016/0167-2738(84)90097-3
276. Liu, Z.C., Fu, W.J., Payzant, E.A., et al.: Anomalous high ionic conductivity of nanoporous β-Li_3PS_4. J. Am. Chem. Soc. **135**, 975–978 (2013). https://doi.org/10.1021/ja3110895
277. Bron, P., Johansson, S., Zick, K., et al.: $Li_{10}SnP_2S_{12}$: an affordable lithium superionic conductor. J. Am. Chem. Soc. **135**, 15694–15697 (2013). https://doi.org/10.1021/ja407393y
278. Adeli, P., Bazak, J.D., Park, K.H., et al.: Boosting solid-state diffusivity and conductivity in lithium superionic argyrodites by halide substitution. Angew. Chem. Int. Ed. **58**, 8681–8686 (2019). https://doi.org/10.1002/anie.201814222
279. Xiao, W., Wang, J.Y., Fan, L.L., et al.: Recent advances in $Li_{1+x}Al_xTi_{2-x}(PO_4)_3$ solid-state electrolyte for safe lithium batteries. Energy Storage Mater. **19**, 379–400 (2019). https://doi.org/10.1016/j.ensm.2018.10.012

280. Fu, J.: Fast Li^+ ion conducting glass-ceramics in the system Li_2O–Al_2O_3–GeO_2–P_2O_5. Solid State Ion. **104**, 191–194 (1997). https://doi.org/10.1016/S0167-2738(97)00434-7
281. Ohta, S., Kobayashi, T., Asaoka, T.: High lithium ionic conductivity in the garnet-type oxide $Li_{7-X}La_3(Zr_{2-X}, Nb_X)O_{12}$ (X=0–2). J. Power. Sources **196**, 3342–3345 (2011). https://doi.org/10.1016/j.jpowsour.2010.11.089
282. Inaguma, Y., Chen, L.Q., Itoh, M., et al.: High ionic conductivity in lithium lanthanum titanate. Solid State Commun. **86**, 689–693 (1993). https://doi.org/10.1016/0038-1098(93)90841-A
283. Jiang, Y., Yan, X.M., Ma, Z.F., et al.: Development of the PEO based solid polymer electrolytes for all-solid-state lithium ion batteries. Polymers **10**, 1237 (2018). https://doi.org/10.3390/polym10111237

Linan Jia obtained his Ph.D. degree from Dalian Maritime University, Dalian, China, in 2015, and then did her postdoctoral research at Shanghai Jiao Tong University. Her current research interests focus on the development of all-solid-state lithium batteries .

Jinhui Zhu obtained his Ph.D. degree from Shanghai Jiao Tong University in 2018. He then did his postdoctoral research at Shanghai Jiao Tong University. He has been working at Shanghai Jiao Tong University as an assistant professor since 2021. His current research interests focus on the development of practical all-solid-state Li batteries .

Xi Zhang (SM'13) received the B.E. degree in information and control engineering, the B.Sc. degree in applied mathematics, and the M.E. and Ph.D. degrees in power electronics and electric power drive from Shanghai Jiao Tong University (SJTU), Shanghai, China, in 2002, 2004, and 2007, respectively. From 2007 to 2009, he was a Postdoctoral Researcher with the Department of Electrical and Computer Engineering, University of Michigan-Dearborn, Dearborn, MI, USA. He is currently a Professor with the School of Mechanical Engineering, Institute of Automotive Engineering, SJTU .

Bangjun Guo (M'19) received the B.S. degree in applied physics from Shandong University, Jinan, China, in 2013, and the Ph.D. degree in physical electronics from East China Normal University, Shanghai, China, in 2018. Since July 2018, he has been a Postdoctoral Researcher of Automotive Engineering with the School of Mechanical Engineering, Shanghai Jiao Tong University, Shanghai. His research interests include battery management system for vehicle, lithium ion battery, and power management strategies .

Yibo Du received the B.S. degree in Mechanical engineering from Shanghai Jiao Tong University. His research interests focus on application of all-solid-state Li batteries.

Xiaodong Zhuang a synthetic material chemist, is a full professor at Shanghai Jiao Tong University and the head of The Meso-Entropy Matter Lab. His scientific interest is meso-entropy matter, including special aromatics, polymers, carbons and two-dimensional materials, for energy storage and conversion .